MICROWAVE RADIOMETER STUDIES OF ATMOSPHERIC WATER OVER THE OCEANS

VOL. I:

Technical Report for NASA Grant NAG5-943

* Miller, D.K. and K.B. Katsaros, 1992: Satellite derived surface latent heat fluxes in rapidly intensifying marine cyclones. *Mon. Wea. Rev.*, (scheduled publication: June).

* Claud, C., K.B. Katsaros, G.W. Petty, A. Chedin and N.A. Scott, 1992: A cold air outbreak over the Norwegian Sea Observed with the Tiros-N Operational Vertical Sounder (TOVS) and the Special Sensor Microwave/Imager (SSM/I). *Tellus,* (in press).

* McMurdie, L.A. and K.B. Katsaros, 1991: Satellite derived integrated water vapor distribution in oceanic midlatitude storms: variation with region and season. *Mon. Wea. Rev.,* **119,** 589-605.

* Raustein, E., H. Sundqvist & K.B. Katsaros, 1991: Quantitative comparison between simulated cloudiness and clouds objectively derived from satellite data. *Tellus,* **43A,** 306-320.

Principal Investigator: Kristina B. Katsaros
Department of Atmospheric Sciences
UNIVERSITY OF WASHINGTON
Seattle, WA 98195
Tel: (206) 543-1203
Fax: (206) 543-0308

MARCH 1992

MICROWAVE RADIOMETER STUDIES OF ATMOSPHERIC WATER OVER THE OCEANS

VOL. I:

Technical Report for NASA Grant NAG5-943

* Miller, D.K. and K.B. Katsaros, 1992: Satellite derived surface latent heat fluxes in rapidly intensifying marine cyclones. *Mon. Wea. Rev.,* (scheduled publication: June).

* Claud, C., K.B. Katsaros, G.W. Petty, A. Chedin and N.A. Scott, 1992: A cold air outbreak over the Norwegian Sea Observed with the Tiros-N Operational Vertical Sounder (TOVS) and the Special Sensor Microwave/Imager (SSM/I). *Tellus,* (in press).

* McMurdie, L.A. and K.B. Katsaros, 1991: Satellite derived integrated water vapor distribution in oceanic midlatitude storms: variation with region and season. *Mon. Wea. Rev.,* **119,** 589-605.

* Raustein, E., H. Sundqvist & K.B. Katsaros, 1991: Quantitative comparison between simulated cloudiness and clouds objectively derived from satellite data. *Tellus,* **43A,** 306-320.

Principal Investigator: Kristina B. Katsaros
Department of Atmospheric Sciences
UNIVERSITY OF WASHINGTON
Seattle, WA 98195
Tel: (206) 543-1203
Fax: (206) 543-0308

MARCH 1992

Vol. 1: Technical Report for NASA Grant NAG5-943

TABLE OF CONTENTS

MICROWAVE RADIOMETER STUDIES OF ATMOSPHERIC WATER OVER THE OCEANS

A Technical Report in Two Volumes

P.I.: Kristina B. Katsaros
Department of Atmospheric Sciences
UNIVERSITY OF WASHINGTON
Seattle, WA 98195
(206) 543-1203
(206) 543-0308

INTRODUCTION

Since the Seasat satellite carried the Scanning Multichannel Microwave Radiometer (SMMR) into space in July of 1978, shortly followed by the SMMR on Nimbus 7, which operated for almost a decade, a new type of data source on atmospheric water vapor and other meteorological parameters has been available for analysis of weather systems over the ocean. Since 1987 we have had the Scanning Multichannel Microwave/Imager (SSM/I) instrument on Defense Meteorological Satellites providing similar data. In this two volume technical report we present a collection of our work performed over the last three years under NASA grant NAGW-1688 administered by Dr. James Dodge of the Mesoscale Program at NASA Headquarters, and NASA grant NAG5-943 administered by Dr. Ramesh Kakar of the Global Processes Program. Some of the chapters are journal articles, others are conference proceedings and abstracts. A major contribution from our group is the Ph.D. thesis of Grant W. Petty, 1990, produced separately as Final Technical Report on NASA grant NAG5-943. It is available upon request.

Volume I of this report contains work mainly supported by NASA grant NAGW-1688. The first is an article for publication in *Monthly Weather Review:*

Miller, D.K. and K.B. Katsaros, 1992: Satellite derived surface latent heat fluxes in rapidly intensifying marine cyclones. *Mon. Wea. Rev.*, (scheduled publication: June).

It is derived from the following Masters of Science thesis:

> Miller, Douglas K., 1990: *Estimation of Surface Latent Heat Flux Patterns Preceding a Rapidly Intensifying Cyclone Derived from the Special Sensor Microwave/Imager*. M. Sci. Thesis, Department of Atmospheric Sciences, University of Washington, Seattle, WA 98195. [Not included in this report.]

In this thesis a method for evaluating the preconditioning of the marine environment via surface moisture flux 24 hours in advance of rapid deepening of a cyclonic storm is explored with data from a 1988 pre-ERICA (Extratropical Rapidly Intensifying Cyclones over the Atlantic) storm. We plan to carry on this project with studies of the 1989-90 ERICA storms (Hadlock and Kreitzberg, 1988).

One of our goals was to make full use of the new tool for studying marine weather systems that the SSM/I represents by applying our algorithms and versatile graphics presentation to the task at hand. The hardware and software system were developed by G.W. Petty while a graduate student with funds supplied by a special NASA grant (NAS8-36473, Cyclonic Storms).

Collaboration with the following colleagues and visiting student researchers have enabled us to advance along several avenues at once: Dr. Nelly Mognard at the University of Puget Sound; Dr. Chantal Claud of Ecole Polytechnique Paliseau, student of Professor Alain Chedin; and Ms. Aurelie Sand of the University of Paris VII, student of Professor Claude Klapisz. Results of the work presented at the European Geophysical Society meeting in Copenhagen, April 23-27, 1990, were reported on in our Third Annual Report, 1990. The following new work was presented at the Royal Meteorological Society/American Meteorological Society joint meeting in London, September 3-7, 1990:

> Claud, C., N. Scott, A. Chedin, K. Katsaros and G. Petty, 1990: Mesoscale Meteorology in Polar Regions from a Coupling of NOAA (TOVS) and DMSP (SSM/I) Data. In Preprint Volume, *Fifth Conference on Satellite Meteorology and Oceanography*, September 3-7, 1990, London, U.K. Published by the Am. Meteorol. Soc., Boston, MA.

> Mognard, N.M. and K.B. Katsaros, 1990: Evolution of Atmospheric Fronts over the Ocean as Observed with the Special Sensor Microwave/Imager and the Geosat Altimeter. In Preprint Volume, *Fifth Conference of the Royal Meteorological Society and the American Meteorological Society*, London, U.K., September 3-7, 1990.

The following article which will appear in Tellus is an extension of the London presentation by Claud et al. (1990):

Claud, C., K.B. Katsaros, G.W. Petty, A. Chedin and N.A. Scott, 1992: A cold air outbreak over the Norwegian Sea observed with the Tiros-N Operational Vertical Sounder (TOVS) and the Special Sensor Microwave/Imager (SSM/I). *Tellus,* (in press).

Follow-up papers to the conference presentations by Mognard, and by Sand, are also being prepared.

Earlier work supported by the Mesoscale Program of NASA appeared this year as a journal article:

McMurdie, L.A. and K.B. Katsaros, 1991: Satellite-derived precipitable water distribution in oceanic midlatitude storms: variation with region and season. *Mon. Wea. Rev.,* **119,** 589-605.

It is also included in this report, Vol. I. Collaborative work with Scandinavian colleagues in relating the SMMR or SSM/I water parameters to similar quantities extracted from numerical models of the atmosphere have resulted in a University of Stockholm Technical Report:

Katsaros, K.B., G.W. Petty and U. Hammarstrand, 1990: Atmospheric Water Parameters in Mid-Latitude Cyclones Observed by Microwave Radiometry and Compared to Model Calculations. *Technical Report,* Meteorological Institute, University of Stockholm (in press). [Not included in this collection but available on request.]

An extension of ideas for this report were carried out with a later version of the Stockholm-Bergen mesoscale atmospheric model. A short article for *Tellus* is included in this report, Vol. I:

Raustein, E., H. Sundqvist and K.B. Katsaros, 1991: Quantitative comparison between simulated cloudiness and clouds objectively derived from satellite data. *Tellus*, **43A,** 306-320.

Volume II of this technical report contains work mainly supported by NASA grant NAG5-943 and its predecessor NASA grant NAG5-354. We recognized early on the importance of microwave radiometer estimates of precipitation over the oceans, but also the difficulty in evaluating the accuracy of such estimates since few comparison data exist. Radar data

provide a source for comparison, but the difference in resolution between the satellite estimates of the order of 35 km and the radar estimates of the order of 0.5 km are a problem. Two articles concerned with these problems have been produced and are reproduced here:

Petty, G.W. and K.B. Katsaros, 1990: Precipitation observed over the South China Sea by the Nimbus 7 Scanning Multichannel Microwave Radiometer during Winter MONEX. *J. Appl. Meteor.*, **29**, 273-287.

Petty, G.W. and K.B. Katsaros, 1992: Nimbus 7 SMMR precipitation observations calibrated against surface radar during TAMEX. *J. Appl. Met.*, (scheduled publication: May).

The research performed by Petty was also presented at the American Meteorological Society Satellite Conferences in San Diego, 1989, and London, 1990. The London conference proceedings are:

Petty, G.W. and K.B. Katsaros, 1990: New geophysical algorithms for the Special Sensor Microwave/Imager. Preprint Volume, *Fifth International Conference on Satellite Meteorology and Oceanography,* September 3-7, 1990, London, England. [Included in this report.]

Petty, G.W. and K.B. Katsaros, 1990: Nimbus 7 SMMR precipitation observations calibrated against surface radar during TAMEX. *J. Applied Met.*, (submitted). Also appearing in abbreviated form in *Preprint Volume, Fifth International Conference on Satellite Meteorology and Oceanography, September 3-7, 1990, London, England.* [Not included here; overlaps with the article above with the same title.]

The thesis work of Petty will appear as a series of articles in the near future. One has been submitted.

A review of the legacy that the Seasat Satellite provided for all of the work in our group on microwave radiometry and other work related to the scatterometer and altimeter instruments has appeared in the *Bulletin of the American Meteorological Society:*

Katsaros, K.B. and R.A. Brown, 1991: Legacy of the Seasat Mission for studies of the atmosphere and air-sea-ice interactions. *Bull. Am. Met. Soc.*, **72**, 967-981.

Three papers are accepted for presentation at the Sixth International Conference on Satellite Meteorology and Oceanography, in early 1992.

McMurdie, L. and K.Katsaros, 1992: Satellite Derived Integrated Water Vapor and Rain Intensity Patterns: Indicators of Rapid Cyclogenesis. In *Preprint Volume, 6th Conference on Satellite Meteorology and Oceanography,* Jan. 5-10, 1992, Atlanta, GA.

Mognard, N.M. and K.B. Katsaros, 1992: Comparison of Wind Speed Measurements over the Oceans with the Special Sensor Microwave/Imager and the Geosat Altimeter. In *Preprint Volume, 6th Conference on Satellite Meteorology and Oceanography,* Jan. 5-10, 1992, Atlanta, GA

Petty, G.W. and K.B. Katsaros, 1992: Morning-Evening Differences in Global and Regional Oceanic Precipitation as Observed by the SSM/I. In *Preprint Volume, 6th Conference on Satellite Meteorology and Oceanography,* Jan. 5-10, 1992, Atlanta, GA.

The preprints of these conference papers are the final contribution in Volume II.

References:

Abbey, R.F., C.W. Kreitzberg and R. Hadlock, 1987: Experiment on Rapidly Intensifying Cyclones over the Atlantic, ERICA, Overview Document, Field Research Project, Version 1. March 1987, available from the ERICA Project Office, Battelle Memorial Institute, Richland, WA.

Hadlock, R. and C.W. Kreitzberg, 1988: The Experiment on Rapidly Intensifying Cyclones over the Atlantic (ERICA) field study-objectives and plans. *Bull. Am. Met. Soc.,* **69,** 1309-1320.

Petty, G.W., 1990: On the Response of the Special Sensor Microwave/Imager to the Marine Environment - Implications for Atmospheric Parameter Retrievals. Ph.D. Thesis, October 1990, Dept. of Atmospheric Sciences, University of Washington, Seattle, WA 98195. NASA Tech Report.

SATELLITE-DERIVED SURFACE LATENT HEAT FLUXES IN A RAPIDLY INTENSIFYING MARINE CYCLONE

Douglas K. Miller*
Kristina B. Katsaros

Department of Atmospheric Sciences AK-40
UNIVERSITY OF WASHINGTON
Seattle, WA 98195
Tel: (206) 543-1203
Fax: (206) 543-0308

Monthly Weather Review
In press (publication date June 1992)

* *Present affiliation:*
Department of Earth and Atmospheric Sciences
PURDUE UNIVERSITY
West Lafayette, IN 47907

Abstract

The aim of this article is to estimate surface latent heat fluxes in the vicinity of a rapidly deepening cyclone before and during its period of most rapid intensification. We do this with a bulk parameterization scheme (Liu, Katsaros, and Businger, 1979) and remotely sensed input data.

We investigate a method for estimating the difference in specific humidity between the surface and a ten meter height using the Special Sensor Microwave/Imager (SSM/I)-observed integrated water vapor field and a sea surface temperature analysis.

The surface latent heat flux fields generally have estimated errors below 40% south of 40°N and outside the region of high integrated water vapor values associated with frontal bands. The method of estimating surface latent heat fluxes for the case study was found to be usable in most regions of the Northwest Atlantic Ocean except for those locations directly adjacent to coastlines in instances of offshore flow and in the vicinity of surface fronts.

1. Introduction

Cyclonic storms that form and move along the east coast of North America during the winter months often bring significant amounts of precipitation and strong winds to New England and the Maritime Provinces. The need to better understand and predict these storms is made clear by the direct effect that they have on mankind. In some cases they have inflicted a high cost in life and property. Ships have experienced extensive deck damage or been sunk, fishing has been disrupted, and an oil rig was once destroyed with eighty-four lives lost.

Those cyclones which fulfill a specific deepening criterion (i.e. 1 mb hr^{-1} for 24 hours, geostrophically adjusted to 60° latitude) are classified as 'rapid deepeners' (Sanders and Gyakum, 1980). These storms, also referred to as 'explosive deepeners', have been the focus of much research in the past decade. A statistical analysis of cyclone deepening rates by Roebber (1989) indicates that the Atlantic and Pacific cyclones in his sample have a significantly greater variance in cyclone deepening rates when compared to the rates for storms located over the continental U.S and Canada. Frequency distributions of the 24 hour adjusted maximum deepening rates produced by Roebber demonstrate that the marine cyclones show a greater skewness towards strong deepening than does the continental sample, indicating that an oceanic cyclone is statistically more likely to have a large deepening rate and be classified as a rapid deepener.

The importance of latent heat release in cyclogenesis is well documented. Reed and Albright (1986) examined a case of explosive cyclogenesis in the Eastern Pacific and concluded that condensational heating was the only diabatic heating process significantly contributing to the cyclonic development. In a numerical simulation of the same storm, Kuo and Reed (1988) confirmed that latent heat release and its interaction with baroclinity accounted for half of the deepening in the control

run. Reed et al. (1988) studied three storms in the North Atlantic and concluded that latent heat release was responsible for between forty and fifty percent of the deepening in two storms which were well predicted by the European Centre for Medium Range Weather Forecasts (ECMWF) T106 operational model. A conclusion of the relative importance of latent heat release for the third storm was not possible since it was not well predicted. Chen et al. (1983) and Gyakum (1983) also demonstrate the important effect of latent heat release as a contribution to cyclonic development. Kuo et al. (1991a) simulated the now famous QE-II storm and found that latent heat release significantly modified the warm frontal structure of the storm to enhance the adiabatic secondary circulation.

The vertical transport of water vapor at the surface (moisture flux or latent heat flux) can affect cyclogenesis indirectly. The upward transport of water vapor decreases low and mid-level static stability through the release of latent heat as noted by Reed and Albright (1986). Recent work by Kuo and Low-Nam (1990) and Kuo et al. (1991b) suggests that surface fluxes (both sensible and latent heat fluxes) can actually have a damping effect during the time of rapid intensification of explosively deepening storms by decreasing the low level baroclinity since cold air tends to be warmed by the surface fluxes and vice versa. Kuo et al. (1991b) tested the influence of the surface fluxes by modeling the same storm under varying surface flux conditions. Their results indicate that surface energy fluxes during the 24 hours that *preceded* the period of most rapid intensification had a much stronger effect on subsequent storm development than did the fluxes that existed as the storm rapidly intensified. The fluxes act to precondition the environment through moistening and destabilization of air at the surface thereby making water vapor available to the developing storm. As the storm spins up, the water vapor is converted to cloud water and/or rain and latent heat is released in the process.

Latent heat release, particularly in the warm frontal clouds, can enhance the storm development by inducing strong low-level convergence and vorticity spin-up as observed in the case study presented by Kuo and Reed (1988).

A preliminary field test for the Experiment on Rapidly Intensifying Cyclones over the Atlantic (ERICA, Hadlock and Kreitzberg, 1988) was conducted in late January 1988 in order to evaluate the quality of participating observing systems, data networks, field operations plans, and data management. Most of the measurement activity was concentrated in the period 25–26 January and the cyclone that developed during this period over the Northwest Atlantic is the focus of this investigation.

Explosively deepening storms are predominantly maritime events as suggested by Roebber (1989). The study of cyclones over oceans is made difficult by the poor surface observing network currently existing in oceanic regions. Useful data is sparse. Instruments mounted on satellites have helped to provide the research community with additional data over oceans. For a long time, most satellite information has come from images obtained in the visible and infrared wavelengths. However, these instruments are limited in the amount of below-cloud-top information they can yield by the thickness of clouds in the field of view. This certainly presents serious limitations for studies involving thick cloud formations such as those commonly observed in cyclones. Sensors receiving radiation in the microwave wavelengths, on the other hand, are capable of giving columnar atmospheric information in most cases when significant cloud amounts are present in the field of view. The Special Sensor Microwave/Imager (SSM/I) is one microwave instrument currently in operation which can observe oceanic regions. It will be introduced in greater detail in section 2.

The emphasis of this study will be on evaluating a method of estimating surface latent heat fluxes using data from the SSM/I, sea surface temperature (SST) and surface pressure data and to apply the method in order to examine surface latent heat flux (LHF) patterns observed in the Western Atlantic both before and during the January 1988 case. Since this storm occurred during the pre-ERICA field test, a larger set of observations exist than would be expected for most winter storms over the ocean. A secondary objective of this study is to develop methodology which can be applied to analysis of the ERICA cyclones. SSM/I data for the ERICA cyclones was not yet available when this study commenced. The 24–26 January 1988 case will be referred to hereafter as the 'pre-ERICA storm' (Hadlock and Kreitzberg, 1988 and Neiman et al., 1990).

Since the SSM/I instrument doesn't directly observe moisture flux fields, it becomes necessary to use a method by which the moisture flux field is computed given a set of mean quantities, the so called bulk parameterization method. Bulk parameterization requires that the specific humidity at a ten meter height and at the surface (Qa and Qs, respectively) be known. In this study we will develop a statistical method for inferring (Qs-Qa) given the SSM/I derived integrated water vapor (IWV) fields along with independent sea surface temperature and surface pressure fields. This method utilizes the high correlation between the IWV amount and the specific humidity at ten meters under certain conditions. The high correlation is observed because boundary layer air contains 50% or more of the integrated water vapor (Liu, 1984).

2. Data Sources

a. The SSM/I Instrument and Its Applications

In this study, we rely on satellite data derived from the SSM/I. The SSM/I is a passive microwave imager which observes electromagnetic radiation at frequencies that fall between strong absorption bands within the microwave portion of the spectrum. As a result, the radiances observed by each SSM/I channel is a combination of surface emission or reflection and the emission and attenuation occurring through the atmosphere. The SSM/I has seven channels which consist of two orthogonal polarizations at three frequencies and one polarization at a fourth frequency. A geophysical parameter can be theoretically estimated given its unique contribution to the total radiant energy received at each SSM/I channel. The atmospheric parameters that can be observed by the SSM/I consist of near surface wind speed, IWV, cloud liquid water, and an index for rain/no rain regions. However, retrieval of all of the listed parameters is not possible at all times. Difficulty occurs when the SSM/I is viewing land regions or areas where there exist significant amounts of liquid water in the field of view (Petty, 1990).

The SSM/I IWV and near surface wind speed algorithms used in this study were developed and modified by Petty and Katsaros (1990). The near surface wind speed algorithm is a modified version of the Goodberlet et al. (1989) algorithm. These algorithms were derived using statistical regression of SSM/I brightness temperatures (T_B's) against *in situ* observations of the respective parameter. The algorithms are sensitive to the presence of precipitation and result in less accurate parameter estimations as the amount of precipitation in the SSM/I field-of-view increases. They become unusable when certain T_B threshold values are exceeded. Pixels where the near surface wind speed algorithm T_B threshold values have been exceeded are referred to as 'rain flagged' pixels.

b. Other Data Sources

By mere coincidence, the SSM/I orbit results in overpasses occurring over the North and West Atlantic close to the synoptic reporting times of 0000 and 1200 UTC. The SSM/I overpasses that occurred in January 1988 to within one hour of 0000 or 1200 UTC were chosen for fitting (Qs-Qa) computed from 124 ship of opportunity and island station (S/I) surface observations to SSM/I-observed IWV and independent SST analyses. All observations that were used to compute the statistical fit are located in the North Atlantic from 20 to 50°N and from 55 to 85°W. The SSM/I overpasses used to compute surface latent heat flux fields for the period before and during the pre-ERICA storm are within the North and West Atlantic and occurred in the period ranging from 2230 UTC 23 January 1988 to 1110 UTC 26 January 1988.

The SSM/I instrument differs from its predecessor (the Scanning Multichannel Microwave Radiometer, SMMR) in that the SSM/I does not have a frequency from which sea surface temperature can be estimated accurately. Since sea surface temperature is required in order to calculate the moisture flux using the bulk parameterization method, an independent data source is needed. Two sea surface temperature analyses were used to compute the moisture flux fields for the periods before and during the pre-ERICA storm.

The first is a product of the Oceanographic Analysis Branch of the National Oceanographic and Atmospheric Administration (NOAA) and is a detailed analysis of SST's in the vicinity of the Gulf Stream Front (GSF). The second is a product consisting of contoured satellite (Advanced Very High Resolution Radiometer, AVHRR) SST observations collected over the course of a week.

The SST field used for the case study is a synthesis of both SST products. The primary SST sources were the January 24 and 25, 1988 Oceanographic Analysis

GSF analyses. The AVHRR SST map for the week of January 25, 1988 was used to fill in the ocean regions not covered by the GSF analyses in in the Northwestern Atlantic.

3. Methods of Analysis

The fact that the marine atmospheric boundary layer contains 50% or more of the integrated water vapor led Liu (1984) to attempt to estimate monthly mean Qa over the North Atlantic ocean using data from the SMMR on the Seasat satellite. Liu found that the root mean square (RMS) difference between the observed monthly Qa and his value computed using a best fit polynomial was 0.78 g kg^{-1} and the correlation was 0.99. He makes clear that using time scales shorter than a month will result in increased error in Qa using IWV as a predictor. Hsu and Blanchard (1989) tested the use of Liu's fifth-order polynomial relationship between monthly IWV and Qa (Liu, 1986) for *individual* soundings and concluded that Liu's fifth-order polynomial relationship is applicable for individual soundings and for soundings located in regions close to coastlines.

To derive a moisture flux field, the bulk parameterization method is applied in the form:

$$E = \rho \times C_E \times U_{10} \times (Qs - Qa) \tag{1}$$

where E is moisture flux $[kg\ (m^2 s)^{-1}]$, ρ is surface air density, 1.275 $[kg\ m^{-3}]$, C_E is water vapor transfer coefficient, U_{10} is wind speed at a ten meter height [m s^{-1}], Qs is saturation specific humidity at sea surface temperature $[kg\ kg^{-1}]$, and Qa is specific humidity at a ten meter height $[kg\ kg^{-1}]$.

The SSM/I wind speed algorithm is calibrated to give the wind speed at a 19.5 meter height. We use the Liu, Katsaros, and Businger (1979) [LKB] marine atmospheric surface layer model to correct the wind to a 10 meter height. A statistical fit is used to derive a (Qs-Qa) value given an SSM/I-IWV value and an independent SST value. The LKB model is used to estimate a C_E value for wind

speeds less than 10 m s^{-1}. For wind speeds that exceed 10 m s^{-1}, we use a C_E value of 1.3×10^{-3} determined by DeCosmo et al. (1990). The ρ value is assumed to be a constant, which results in a maximum density error of $\pm$ 0.06 $kg\ m^{-3}$. The latent heat flux is simply:

$$Qe = L_V \times E \tag{2}$$

where Qe is latent heat flux [$W\ m^{-2}$], L_V is $4.1868 \times (597.31 - 0.56525 \times T) \times (1.0 \times 10^3)$ [$J\ kg^{-1}$], T is air temperature [C], and E is moisture flux [$kg\ (m^2 s)^{-1}$].

The LKB model takes stratification into account in its iterations. Stratification depends on the air-sea temperature difference and the friction velocity (U_*). Since no data source exists that gives air temperature at 10 meters (T_{10}) over the spatial coverage of the SSM/I, a stand-in value for T_{10} must therefore be found. A constant temperature lapse rate was assumed where T_{10} is merely the height (10 meters) above the ocean within the surface layer multiplied by the lapse rate subtracted from the sea surface temperature. Actual surface layer lapse rates have a large variability depending upon origin of the air mass and modification of the air mass by the ocean. If the assumed temperature lapse is an overestimate, the corresponding air temperature at 10 meters will be an underestimate and the resulting relative humidity may exceed 100%.

4. Evaluation of Statistical Methods

The best polynomial fits discussed in this study represent the fits that minimize the RMS difference. The RMS difference is defined as:

$$RMSd = [(1/N)\sum_{i=1}^{N}(F_i - O_i)^2]^{\frac{1}{2}} \tag{5}$$

where $RMSd$ is root mean square difference, N is number of independent data points, F_i is estimated value, and O_i is observed value.

Traditionally, IWV has been used to estimate Qa which was then used along with a computed Qs (assuming 100% relative humidity at the ocean surface) as input for the moisture flux. A more direct method should be one which estimates the specific humidity difference (Qs-Qa) between the surface and 10 meter height since it determines the direction of the moisture flux. A reasonable step was to try a two variable regression of IWV and SST against (Qs-Qa) [hereafter referred to as the IWV,SST method]. A polynomial of the form:

$$(Qs - Qa) = a \times IWV + b \times IWV^2 + c \times SST + d \times SST^2 \tag{6}$$

was fit to the January 1988 observations. The units of SST, IWV, and (Qs-Qa) are C, $kg\ m^{-2}$, and $g\ kg^{-1}$, respectively. Coefficients a, b, c, and d are values which minimize the RMS difference. Values for a, b, c, and d are -0.11676, -0.97811×10^{-3}, 0.33441, and 0.56958×10^{-2}, respectively. Although the SST (and surface pressure) values are used directly to compute Qs in the development of the regression equation, the hope is that SST, in addition to IWV, will account for some of the variance observed in Qa and result in a more accurately estimated Qs and Qa difference.

Figure 1 is a comparison of (Qs-Qa) computed using (6) to the magnitudes of (Qs-Qa) from ship data for 124 points. The line shown has a slope equal to 1.0. The standard deviation of the observed S/I (Qs-Qa) quantity is 3.73 g kg^{-1}. The standard deviation of the estimated (Qs-Qa) quantity is 3.31 g kg^{-1}.

Of the statistical fits tested in Miller (1990), the one employing (6) to estimate (Qs-Qa) yielded the smallest RMS differences for both the 'all' and 'no rain' data sets. The difference in the RMS difference between the sample containing 'all' points and 'no rain' points was also smallest for this method. This implies that the accuracy of the IWV,SST method is less sensitive to the presence of rain than is the IWV versus Qa method (for further details see Miller, 1990). It is apparent in Table 1 that the IWV,SST method begins to give useful estimates for (Qs-Qa) when the difference exceeds 6.0 g kg^{-1}. At these magnitudes the RMS difference is no more than 23%. This range is also the one where evaporation rates are high.

The validity of the IWV,SST method could be tested independently given sufficient information of moisture in the horizontal and vertical dimensions via a moisture budget. The evaporation rate could be computed as a residual given observed values of moisture storage in a column of the atmosphere, net horizontal moisture convergence into this column and an area-averaged precipitation rate for the column. Such a test was not possible at the time of this study since there was insufficient wind and moisture data to compute reliable net horizontal moisture convergence estimates.

The 'no rain' points that fell a relatively large distance from the line of perfect agreement in Fig. 1 were inspected. These points were in the vicinity of atmospheric fronts and next to coastlines in cases of offshore flow. Such conditions represent cases where a shallow moist layer has formed underneath a dry layer of air which is a significant departure from the smooth 'climatological' specific

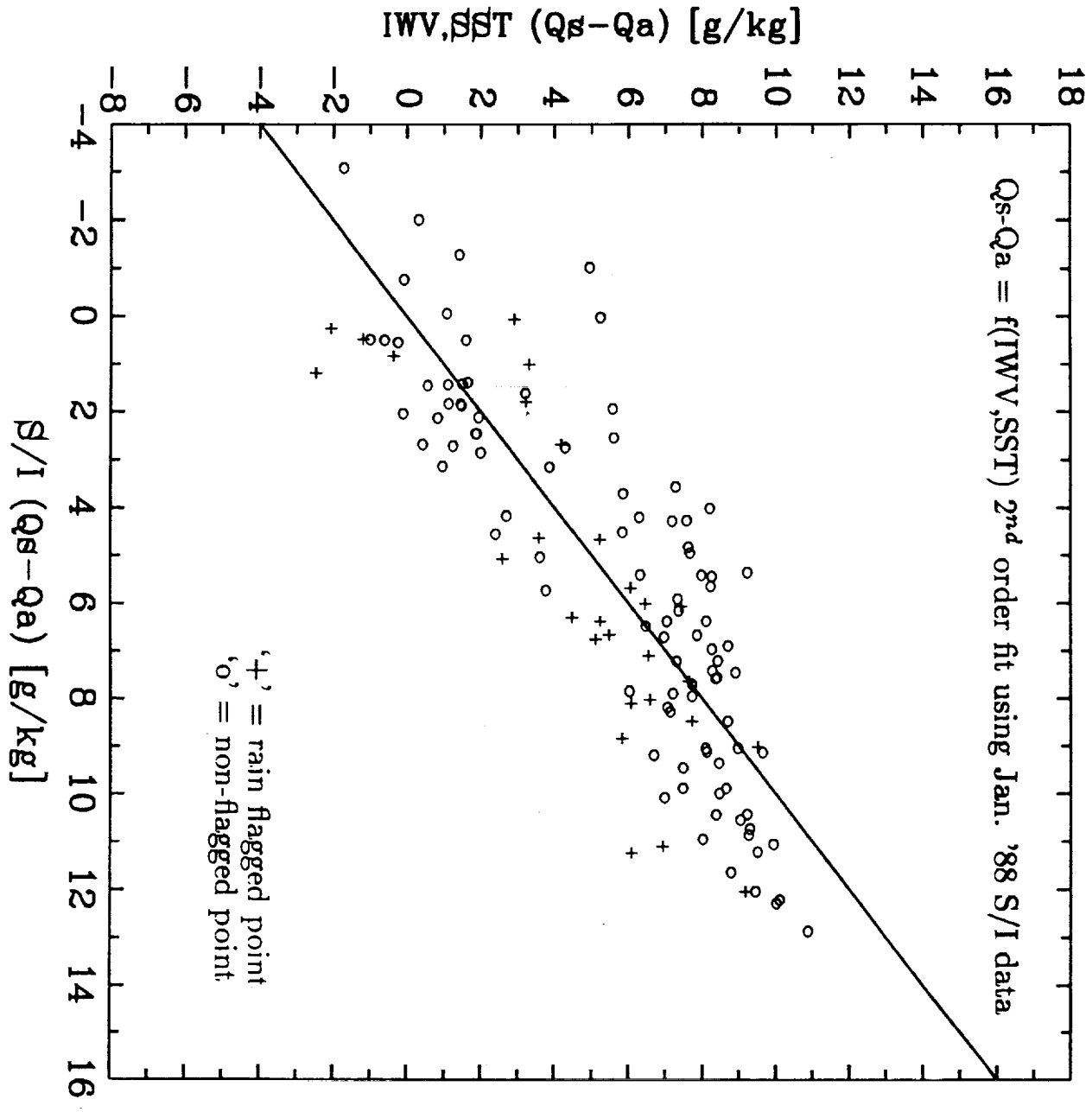

FIG. 1. Comparison of (Qs-Qa) based on SSM/I IWV and independent SST analyses to Jan. 1988 S/I observations for 124 points with a 2nd order fit for (Qs-Qa).

humidity profile assumed by applying a statistical method to infer (Qs-Qa) from IWV and SST values. Perhaps the most striking outliers are the two with the S/I (Qs-Qa) values of approximately -1.0 g kg^{-1} and 0.0 g kg^{-1}. These points lie on the warm side of a significant horizontal IWV gradient associated with a surface cold front. The IWV,SST method is best applied in regions with no large horizontal IWV gradient. In earlier studies at the University of Washington (McMurdie and Katsaros,1985; Katsaros et al.,1989a,b), we have developed a method to objectively identify frontal zones using IWV maps. IWV gradient values exceeding some critical value (e.g. 0.1 $(kg\ m^{-2})$/km; Katsaros et al.,1989b) are flagged as being located within frontal zones. This method could be used to flag regions within an SSM/I overpass where the IWV,SST method should *not* be applied. However, it was not done for this study and, as a result, surface LHF estimation in the vicinity of surface weather fronts shown on Figs. 3d, 4d and 8d should be viewed with some skepticism. A future study is needed to define the horizontal distance from surface fronts where the IWV,SST method becomes applicable.

5. The Pre-ERICA Case Study

A midlatitude cyclone formed off the coast of North Carolina on January 25, 1988 and deepened rapidly within the following 48 hours. The focus of the synoptic discussion will be on the conditions prior to and during the period of rapid deepening.

a. The Surface Weather Maps

The surface weather maps used in Figs. 2a and 2b were taken from the National Meteorological Center (NMC) Northern Hemisphere Surface Chart analyses.

At 0000 UTC on January 25 (Fig. 2a), a high pressure cell dominates the Northwest Atlantic. At the surface, light winds are observed over the ocean and cold temperatures are reported north of the cell center. The cold and stationary fronts between 25° and 35°N are attached to a cyclone which has moved east of our picture. An open wave cyclone approaches the east coast and has a central pressure of 1000 mb. By 1200 UTC on January 25 (Fig. 2b), the high pressure cell has strengthened to 1031 mb and moved further east. Buoy 44004 (38.5°N,70.6°W) reports a surface temperature of 13°C. Chatham, MA reports a surface temperature of only 4°C so a strong horizontal temperature gradient (0.026°C km^{-1}) is evident which is a reflection of the influence of the Gulf Stream. The cyclone approaching the coast has veered northward and is followed by another cyclone located near Chicago, IL. A coastal trough has developed near Cape Hatteras, NC. which spawns the eventual rapidly deepening cyclone. Curvature in the 1020 mb isobar contour at 40°N is indicative of a feature apparently observed by the map analyst on satellite imagery.

The surface analyses used in the following two time periods come from the Neiman et al. (1990) article. Much has happened by 0000 UTC on January 26

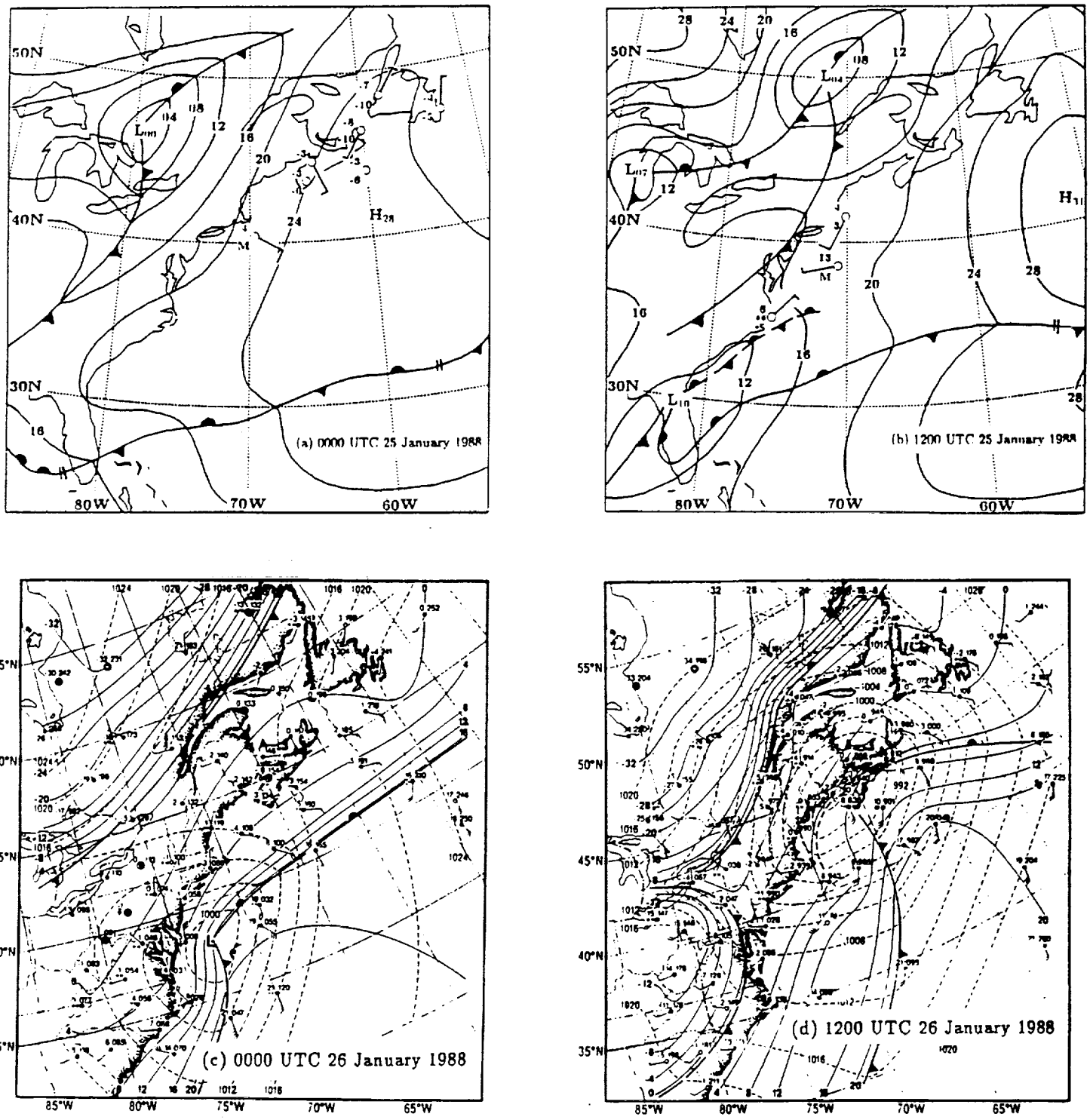

FIG. 2. Mean sea level pressure (mb) analyses at (a) 0000 UTC 25 January, (b) 1200 UTC 25 January, (c) 0000 UTC 26 January and (d) 1200 UTC 26 January 1988. Observed temperatures in (a) and (b) are shown for stations noted in the text. Observed temperatures and pressures in (c) and (d) are noted in the upper left and right portions of the station plots, respectively. Analyses in (a) and (b) are taken from NMC Northern Hemisphere Surface Charts and the analyses in (c) and (d) are from Neiman et al. (1990).

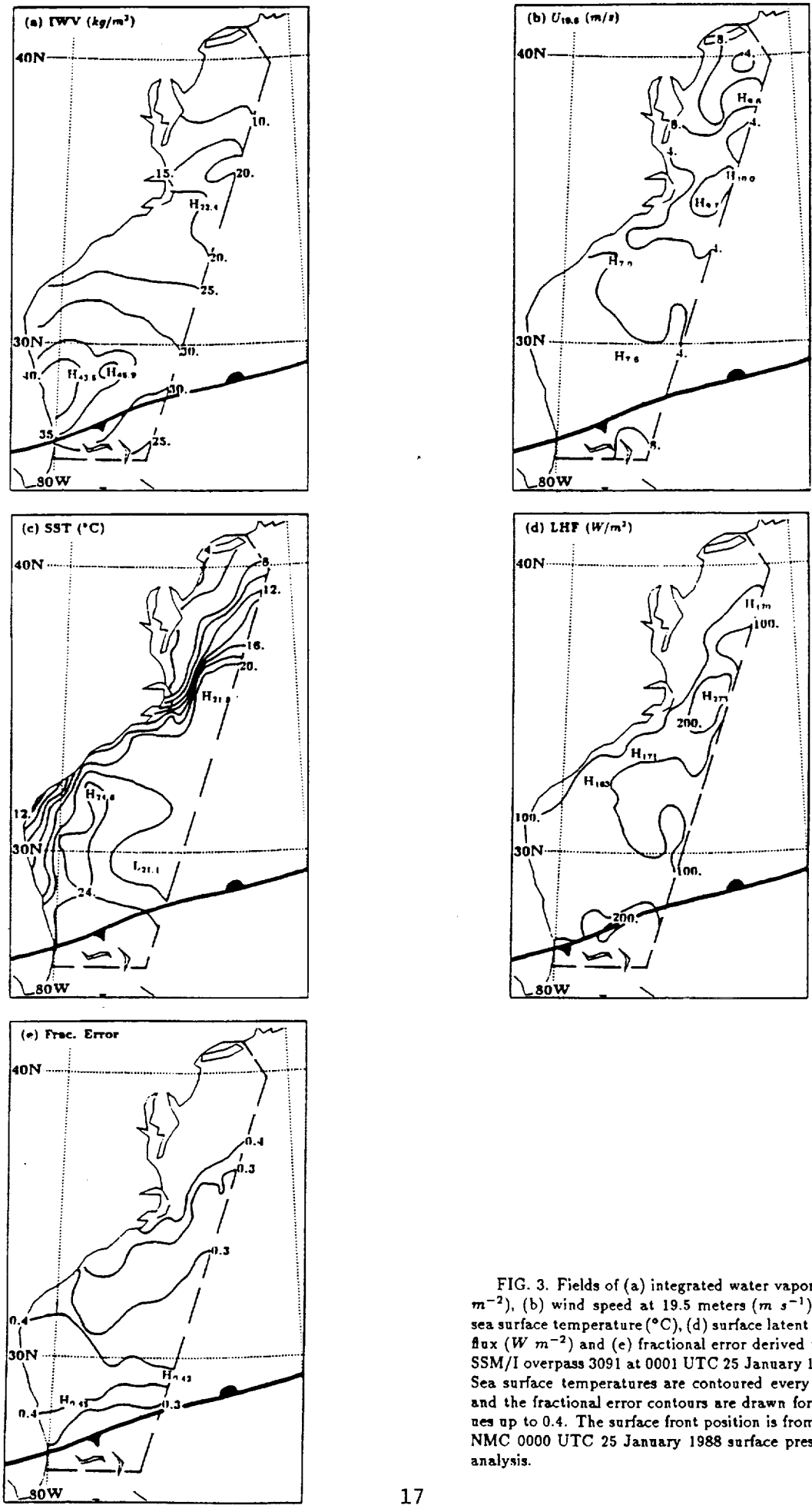

FIG. 3. Fields of (a) integrated water vapor ($kg\ m^{-2}$), (b) wind speed at 19.5 meters ($m\ s^{-1}$), (c) sea surface temperature (°C), (d) surface latent heat flux ($W\ m^{-2}$) and (e) fractional error derived from SSM/I overpass 3091 at 0001 UTC 25 January 1988. Sea surface temperatures are contoured every 2°C and the fractional error contours are drawn for values up to 0.4. The surface front position is from the NMC 0000 UTC 25 January 1988 surface pressure analysis.

(Fig. 2c). The eventual rapid deepener has formed near Cape Hatteras and moved northward as an open wave cyclone. The only other cyclone in the vicinity is the one previously located near Chicago. The high pressure cell has stalled to the east and weakened. At 1200 UTC on January 26 the storm has continued to deepen and moved northward and is on the verge of making landfall (Fig. 2d). It experiences a large deepening rate of almost 2 mb hr^{-1} from 0000 UTC to 1200 UTC on January 26 (Neiman et al. 1990).

b. The SSM/I Derived Fields

A detailed look at IWV,SST estimated surface latent heat flux fields for some SSM/I overpasses occurring both before and during the pre-ERICA case will assist in further evaluating the usefulness of our method for obtaining instantaneous flux fields over the ocean.

Several methods and assumptions were utilized for 'rain-flagged' data point locations outside of frontal zones. Those data points without a meaningful wind speed were assigned a wind speed by interpolating values from surrounding SSM/I 'no rain' points. Although this interpolation might introduce significant error in zones of large horizontal wind shear, it remains as a preferable alternative when compared to the probable error introduced by using climatological near surface wind speed estimates.

It was generally assumed that rainrates outside of frontal zones were small enough so that a meaningful SSM/I IWV value could be estimated at 'rain-flagged' locations. Also, the horizontal scale of adjacent 'rain-flagged' data pixels outside of frontal zones was generally small enough so that such regions were smoothed out in the process of interpolating SSM/I data to the 0.5 ° grid. Application of the IWV,SST method at 'rain-flagged' points might be questionable. However, it

was concluded previously that the accuracy of the IWV,SST method for estimating (Qs-Qa) is not strongly affected by the presence of rain since the difference between the RMS difference for the 'all' and for the 'no rain' samples was relatively small.

1) Sensitivity to Surface Layer Lapse Rate, Surface Pressure, SST and IWV Analyses

Surface latent heat flux fields were computed for a block of an SSM/I overpass to test their sensitivity to large variations in the surface layer lapse rate, surface pressure, SST and IWV. In testing the sensitivity of each parameter, surface LHF fields were computed with all other parameters held constant as the test parameter varied from one extreme to another. There were two trials each for the surface layer lapse rate, the surface pressure, SST and IWV sensitivity tests. These tests are summarized in Table 2. $|\Delta H|$ and $|\Delta L|$ represent the largest differences in absolute magnitude between corresponding surface LHF maxima and minima, respectively, for the various sensitivity trials of each input parameter. The surface LHF fields were found to be *not* sensitive to the assumed surface pressure analysis or the surface layer lapse rate for areas where U_{10} exceeds 7 m s^{-1} but *were* sensitive to the SST, IWV, and U_{10} fields and to the surface layer lapse rate for areas of low wind speed. The direction of the latent heat fluxes was determined by the SST and IWV values, whereas the flux magnitudes were most dependent upon U_{10}. However, the SST and IWV fields do make some contribution to the surface LHF magnitudes. Cases where low wind speeds, low(high) SST's, and high(low) IWV values are colocated are ones where the latter two fields have a significant impact on the surface LHF magnitudes, but the absolute magnitudes of the fluxes are small due to the low U_{10} values.

The apparent insensitivity of the surface LHF patterns to the surface layer lapse rate conditions for the pre-ERICA case study makes the use of an assumed constant lapse rate reasonable. A surface layer lapse rate of 6.0 °C km^{-1} will be assumed for the remainder of the moisture flux calculations. This value was chosen to follow the mean surface to 10 km lapse rate of Nuss and Anthes (1987) and is similar to the mean wintertime conditions used by Lau (1978).

2) A Look at Selected SSM/I Pre-ERICA Overpasses

By estimating the fractional error of surface LHF fields derived using the IWV,SST method, the usefulness of the fields can be discerned. Since ρ, C_E, U_{10}, and L_V are identical in surface LHF and surface LHF error calculations, fractional error is merely a ratio of the RMS difference for the appropriate '(Qs-Qa)' bin from Table 1 to the (Qs-Qa) value estimated using (6). The IWV, $U_{19.5}$, SST, surface LHF and surface LHF error calculations for three SSM/I overpasses which occurred just prior to and during the existence of the pre-ERICA storm will be analysed.

The IWV maximum east of central Florida for overpass 3091 (Fig. 3a) is to the north of the stationary front seen on the 0000 UTC 25 January surface map (Fig. 2a). The wind speed (Fig. 3b) and local IWV maxima located near Hatteras are just east of a strong SST gradient (Fig. 3c) and over water with a temperature near 22 °C. Clearly the SSM/I has observed a feature not depicted on the 0000 UTC 25 January NMC surface map. At the same positions as these maxima are moderate upward surface LHF maxima (Fig. 3d), the largest being near Cape Hatteras (273 $W\ m^{-2}$). The area covered in this overpass is located southwest of a high pressure cell. Winds are most likely transporting air from the ocean toward land so that the atmosphere within view of the SSM/I instrument is maritime in origin. The

location of the IWV maxima (Fig. 3a) relative to the GSF is similar to model results of Warner et al. (1990). In their study, the Penn State/NCAR mesoscale model is initialized with calm winds, horizontally uniform vertical structures of temperature and moisture, and a uniform surface pressure field in order to study Marine Atmospheric Boundary Layer (MABL) circulations forced by the GSF. One result is that low-level moisture convergence increases integrated water vapor just to the warm side of the north wall of the Gulf Stream. Another result is the appearance of surface latent heat fluxes from the ocean in the 200–300 $W\ m^{-2}$ range over the warmest water near the GSF. These findings are similar to what we observe on the maps of overpass 3091 (Fig. 3). The LHF maxima just off South and North Carolina are parallel to the analysed coastal trough shown on the 1200 UTC 25 January analysis. Without better spatial and temporal data it is difficult to conclude if the parallel positioning is related or a coincidence. Three of the surface LHF maxima (183, 171, and 273 $W\ m^{-2}$) are within the 0.3 fractional error contour (Fig. 3e). The isolated maximum off Maryland has an estimated error greater than 40%.

An IWV bulge has attained a wavelike shape on the IWV image of SSM/I overpass 3097 (Fig. 4a). A stationary front runs roughly east-west on the 1200 UTC 25 January surface map (Fig. 2b) at the flank of the IWV bulge. This IWV feature is colocated with the region of curvature in the 1020 mb isobar contour at 41°N on the surface analysis, so existence of the isobar curvature appears justified by SSM/I imagery. The frontal IWV maxima and IWV gradient have decreased from the time of the previous SSM/I overpass (not shown). Wind speed contours (Fig. 4b) show little organization at the time of overpass 3097. Speeds in the 8.0 to 12.0 m s^{-1} range are found in the 1020 mb isobar curvature region at 40°N while along the stationary front they are calm or low (0.0 to 8.0 m s^{-1}).

Maxima within the IWV wave (26.1 and 27.0 $kg\ m^{-2}$) suggest localized moisture convergence and marks the active region of the pressure trough. The 37 GHz polarization difference map for overpass 3097 (Fig. 5) marks it with a significant feature at 40°N, 60°W, where differences are less than 50 K (likely a rain region). This 'rain' mass is just north of a warm SST eddy (Fig. 4c) and a surface LHF maximum (Fig. 4d) at 39°N, 62°W. The proximity of the three features is not a coincidence. The 2200 UTC 25 January Sable Island (43.9°N, 60.0°W) sounding (Fig. 6) shows distinct upper and lower level moist layers. The upper layer marks an approaching warm front, the lower one cannot be the warm front according to the 0000 UTC 26 January surface analysis (Fig. 2c) since the surface warm front is not yet upon Sable Island and the low level moist layer is positioned next to the surface. An SSM/I overpass at 2203 UTC (3104) points to the lower level moist layer as being related to the 'rain' mass. The 37 GHz polarization difference map for that overpass (Fig. 7) shows the advected 'rain' mass over Sable Island. Although the pre-ERICA storm has matured by 2200 UTC 25 January, the cloud mass over Sable Island is too far north to be associated with it. The warm frontal cloud mass accompanying the pre-ERICA storm is just south of 40.0°N. Since the 'rain' mass is in the lower troposphere and it formed on the northwest side of a strong high pressure cell, it appears that it received its energy from the ocean via latent and/or sensible heating. Surface LHF maxima apparent for an SSM/I overpass preceding 3097 (number 3090) and overpass 3097 confirm that latent heating at least was a factor in the 'rain' mass development. The 252 $W\ m^{-2}$ maximum is within the 30% error region.

The pre-ERICA storm has begun its occlusion and part of the cold front is seen south and east of Florida on the 3112 IWV image (Fig. 8a). An IWV maximum of 42.7 $kg\ m^{-2}$ appears at the cold front. An IWV gradient is apparent behind

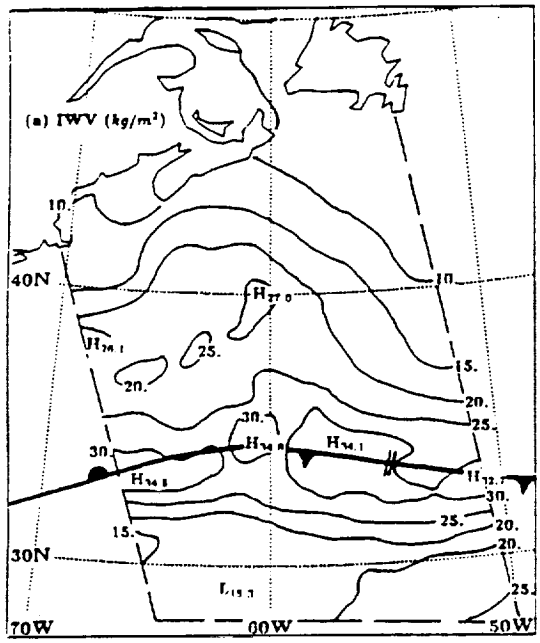

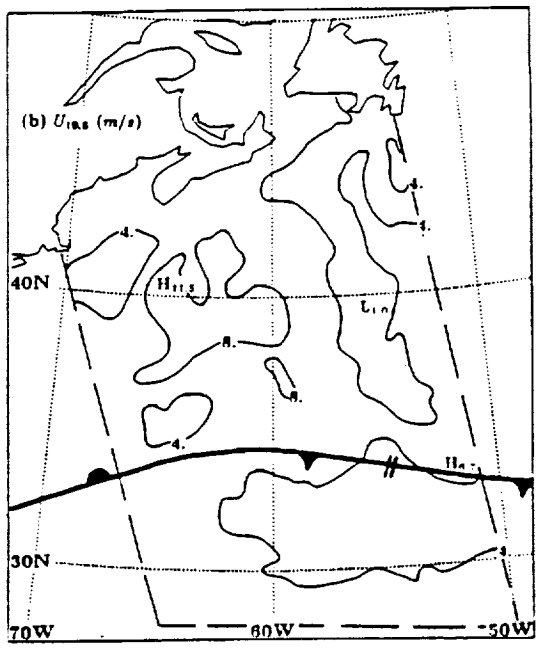

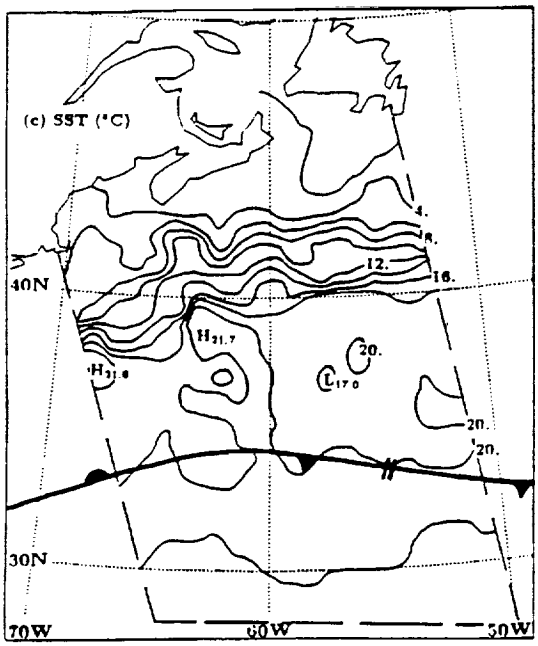

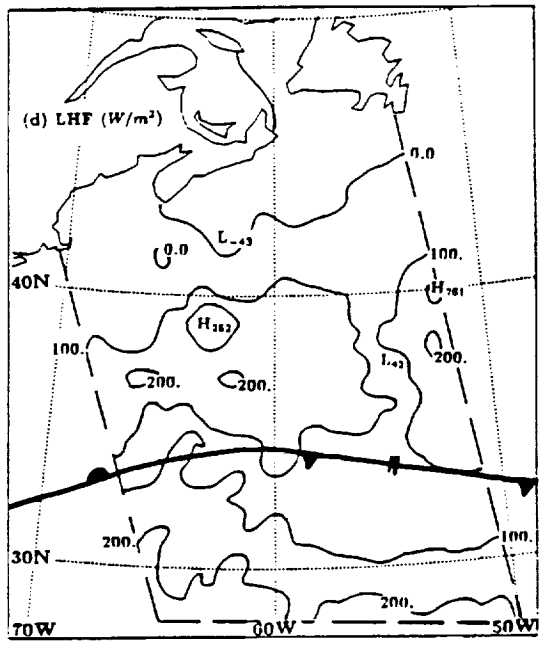

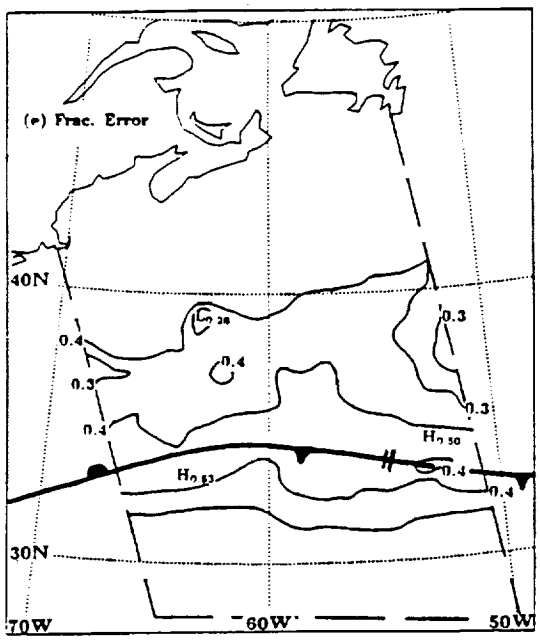

FIG. 4. Fields of (a) integrated water vapor ($kg\ m^{-2}$), (b) wind speed at 19.5 meters ($m\ s^{-1}$), (c) sea surface temperature (°C), (d) surface latent heat flux ($W\ m^{-2}$) and (e) fractional error derived from SSM/I overpass 3097 at 0942 UTC 25 January 1988. Sea surface temperatures are contoured every 2°C and the fractional error contours are drawn for values up to 0.4. The surface front position is from the NMC 1200 UTC 25 January 1988 surface pressure analysis.

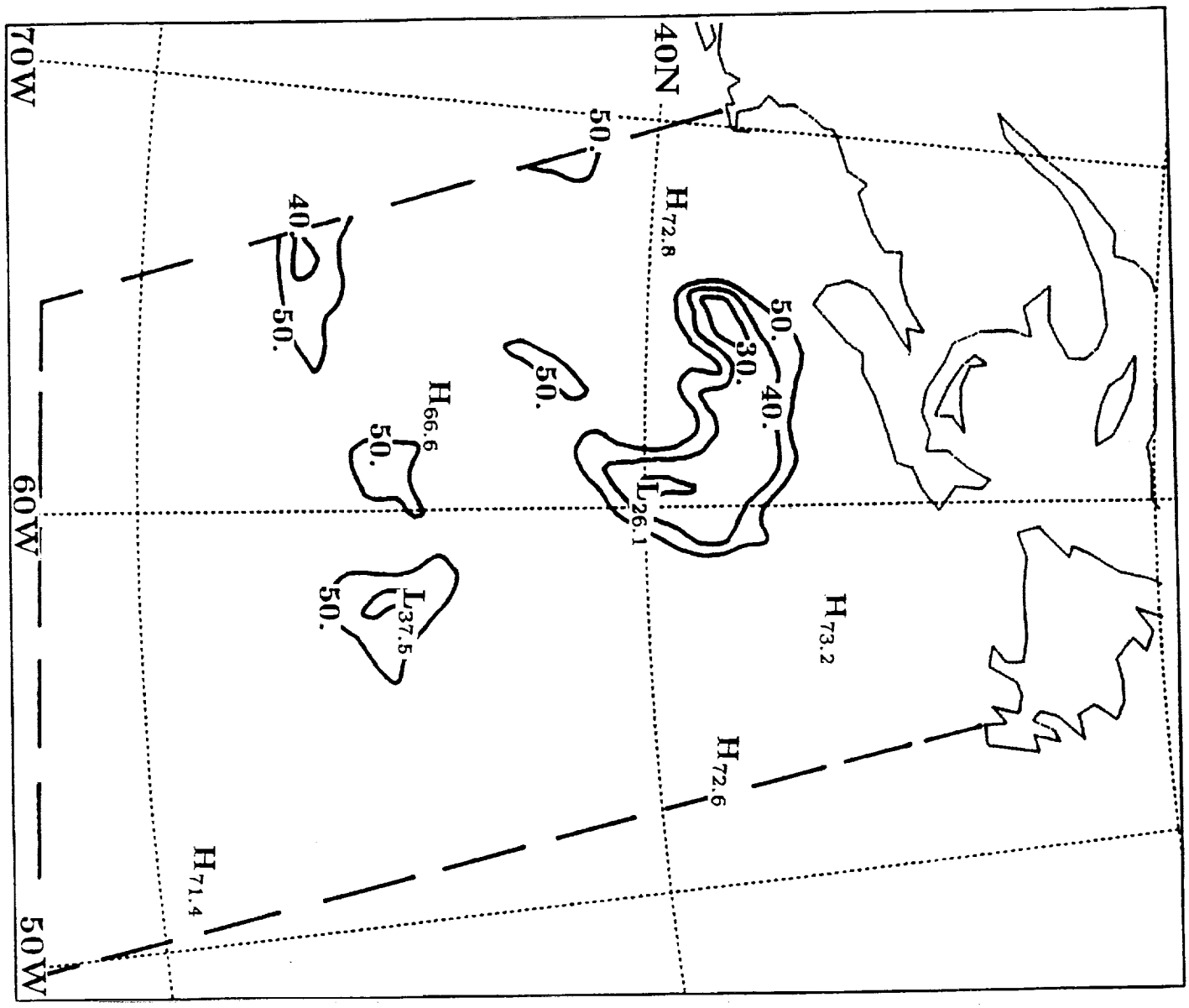

FIG. 5. 37 GHz polarization difference (K) field observed for SSM/I overpass 3097 at 0942 UTC 25 January 1988. Regions with values less than 50 K are where precipitation is most likely to be occurring.

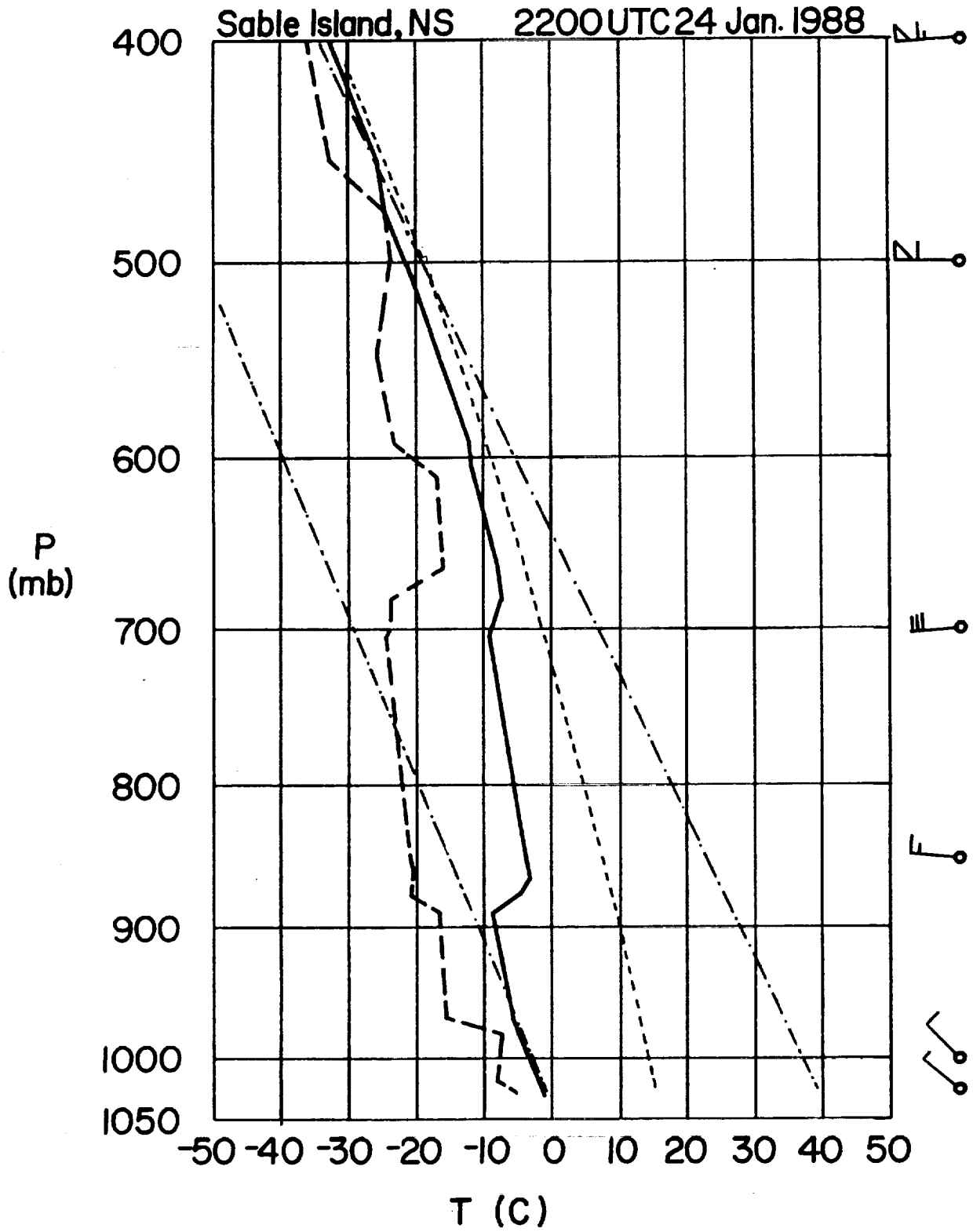

FIG. 6. Sounding at Sable Island, N.S. for 2200 UTC 25 January 1988. Temperature, solid; dewpoint, dashed; dry adiabats, dot dash; moist adiabat, pecked. Winds: full barb, 5 m s^{-1}; pennant 25 m s^{-1}.

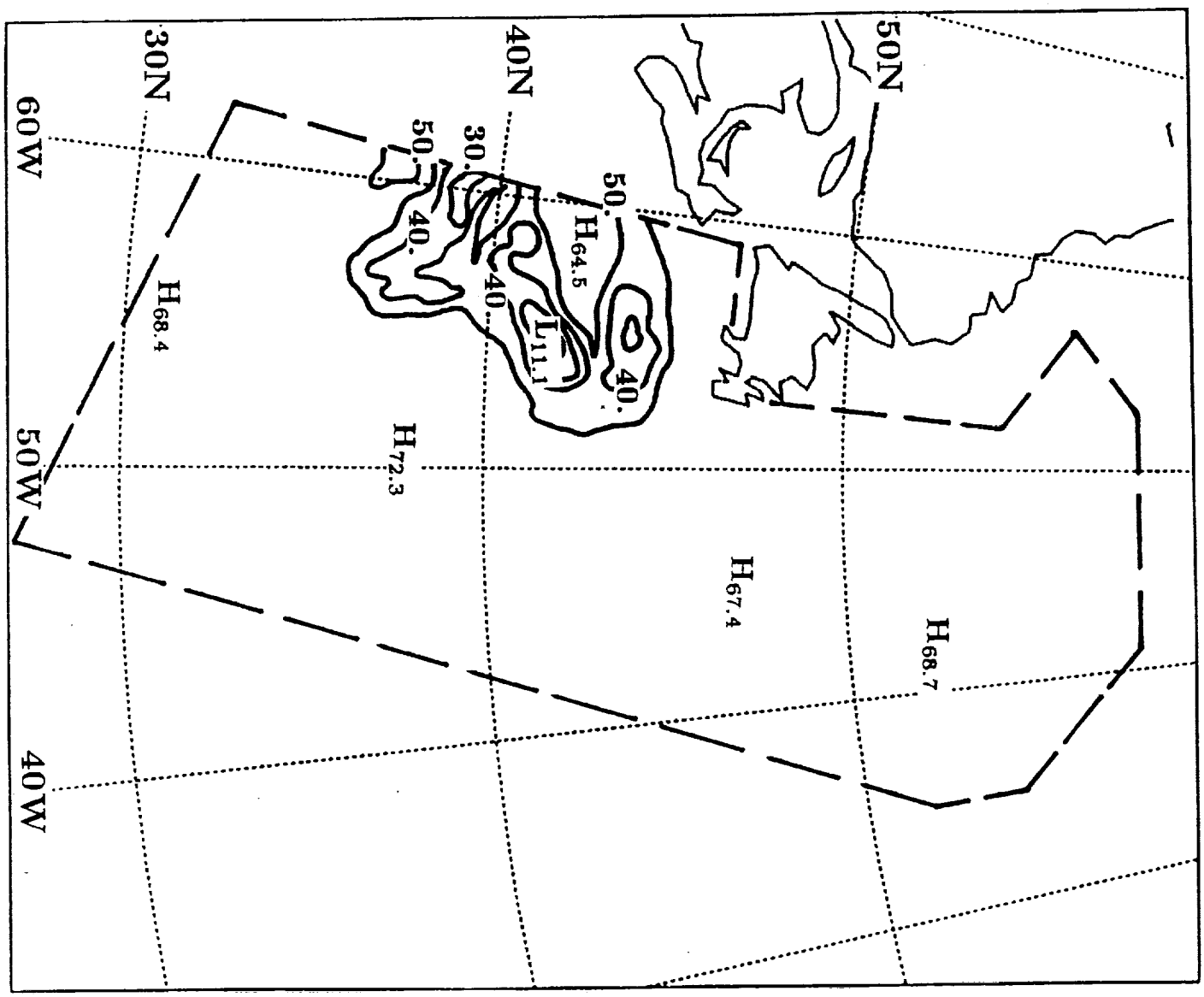

FIG. 7. 37 GHz polarization difference (K) field observed for SSM/I overpas 3104 at 2203 UTC 25 January 1988. Regions with values less than 50 K are where precipitation is most likely to be occurring.

the cold front and is associated with strong cold air advection. The 10.0 $kg\ m^{-2}$ IWV contour reaches to the southern tip of Florida and is evidence of the extent of dramatic cold air advection occurring in the southeastern states of the U.S. The low IWV values seen on Fig. 8a are consistent with the cold surface temperatures reported at 1200 UTC 26 January 1988. Wind speeds at the front range from 4.0 to 12.0 m s^{-1} (Fig. 8b). The cold air advection is occurring east of North Carolina in regions where winds exceed 12.0 m s^{-1}. These winds along with high SST's (Fig. 8c) result in large surface LHF maxima (Fig. 8d) clustered parallel to the South and North Carolina coasts. A maximum also is positioned north of the Bahamas. The IWV 10.6 $kg\ m^{-2}$ maximum well behind the cold front marks where strong upward moisture fluxes are modifying the arctic air. As this air is advected over the warm ocean, moisture is mixed upward from the ocean surface along updraft lines of alternating helical roll vortices which lie horizontally within the planetary boundary layer (Hein and Brown, 1988). Cloud streets form as a result. The existence of cloud streets was confirmed by looking at the high resolution 85 GHz SSM/I liquid water image for overpass 3112 (not shown). A look at the 37 GHz Polarization Difference map for overpass 3112 (Fig. 9) shows the extent of the developing cloud streets that were seen on the 85 GHz SSM/I image. The 60.0 K contour outlines the leading edge of the cloud street region. The location of the large upward surface LHF region near the coastline at least is confirmed by the fact that cloud streets are present to the east and the surface wind is directed so that air moves from the high evaporation rate region to the cloud street region. Fractional error (Fig. 8e) for almost the entire overpass is less than 0.4 with a significant portion less than 0.2. The observed surface LHF maxima all lie within a region of less than 30% error. The computed surface LHF fields valid at 1200 UTC 26 January 1988 from Neiman et al. (1990) are shown in Fig.

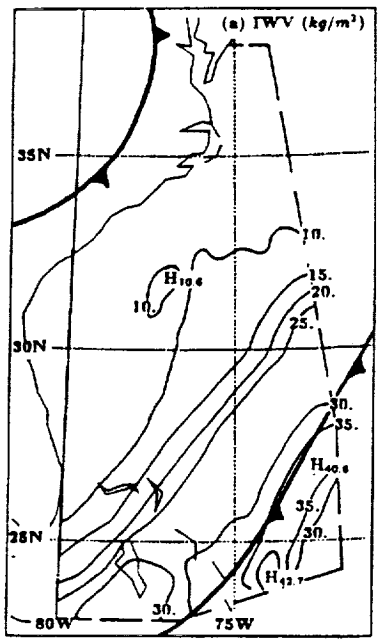

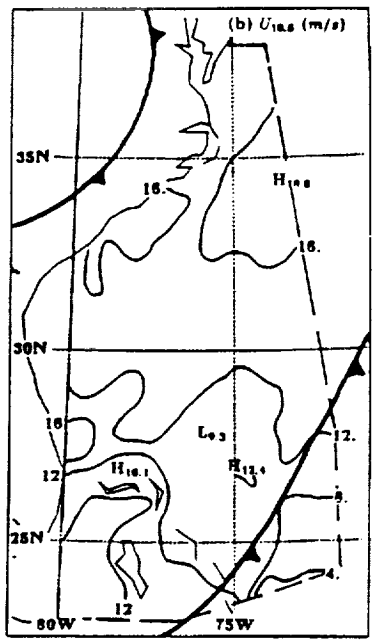

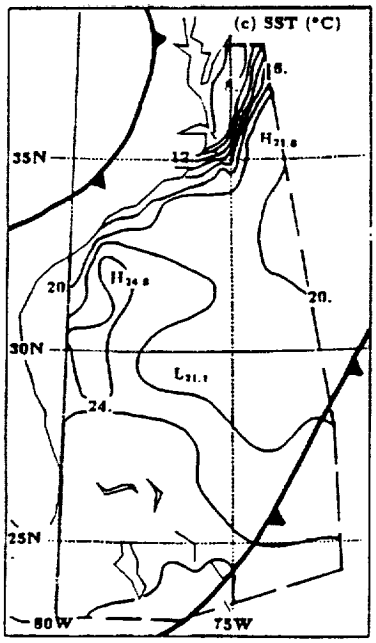

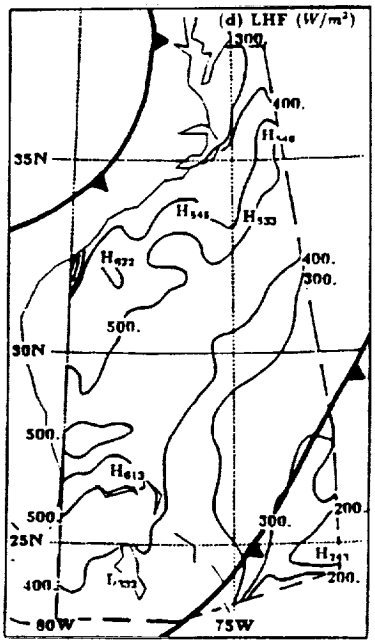

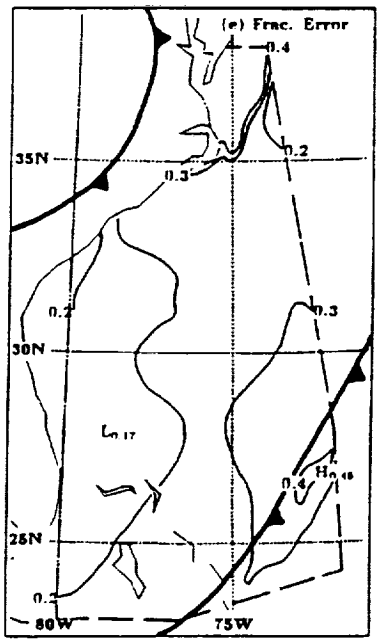

FIG. 8. Fields of (a) integrated water vapor ($kg\ m^{-2}$), (b) wind speed at 19.5 meters ($m\ s^{-1}$), (c) sea surface temperature (°C), (d) surface latent heat flux ($W\ m^{-2}$) and (e) fractional error derived from SSM/I overpass 3112 at 1110 UTC 26 January 1988. Sea surface temperatures are contoured every 2°C and the fractional error contours are drawn for values up to 0.4. The surface front position is from the Neiman et al. (1990) 1200 UTC 25 January 1988 surface pressure analysis.

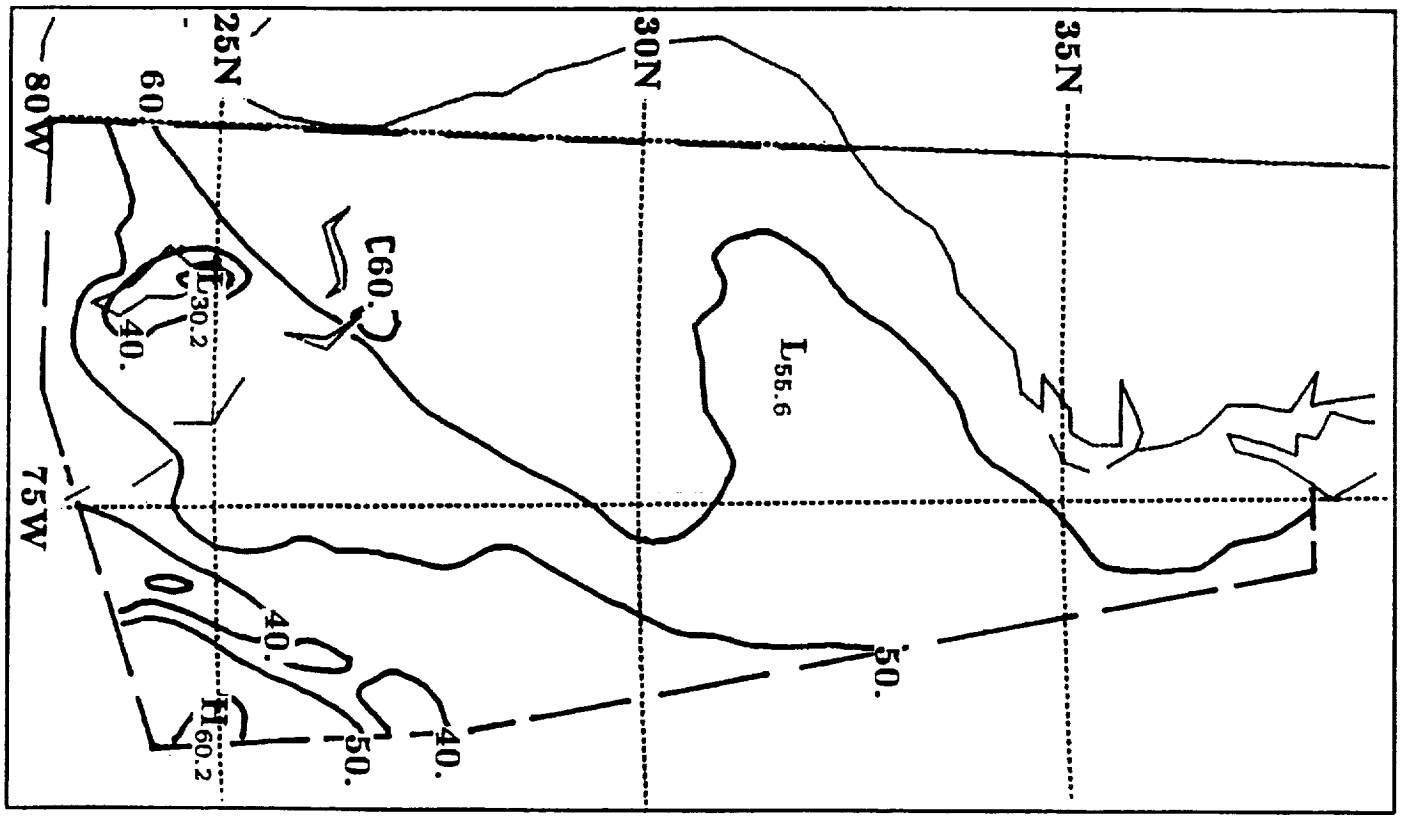

FIG. 9. 37 GHz polarization difference (K) field observed for SSM/I overpass 3112 at 1110 UTC 26 January 1988. The 60 K contour indicates the edge of developing convective cloud streets. Regions with values less than 50 K are where precipitation is most likely to be occurring.

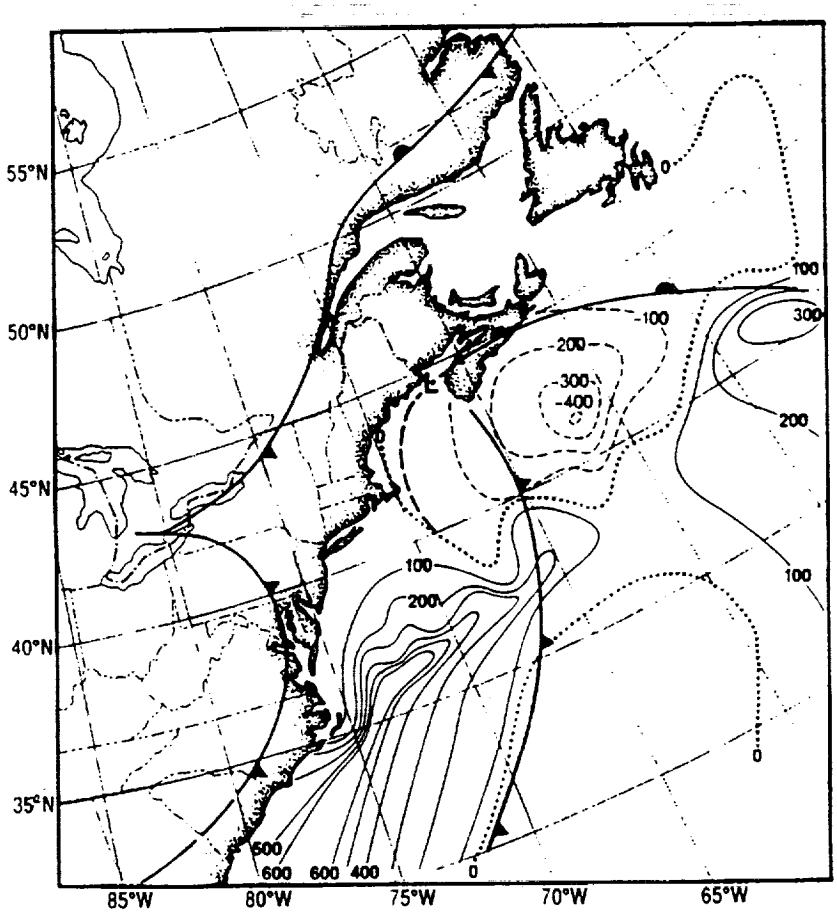

FIG. 10. Surface latent heat flux ($W\ m^{-2}$) at 1200 UTC 26 January 1988 from Neiman et al. (1990). Surface fronts at 1200 UTC 26 Jan8uary 1988 are also shown.

10. Recall that overpass 3112 ocurred at 1110 UTC on the same day. Although the spatial overlap between the two analyses is poor, the surface LHF magnitudes are comparable for coincident areas in Figs. 10 and 8d as is the tendency for the maxima to be oriented in a southwest/northeast direction.

6. Summary and Conclusions

A method was tested which utilized IWV and wind speed from the SSM/I along with SST data to estimate surface latent heat flux fields for several SSM/I overpasses which occurred during the early and middle development stages of a mid-latitude storm. A relationship was tested for estimating (Qs-Qa) as a function of SSM/I IWV and an independent SST analysis which indicated some promise since it yielded a relatively low RMS difference of 1.96 g kg^{-1} and was less sensitive to the presence of rain than was the other tested method (Qa as a function of IWV).

Sensitivity of the surface LHF fields to surface layer lapse rate, surface pressure, SST and IWV amounts was tested with the conclusion that it was low for surface pressure and for the surface layer lapse rate when wind speeds exceeded 7 m s^{-1}. The surface LHF, IWV, SST, $U_{19.5}$, and fractional error maps were presented for three SSM/I overpasses during the period leading up to rapid deepening of the pre-ERICA storm. In eight pre-ERICA SSM/I overpasses that were studied (Miller, 1990), results showed that surface LHF fields generally had estimated errors exceeding 40% north of 40°N. In these regions, cold air generally is situated over cold water so that the saturation vapor pressures at different levels within the lowest 10 meters of the atmosphere are nearly equivalent. As a result, evaporation is small and the estimated error of the statistical method is large. Most surface LHF maxima were colocated with regions of at most 30% error and some regions with less than 20% error. These results were computed so that surface wind speed error was cancelled out in the calculations. Since it is not well understood to what accuracy the surface LHF fields are needed to successfully model rapid cyclogenesis, the impact of surface LHF fields estimated from SSM/I and SST data on the prediction of rapid cyclogenesis awaits further study.

If such fields were to prove useful, employing remotely sensed data for estimating surface LHF may have most important applications in regions far from coastlines and shipping routes. The southern hemisphere oceanic areas are particularly data sparse so that methods based on remotely sensed data could broaden the understanding of storm development which occurs in those regions. Application of the presented statistical method in regions outside the domain of the case study (January in the North Atlantic Ocean) would require an expanded study to make the method more general.

In conclusion, the statistical method developed in this study could provide an important contribution to the understanding of rapidly intensifying cyclones since the surface latent heat fluxes have been shown (Kuo and Low-Nam,1990; Kuo et al.,1991b) to pre-condition the environment in a way that is favorable for cyclogenesis.

Acknowledgements

The authors would like to thank Lynn McMurdie and Grant Petty for their helpful insights. Also, comments made by the anonymous reviewers were instrumental in improving the manuscript quality. SSM/I Antenna Temperature Tapes were generously made available by Frank Wentz of Remote Sensing Systems, Inc. This research was supported by the National Aeronautics and Space Administration through Grant NAGW-1688.

BIBLIOGRAPHY

Chen, T.-C., C.-B. Chang and D.J. Perkey, 1983: Numerical study of an AMTEX '75 oceanic cyclone. *Mon. Weather Rev.*, **111**, 1818–1829.

DeCosmo, J., and K.B. Katsaros, 1989: Surface layer fluxes of momentum, heat, and water vapor during HEXMAX. Abstracts of the Fifth Scientific Assembly of the International Association of Meteorology and Atmospheric Physics, 31 July–12 August, Reading, UK, **1**, GX.31.

Goodberlet, M.A., C.T. Swift and J.C. Wilkerson, 1989: Remote sensing of ocean surface winds with the Special Sensor Microwave/Imager. *J. Geophys. Res.*, **94**, 14547–14555.

Gyakum, J.R., 1983: On the evolution of the *QEII* storm. Part II: Dynamic and thermodynamic structure. *Mon. Weather Rev.*, **111**, 1156–1173.

Hadlock, R., and C.W. Kreitzberg, 1988: The Experiment on Rapidly Intensifying Cyclones over the Atlantic (ERICA) field study–objectives and plans. *Bull. Amer. Meteor. Soc.*, **69**, 1309–1320.

Hein, P.F., and R.A. Brown, 1988: Observations of longitudinal roll vortices during arctic cold air outbreaks over open water. *Bound. Layer Meteorol.*, **45**, 177–199.

Hsu, S.A., and B.W. Blanchard, 1989: The relationship between total precipitable water and surface–level humidity over the sea surface: a further evaluation. *J. Geophys. Res.*, **94**, 14539–14545.

Katsaros, K.B., I. Bhatti, L.A. McMurdie and G.W. Petty, 1989a: Identification of atmospheric fronts over the ocean with microwave measurements of water vapor and rain. *Weather and Forecasting*, 4, 449–460.

——, G.W. Petty, I. Bhatti and D. Miller, 1989b: *Application of Special Sensor Microwave/Imager Data for Analysis of Cyclonic Storms in Midlatitudes over the Sea.* Naval Environmental Prediction Research Facility, Monterey, CA., 37 pp.

Kuo, Y.-H., M.A. Shapiro and E.G. Donall, 1991a: The interaction between baroclinic and diabatic processes in a numerical simulation of a rapidly intensifying extratropical marine cyclone. *Mon. Weather Rev.*, **119**, 368–384.

——, and R.J. Reed, 1988: Numerical simulation of an explosively deepening cyclone in the Eastern Pacific. *Mon. Weather Rev.*, **116**, 2081–2105.

——, R.J. Reed and S. Low-Nam, 1991b: Effects of surface energy fluxes during the early development and rapid intensification stages of seven explosive cyclones in the Western Atlantic. *Mon. Weather Rev.*, **119**, 457–476.

——, and S. Low-Nam, 1990: Prediction of nine explosive cyclones over the Western Atlantic Ocean with a regional model. *Mon. Weather Rev.*, **118**, 3–25.

Lau, N.C., 1978: On the three-dimensional structure of the observed transient eddy statistics of the Northern Hemisphere wintertime circulation. *J. Atmos. Sci.*, **35**, 1900–1923.

Liu, W.T., 1984: Estimation of latent heat flux with SEASAT-SMMR, a case study in N. Atlantic. *Large-Scale Oceanographic Experiments and Satellites*, C. Gautier and M. Fieux, Eds.,D. Reidel, 205–221.

——, 1986: Statistical relation between monthly mean precipitable water and surface-level humidity over global oceans. *Mon. Weather Rev.*, **114**, 1591–1602.

——, K.B. Katsaros and J.A. Businger, 1979: Bulk parameterization of air-sea exchanges of heat and water vapor including the molecular constraints at the interface. *J. Atmos. Sci.*, **36**, 1722–1735.

McMurdie, L.A., and K.B. Katsaros, 1985: Atmospheric water distribution in a mid-latitude cyclone observed by the Seasat Scanning Multichannel Microwave Radiometer. *Mon. Weather Rev.*, **113**, 584–598.

Miller, D.K., 1990: Estimation of surface latent heat flux patterns preceding a rapidly intensifying cyclone derived from the Special Sensor Microwave/Imager. M.S. Thesis, University of Washington, Seattle, 223pp.

Neiman, P.J., M.A. Shapiro, E.G. Donall and C.W. Kreitzberg, 1990: Diabatic modification of an extratropical marine cyclone warm sector by cold underlying water. *Mon. Weather Rev.*, **118**, 1576–1590.

Nuss, W.A., and R.A. Anthes, 1987: A numerical investigation of low-level processes in rapid cyclogenesis. *Mon. Weather Rev.*, **115**, 2728–2743.

Petty, G.W., 1990: On the response of the Special Sensor Microwave/Imager to the marine environment - implications for atmospheric parameter retrievals. Ph.D. Thesis, University of Washington, Seattle, 291pp.

——, and K.B. Katsaros, 1990: New geophysical algorithms for the Special Sensor Microwave Imager. Preprints of the Fifth Conference on Satellite Meteorology and Oceanography, 3–7 September, London, England, *American Meteorological Society*, 247–251.

Reed, R.J., and M.D. Albright, 1986: A case study of explosive cyclogenesis in the Eastern Pacific. *Mon. Weather Rev.*, **114**, 2297–2319.

——, A.J. Simmons, M.D. Albright and P. Undén, 1988: The role of latent heat release in explosive cyclogenesis: Three examples based on ECMWF operational forecasts. *Weather and Forecasting*, **3**, 217–229.

Roebber, P.J., 1989: On the statistical analysis of cyclone deepening rates. *Mon. Weather Rev.*, **117**, Notes and Correspondence, 2293–2298.

Sanders, F., and J.R. Gyakum, 1980: Synoptic-dynamic climatology of the "bomb". *Mon. Weather Rev.*, **108**, 1589–1606.

Warner, T.T., M.N. Lakhtakia and J.D. Doyle, 1990: Marine atmospheric boundary layer circulations forced by Gulf Stream sea surface temperature gradients. *Mon. Weather Rev.*, **118**, 309–323.

Table 1: Statistics of $(Qs - Qa)_{est}$ using the second order $(Qs - Qa)_{est} = f\{IWV, SST\}$ polynomial and $(Qs - Qa)_{obs}$ for January 1988. [NOTE: $dQa_{obs} = (Qs - Qa)_{obs}$]

Bin number:	1	2	3	Overall RMS Difference (g/kg)
Bin interval (g/kg):	-4.0< dQa_{obs} ≤2.0	2.0< dQa_{obs} ≤8.0	8.0< dQa_{obs} ≤14.0	
All data points:	No. of points = 27	No. of points = 62	No. of points = 35	2.01
RMS difference (g/kg):	2.28	1.80	2.12	
No rain flagged data points:	No. of points = 20	No. of points = 49	No. of points = 27	1.96
RMS difference (g/kg):	2.26	1.92	1.80	

Table 2: Sensitivity trials of four different surface LHF input parameters for a mean wind speed greater than 7 m/s. Sensitivity is defined in terms of the largest change in maximum ($|\Delta H|$) and minimum ($|\Delta L|$) LHF within the field.

Parameter	Trial Values of Parameter	Sensitivity
Surface Layer Lapse Rate ($C\ km^{-1}$)	-6.0 9.8	$\|\Delta H\| = 2\ W/m^2$ $\|\Delta L\| = 1\ W/m^2$
Surface Pressure (mb)	940 1050	$\|\Delta H\| = 1\ W/m^2$ $\|\Delta L\| = 0\ W/m^2$
SST (C)	0.0 27.0	$\|\Delta H\| = 900\ W/m^2$ $\|\Delta L\| = 500\ W/m^2$
IWV ($kg\ m^{-2}$)	0.0 50.0	$\|\Delta H\| = 550\ W/m^2$ $\|\Delta L\| = 450\ W/m^2$

A COLD AIR OUTBREAK OVER THE NORWEGIAN SEA OBSERVED WITH THE TIROS-N OPERATIONAL VERTICAL SOUNDER (TOVS) AND THE SPECIAL SENSOR MICROWAVE/IMAGER (SSM/I).

by

CHANTAL CLAUD, KRISTINA B. KATSAROS *, GRANT W. PETTY *,
ALAIN CHEDIN, NOELLE A. SCOTT

Laboratoire de Meteorologie Dynamique, Ecole Polytechnique, 91128 Palaiseau Cedex, France

* *Department of Atmospheric Sciences, University of Washington, Seattle, USA*

TELLUS

ABSTRACT

Until recently, the scarcity of meteorological observations over polar areas has limited studies of high-latitude weather systems, but now data from polar orbiting satellites offer a new opportunity to observe and describe these systems. TOVS data have been used successfully for delineating synoptic and sub-synoptic systems since they provide the vertical temperature structure of the atmosphere; SSM/I observations have proved valuable for analysing storms through water vapor and rain determinations. These positive results prompted us to analyze simultaneous TOVS and SSM/I observations obtained during a cold air outbreak over the Norwegian Sea. After a description of the instruments and the retrieval schemes, the mutually supporting information from these two independent instruments is discussed. Implications for the monitoring of polar lows are presented.

1. Introduction

Until recently, the scarcity of meteorological observations in polar regions has seriously hindered the study of weather systems in these areas. The advent of polar orbiting satellites with the capability of retrieving quantitative meteorological information now offers a new opportunity. Because of the large overlap at high-latitudes of consecutive swaths of data from polar orbiting satellites, one can obtain frequent samples of mesoscale weather systems and follow their development and decay.

From the TIROS-N Operational Vertical Sounder (TOVS) aboard NOAA satellites, it is possible to extract the vertical structure of the atmosphere in terms of temperature, moisture and cloudiness. Atmospheric temperature profiles can be obtained with good accuracy in most weather conditions (Le Marshall, 1988). Unfortunately, the determination of other parameters such as water vapor profiles or total water vapor content is impossible if the cloudiness is greater than a certain threshold; therefore, in polar regions where cloudiness is prevalent, such determinations often fail.

One way of alleviating this problem over the sea is to use the observations of the Special Sensor Microwave /Imager (SSM/I) launched in June 1987 on a satellite in the United States Defense Meteorological Satellite Program (DMSP) (Hollinger et al., 1987). Several studies have already shown that integrated atmospheric water vapor (precipitable water), as well as surface wind speeds can be retrieved over the open ocean from this instrument with good accuracy (Alishouse et al., 1990 ; Petty, 1990 ; Goodberlet et al., 1989).

In this paper, we present the application of both TOVS and SSM/I observations to the analysis of a cold air outbreak over the Norwegian Sea between 29 February and 1 March 1988. After some background on both instruments and the retrieval algorithms in section 2, section 3 follows with an overview of the synoptic situation. The TOVS and SSM/I retrieved parameters for the case of interest are then presented in sections 4 and 5

respectively. Finally, in section 6, the complementary nature of the information from these two types of satellite data is discussed. We show that the combination can be of considerable value for the monitoring of polar lows, which often occur in these regions during wintertime and which are difficult to forecast due to their small size and short lifetime.

2. The sensors and retrieval algorithms

2. 1. The TOVS instrument

2.1.1. Description. The TIROS-N Operational Vertical Sounder, which flies aboard NOAA satellites consists of three passive vertical sounding instruments (Smith et al.,1979): the High resolution Infrared Radiation Sounder (HIRS-2), a radiometer with 19 channels in the infrared and one in the visible; the Microwave Sounding Unit (MSU), a microwave radiometer with 4 channels in the vicinity of 55 GHz; and the Stratospheric Sounding Unit (SSU), a pressure-modulated infrared radiometer with 3 channels near 15 μm.

Table 1 gives the characteristics and primary use of observations made in the various spectral channels of the TOVS. The HIRS-2 ones are distributed along the whole infrared spectrum (from 3.7 to 15 μm). The ability of the 50 GHZ channels to penetrate clouds make them indispensable, since clouds are generally opaque to the infrared channels.

The spatial resolution of the infrared sounder is about 17 km at nadir whereas the spatial resolution of the microwave sounder is 100 km at nadir, the swath width being about 2400 km. Besides the TOVS instrument, there is also an imager aboard the NOAA satellites, the Advanced Very High Resolution Radiometer (AVHRR) with a spatial resolution of 1.1km . Normally two TIROS-N satellites operate simultaneously ; at low latitudes, each satellite observes a point on the earth every 12 hours, but at high latitudes, overlap between swaths allows more frequent sampling.

2.1.2. The retrieval algorithm. The TOVS retrieval algorithm used in this study is the Improved Initialization Inversion (3I) algorithm (Chedin and Scott, 1985 and Chedin et al., 1985), developed at Laboratoire de Meteorologie Dynamique. This method determines the following physical parameters : air mass type, temperature profiles (or geopotential thicknesses), thermal winds, microwave surface emissivity, cloud heights and amounts, total water content and relative humidities in 3 layers. Only HIRS-2 and MSU observations are currently used, so that the retrievals are obtained from the surface to a pressure level of 10 hPa (by adding SSU observations, it would be possible to reach 1 hPa).

The inversion relies upon *a priori* knowledge of the parameters (the atmospheric structure) and the associated calculated brightness temperatures for each channel of the vertical sounder. This *a priori* knowledge is in the TOVS Initial Guess Retrieval (TIGR) data set, created once and for all. Provided the observed brigthness temperatures correspond to clear areas, or have been properly "cleared" (decontaminated from clouds) by the so-called psi-method, the 3I procedure consists of two principal steps: first a search is made for the best initial guess solution in the TIGR data set ; finally the solution is obtained by a maximum *a posteriori* probability estimation procedure using the Jacobians associated with the initial guess, in the TIGR data set.

Retrievals of water vapor quantities (relative humidity, integrated water vapor) are obtained for 3 layers delimited by the levels 1000, 850, 500 and 300 hPa corresponding approximately to the center of HIRS-2 channels 10, 11, 12 weighting functions (Fig. 1). Following the temperature inversion, predicted brightness temperatures associated with the initial guess are corrected for the deviations between the initial and final temperature profiles. These new calculated brightness temperatures are then used as initial guess for water vapor and surface temperature retrievals. The method is based upon a simultaneous physical inversion of water vapor amounts and surface temperature (HIRS-2 channel 10 is sensitive to the surface temperature, and use is also made of HIRS-2 window-channels 8 and 18). Reliable water vapor retrievals become impossible when cloud coverage is large,

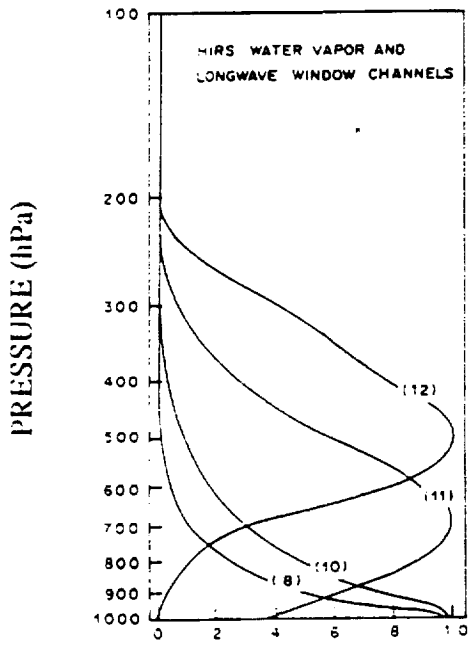

Fig. 1 : Weighting functions of the 6.3 μm ("water vapor") and 11 μm ("windows") HIRS-2 channels (from Smith et al., 1979).

i.e. greater than 60 %. In such cases, holes due to rejection by the algorithm appear in the retrieved water vapor fields (see e.g. Tahani et al., 1989).

All parameters are retrieved at a spatial resolution of 100 km. Quality control is incorporated into the procedure in order to detect and to reject either bad satellite data or bad retrievals. For this purpose, all retrievals pass a series of tests using the deviations between observed, initialized and retrieved profiles (Chedin, 1988). In cases with precipitation detected by MSU observations, retrievals must also be rejected (Chedin et al., 1989). In the arctic and subarctic environment, temperature profiles are obtained with good accuracy and most of the time compare well to data from radiosondes (Claud et al., 1991).

2.2. The SSM/I instrument

2.2.1. Description. The Special Sensor Microwave/Imager (SSM/I) was launched by the Defense Meteorological Satellite Program (DMSP) on June 19, 1987. This seven channel microwave radiometer measures upwelling polarized microwave radiation from the earth/atmosphere system at four frequencies : 19.35, 22.2, 37, and 85.5 GHz. Two polarizations, vertical (V) and horizontal (H), are available for each frequency, except for 22.2 GHz which has only vertical polarization. The spatial resolution ranges from 55 km at 19 GHz down to 15 km at 85 GHz. Further details concerning the instrument are given by Hollinger et al., (1987).

Radiation received by the SSM/I comes from three sources : atmospheric emission in the direction of the satellite, surface emission, and downward atmospheric emission reflected from the ocean surface. Changes in the total microwave radiance observed by a given channel are dominated by variations in the atmospheric transmittance and, to a lesser extent, by changes in the ocean surface emissivity due to wind-induced roughening and foam production. At SSM/I frequencies, the most important atmospheric attenuators/emittors are oxygen, water vapor and liquid water (Fig. 2).

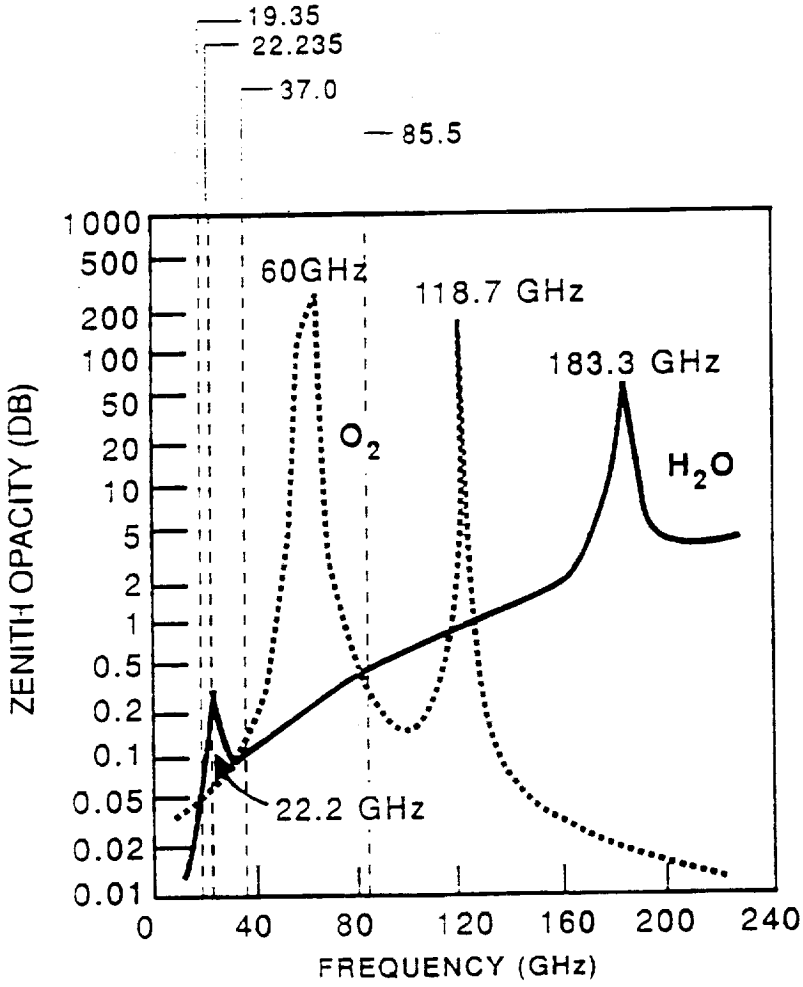

Fig. 2 : Illustration of the positions of SSM/I channels relative to oxygen and water vapor lines in the microwave spectrum (0 - 240 GHz), after Waters, 1976. The zenith opacity refers to the integrated column of a standard atmosphere.

Because each of the seven channels of the SSM/I responds differently to changes in integrated water vapor, integrated liquid water, surface wind speed, and certain "minor" parameters, it is possible to combine channel brightness temperatures in a way that is sensitive to a single parameter of interest and approximately orthogonal to the rest. The general problem of optimally retrieving environmental parameters from the SSM/I has been discussed in some detail by Petty (1990).

2.2.2. The retrieval algorithms. Here we confine our attention to two parameters which are known to be measurable by the SSM/I with reasonable reliability : the integrated water vapor content and the surface wind speed. These are both obtained with a spatial resolution of about 50 km, though the sampling density is somewhat higher. Because of the relatively small amounts of water vapor and liquid water encountered in polar air masses, simple linear water vapor and wind speed algorithms are quite satisfactory for the purposes of this study.

We have developed an algorithm for integrated water vapor specifically intended for use in the polar oceanic regions considered in this study; it depends simply on the difference between the 22V and 19V channel brightness temperatures :

$$IWV\ (kg/m^2) = 0.98\ (TB22V-TB19V) -3.5 \qquad (1)$$

where TB19V stands for the 19 GHz brightness temperature in vertical polarization, and TB22V, 22 GHz brightness temperature in vertical polarization.

The coefficients for the above relationship were derived from the analytic brightness temperature model of Petty (1990), assuming atmospheric water vapor and temperature profiles characteristic of air masses with less than 20 kg/m^2 of total water vapor, as determined from the global radiosonde statistics presented by Petty (1990). An additional assumption was that the mean surface wind speed was near 10 m/s and that cloud water in

the amount of approximately 0.1 kg/m^2 was present and had a temperature near 270 K. Since the brightness temperature difference appearing in (1) is only weakly sensitive to any of these assumptions, we expect that maximum uncertainties in retrieved IWV do not exceed 1-2 kg/m^2 for the cases considered and are probably less, provided only that IWV does not greatly exceed 15 kg/m^2. For higher values of IWV, the assumption of linearity fails, and (1) will give an increasingly serious underestimate of the true water vapor amount.

For surface wind speed determination, we used an adaptation of the algorithm of Goodberlet et al., (1989), who derived the following coefficients via a "weighted linear regression" of 708 buoy wind speeds against the coincident SSM/I brightness temperatures from the 19V, 22V, 37V, and 37H channels:

$$SW\ (m/s) = 147.90 + 1.0969\ TB19V - 0.4555\ TB22V - 1.76\ TB37V + 0.786\ TB37H \qquad (2)$$

SW is the wind speed referenced to a height of 19.5 m above the surface. Our own extension of this algorithm includes spatial smoothing and slightly modified criteria for flagging regions contaminated by rainfall. These minor modifications are described more fully by Petty (1990).

Under rain free conditions, a standard error of about 2 m/s was reported by Goodberlet et al., (1989) for winds in the range 3-25 m/s. This error statistics may not be representative for the regions and extreme meteorological conditions considered in the present study. However, our own experience suggests that the retrieved values are reasonable, though with an apparent tendency to underestimate wind speeds above 25 m/s.

For completeness, we also examined two other parameters which can be inferred from SSM/I data, the cloud liquid water content and an index of scattering by large ice particles.

This index is indicative of convection. Large ice particles, graupel or hail, are required for a substantial signal. The algorithms used have been validated more qualitatively than quantitatively. For a complete description, the reader is again referred to Petty (1990).

3. Synoptic description of the 29 February to 1 March 1988 situation

Maps of the European Meteorological Bulletin (EMB, see references) as well as AVHRR images have been used for describing the synoptic situation. The three day period from 29 February to 1 March 1988 was characterized by a cold air outbreak which had abruptly begun over the Norwegian and North Seas on February 28. The northerly flow associated with the cold air outbreak was reinforced during this period by a strong east-west pressure gradient accompanying a cyclone over Denmark and southern Sweden with a central pressure 980 hPa and a strong anticyclone situated south of Greenland with a central pressure of 1050 hPa on 28 February at 1200 UTC (Fig. 3a) . An upper level disturbance (500 hPa) was associated with the cold air region delimited by the fronts at the surface.

During February 29, the region covered by cold air expanded southward (Fig. 3b); the front extending from northern Norway to Novaya Zemlya evolved into a low center in the Barents Sea on the 1st of March. A stationary front lay west of Great Britain. Surface winds were quite strong in frontal areas as well as in the North Sea. At 1200 UTC, almost the entire area was cloudy except a region close to Greenland. The 500 hPa disturbance moved southward together with the cold air at the surface.

Fig. 4 displays the AVHRR image in channel 4 at about 0900 UTC ; it indicates the presence of a frontal cirrus band between Iceland and the British Isles. Another cirrus band is visible over Scandinavia. Most of the region corresponding to the strong pressure gradient is covered with cumulonimbus and well-defined cloud streets can be seen west of Spitzbergen. Note also the formation of a vortex at about 76 °N, 13 °E.

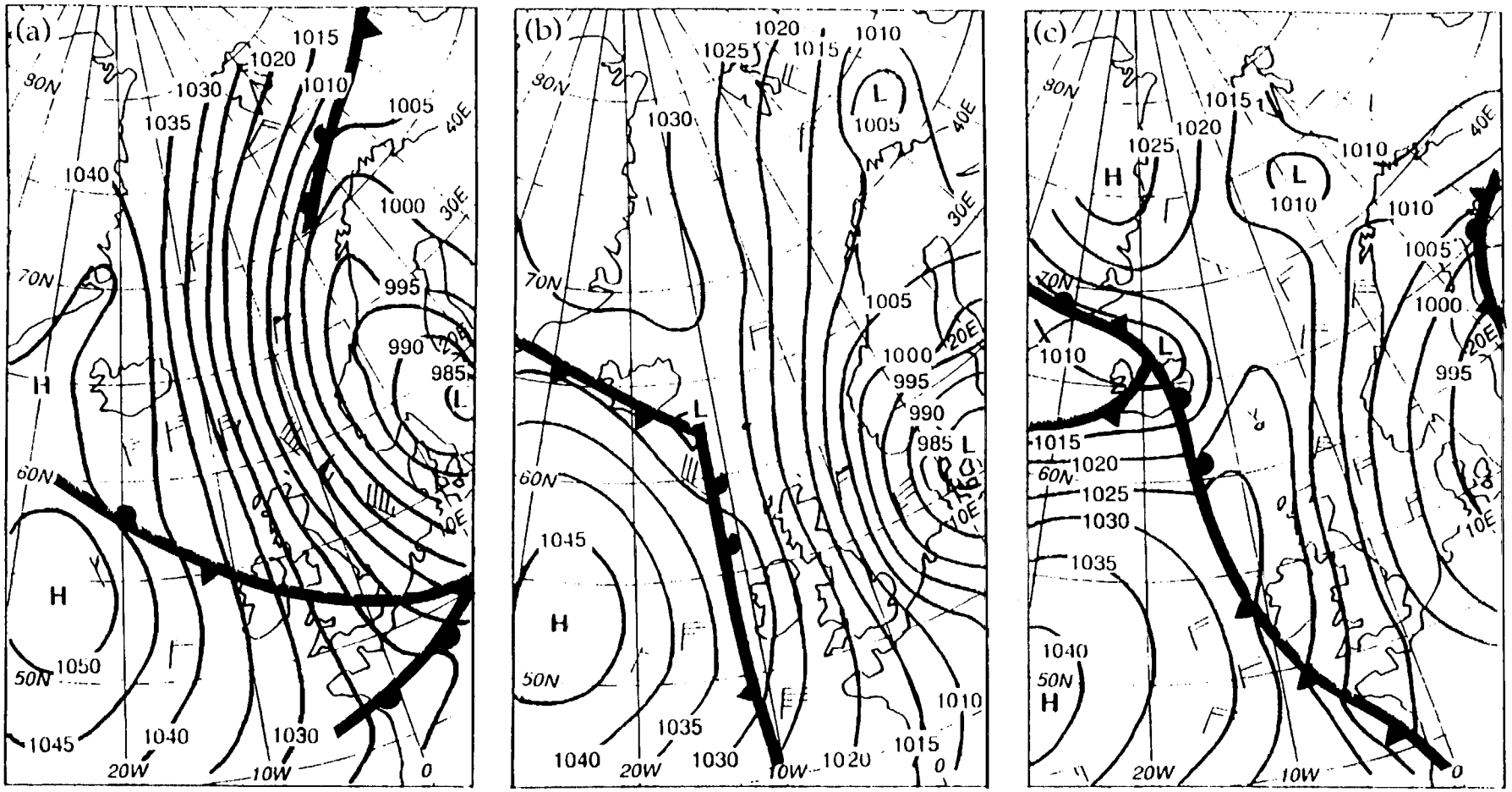

Fig. 3 : Surface chart (redrawn from the European Meteorological Bulletin) at 1200 UTC

a. 28 February 1988

b. 29 February 1988

c. 1 March 1988

On March 1 at 1200 UTC (Fig. 3c), a col developed northeast of Iceland in a trough connecting two lows, one over Iceland, the other close to Bear Island. The cold front, which by now had reached the African coast, was weakening. The area of warm air over the Atlantic Ocean had moved eastward and the winds over the Norwegian and North Seas were much weaker than on the previous day.

The AVHRR image in channel 4 at 0845 UTC (not shown) gave further indications of the evolution over the previous 24 hr : both the cirrus band over Scandinavia and the one between the British Isles and Iceland were seen to have moved eastward, and while the cloud streets west of Spitzbergen were less dramatic, the small vortex first identified on the 29th had become much more pronounced and was bounded on the east by a cloud-free area. It is likely that this system corresponds to a polar low identified at the Norwegian Meteorological Institute (DNMI) at 1200 UTC (position : 74 °N, 18 °E).

4. Results of the 3I algorithm

Three NOAA-10 passes covering the area were obtained from the Norwegian Meteorological Institute (DNMI) for 29 February at 0856 UTC, 29 February at 1707 UTC, and 1 March at 0833 UTC. Each pass is of about 10 minutes duration. Cloud related results, geopotential thicknesses and water vapor retrievals are discussed below.

4.1. Cloud related results

Cloud detection results for the 29 February pass are presented in Fig. 5 (these correspond to the AVHRR image in Fig. 4). The situation is found to be quite cloudy by the 3I algorithm, as would be expected based on the AVHRR image. The high cloud systems over Iceland and Scandinavia have been well detected. The 3I cloud top pressure is in the range 300-400 hPa, which seems reasonable, though it cannot be independently verified. Rather low clouds over the Atlantic Ocean west of the polar front have also been well detected, and the top pressure deduced from 3I is in the range 600-800 hPa, which is realistic in view of the synoptic situation and the infrared image (Fig. 4). Nevertheless,

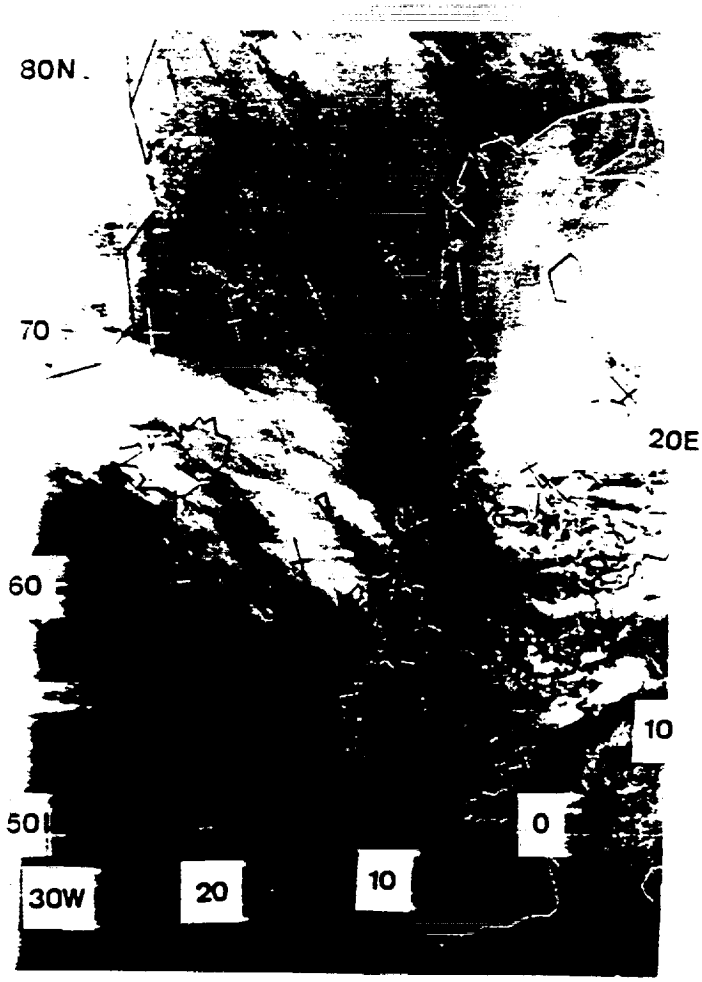

Fig. 4 : AVHRR image, channel 4, 29 February 1988, 0856 UTC (by the courtesy of the Royal Dutch Meteorological Institute).

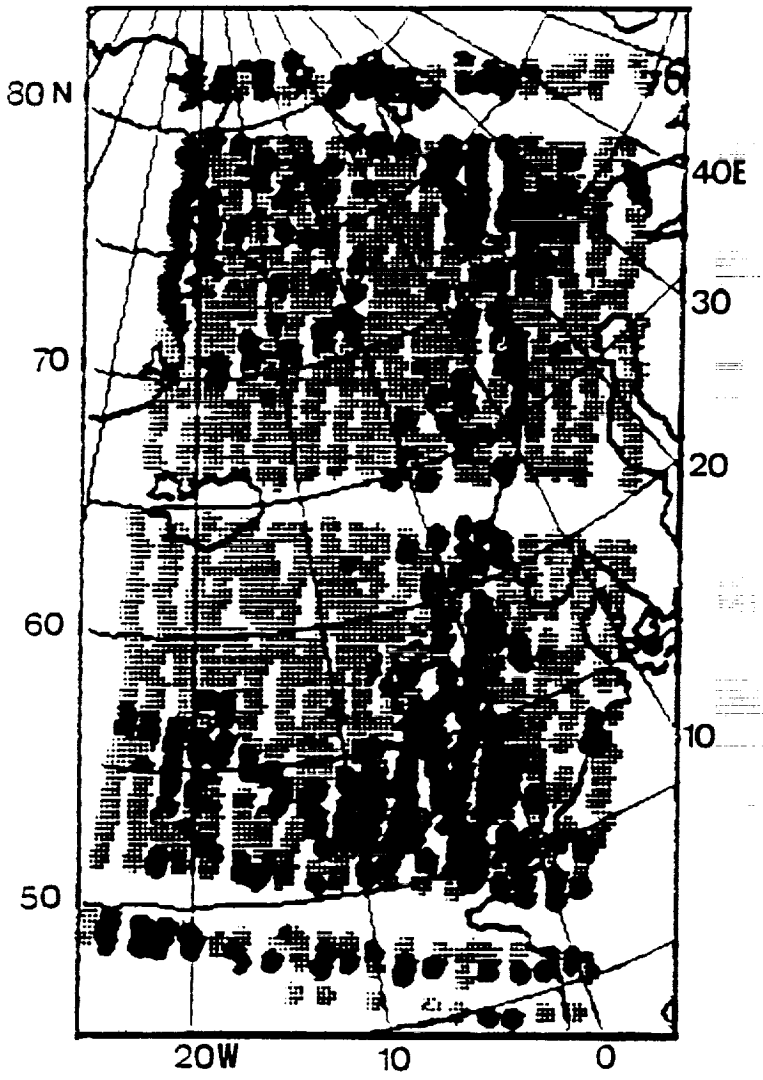

Fig. 5 : 3I cloud detection results, 29 February 1988, 0856 UTC. Clear areas are displayed by dark dots, cloudy ones are shaded grey. Blank zones correspond to calibration zones.

some clear areas are identified by the 3I system in regions where there are obviously cumulonimbus created by surface heating. The failure to detect these clouds is probably due to the fact that they do not cover the whole box (cloud detection tests are performed within each HIRS-2 spot, but 2 clear spots are sufficient in a box to declare it clear). For the following passes, these remarks also apply, the large cloud systems being well detected, except again most of the cumulonimbus clouds.

4.2. Geopotential thicknesses

Fig. 6a-c display the 1000-500 hPa geopotential thicknesses. On February 29 (Fig. 6a), two general regions of large thickness gradient can be identified : one corresponds to the frontal zone extending from Greenland across Iceland to just west of Ireland (Fig. 2a, weather map); the other includes the region poleward of 65 °N. The latter region is characterized by two north-south axes of lower thickness near 5 °W and 20 °E respectively; these features persist throughout the following 24 hr (Fig. 6 b, c), and are seen to drift eastward by only 5 degrees longitude during this period.

Unfortunately, the full extent of the cold air cannot be seen in the evening pass on the 29th, since this pass only covers a portion of the North Sea. However, on the 1st of March, the southward advancement of the cold air has been halted : the front between Greenland and the British Isles has moved eastward of its position on the previous day and the front in the Barents Sea is sharper.

A striking feature, however, is the large number of rejections, especially for 29 February and 1 March passes in the Atlantic Ocean and in the North Sea. In the case of the North Sea, these rejections are due to precipitation. Over the Atlantic Ocean, the situations found in the TIGR data set were not close enough to the observed situations and were rejected by the quality control tests (see section 2.1.2).

The 3I inferred 1000-500 hPa geopotential thicknesses for these three passes were found to generally agree with the analyses (not shown) provided by the ECMWF (European Center

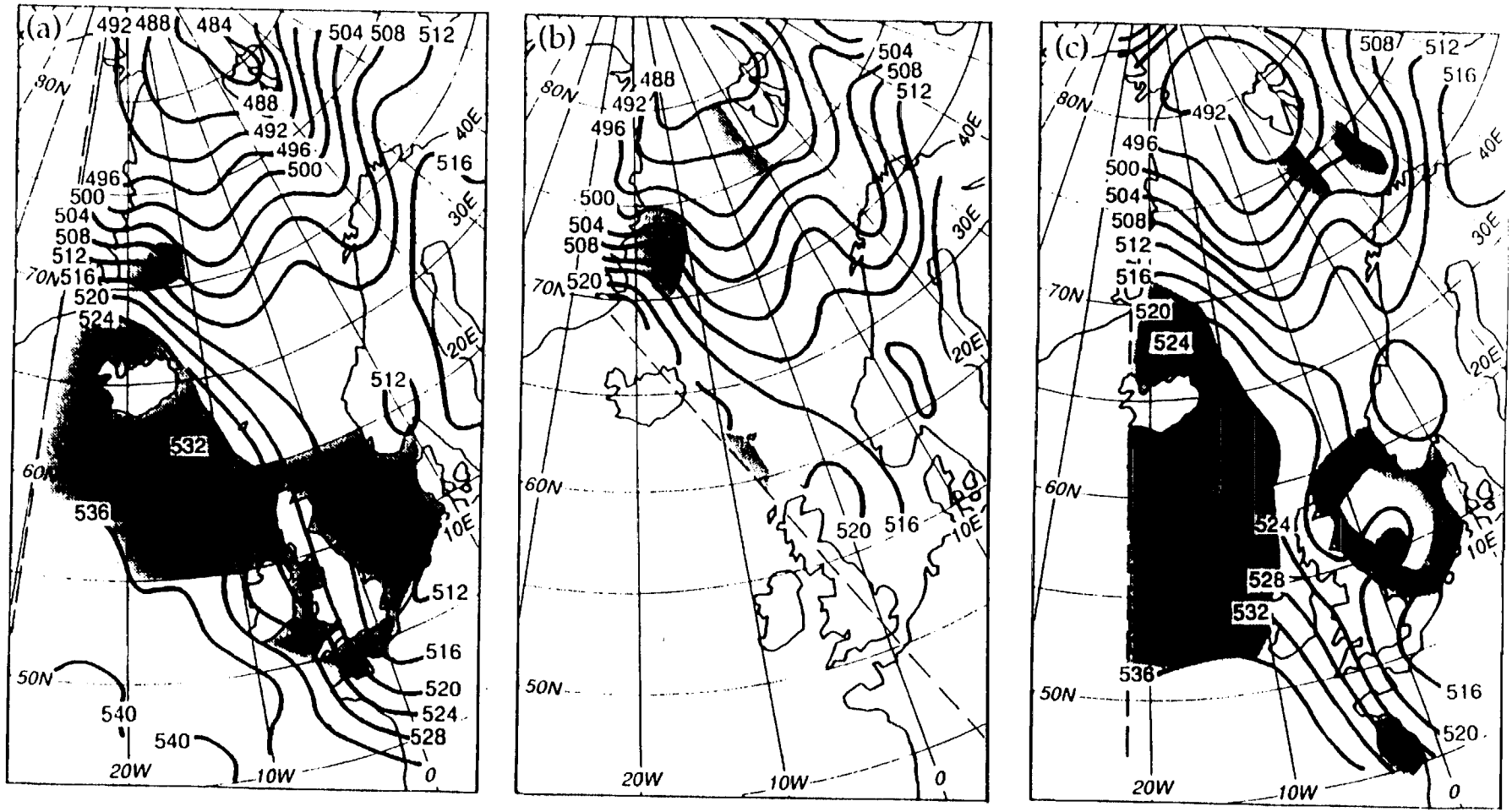

Fig. 6 : 1000-500 hPa 31 geopotential thicknesses (in decameter) :

a. 29 February 1988, 0856 UTC

b. 29 February 1988, 1707 UTC

c. 1 March 1988, 0833 UTC

Areas of rejections (section 4.2) are shaded grey. The dashed line represents the swath edge.

for Medium range Weather Forecasts) ; similar large-scale structures appear though the cold tongues on both sides of Spitzbergen are less pronounced on the ECMWF products.

The 1000-850 hPa geopotential thickness field (Fig. 7) on the morning of 29 February is qualitatively very similar to the corresponding 1000-500 hPa thickness field. Note however the presence of a tongue of warm air extending from England to about 66 °N just off the western coast of Norway.

The 3I derived 500-300 hPa geopotential thicknesses displayed in Fig. 8 for the same pass again show the gradient associated with the front extending from Greenland to west of Ireland.

4.3. Water vapor

Total retrieved water vapor content is displayed in Fig. 9a-b for the morning of 29 February and 1 March, respectively : in several regions, no determination has been performed, due to either rejections in the temperature and/or water vapor profiles calculation or cloudiness larger than 60%.

For both passes, two regions can be distinguished : the warm air side of the front is seen to be generally characterized by water vapor values of 8-12 kg/m^2, while the cold air mass north and east of the British Isles is considerably drier. In this latter region, the warmest air in the vicinity of 60 °N, 10 °W is characterized by water vapor content of about 7 kg/m^2, while the coldest air near the ice edge presents water vapor content as low as 1 kg/m^2. Note that the fields of retrieved integrated water vapor values are found to be qualitatively very similar to the 1000-500 hPa geopotential thickness fields, including even the two thickness tongues both sides of Spitzbergen described earlier.

It is also possible to derive the water vapor content for 3 separate layers : 1000-850 ; 850-500 ; 500-300 hPa. Most of the water vapor (from 30 to 50 %) is found in the layer 1000-850 hPa (see Fig. 10 a-b), with values ranging from 0.5 to 5.5 kg/m^2. The warm air advection west of Norway observed in the thicknesses is also apparent in the water vapor content which has a relative maximum of 2.5 kg/m^2. In the 800-500 hPa layer (Fig. 11a-

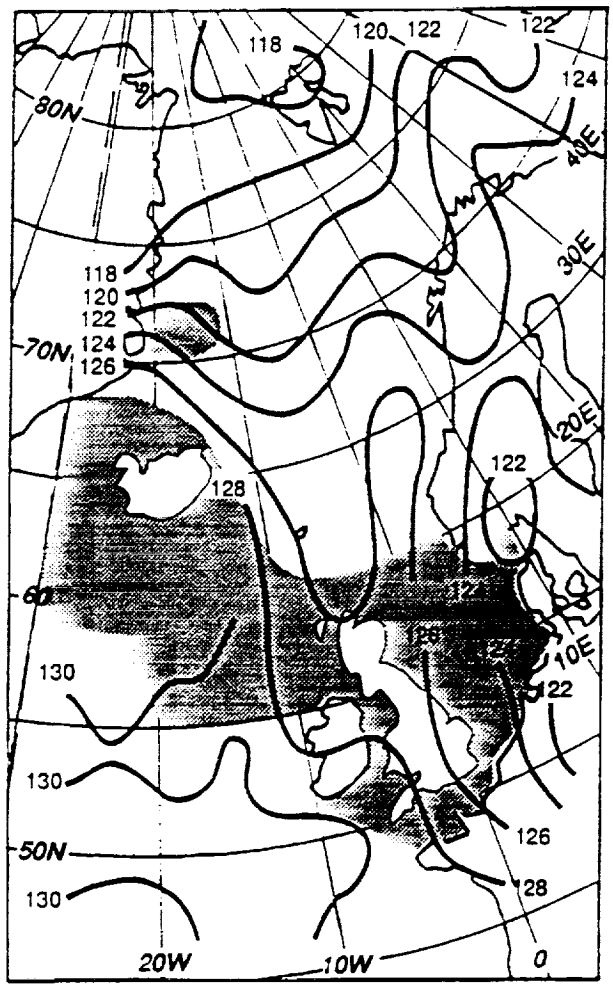

Fig. 7 : 1000-850 hPa 3I geopotential thicknesses (in decameter), 29 February 1988, 0856 UTC. Areas of rejections are shaded grey.

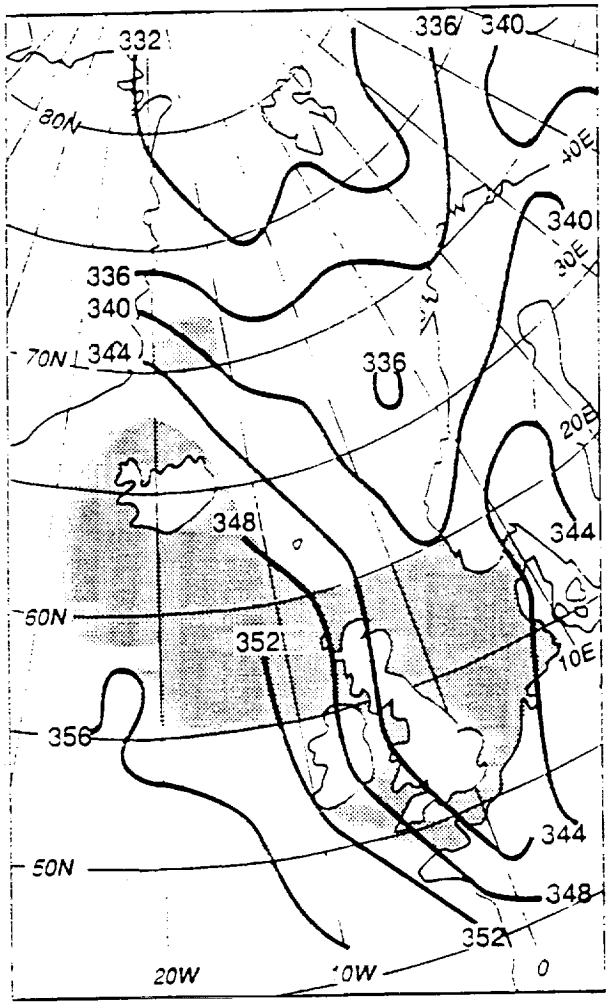

Fig. 8 : Same as Fig. 7, but 500-300 hPa.

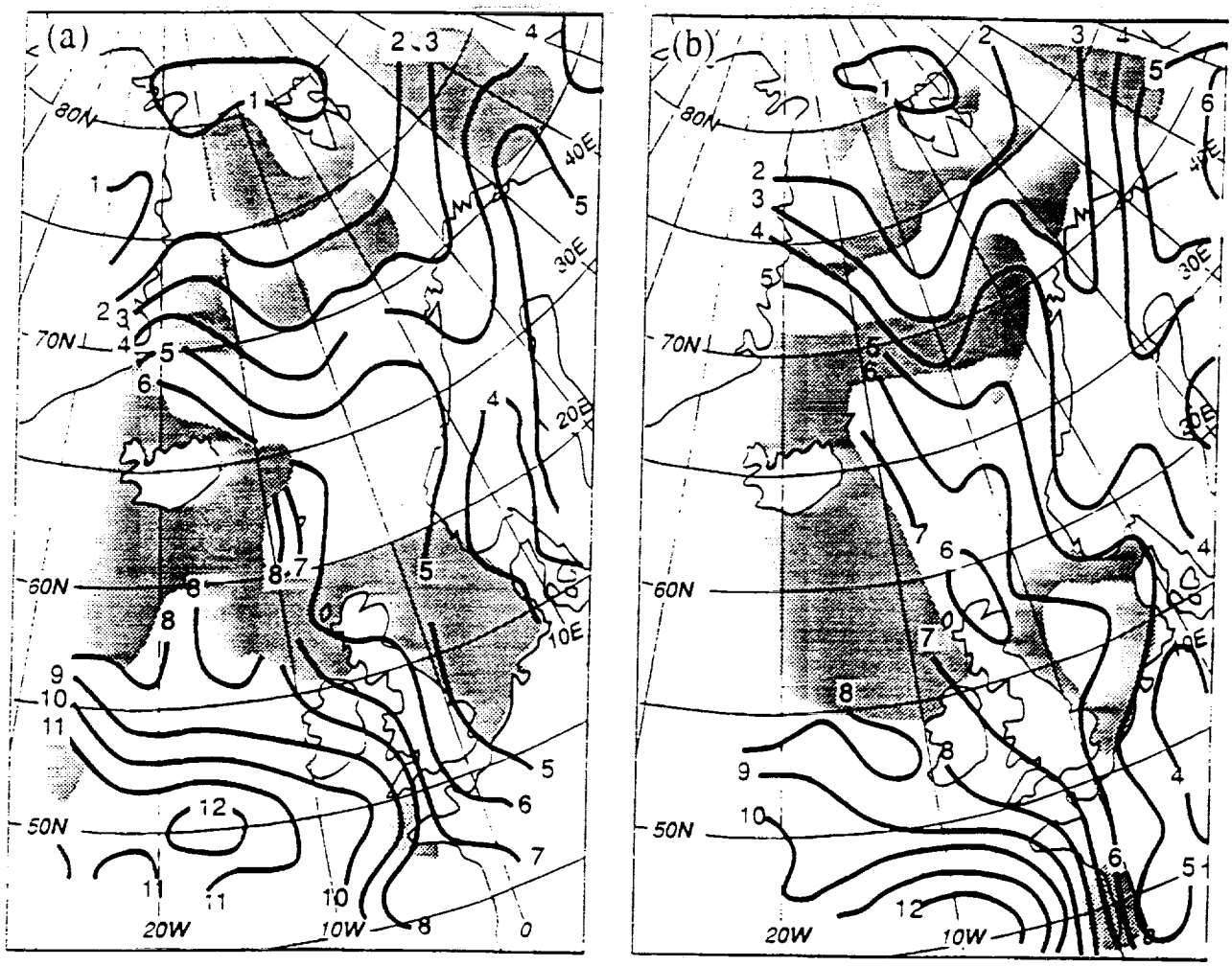

Fig. 9 : 3I total precipitable water (in kg/m^2)

a. 29 February 1988, 0856 UTC

b. 1 March 1988, 0833 UTC

Areas of rejections are shaded grey.

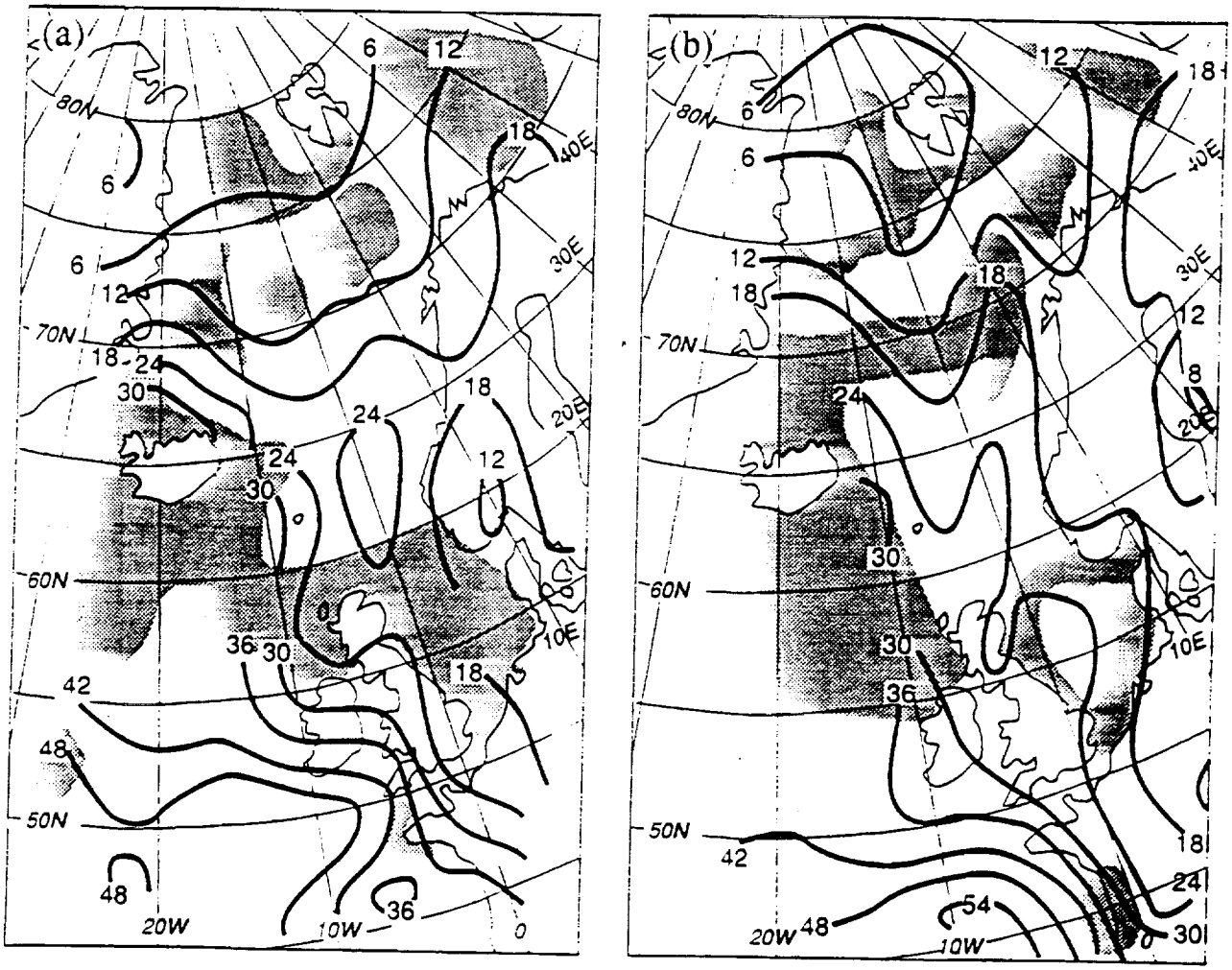

Fig. 10 : same as 9 but for the layer 1000-850 hPa ; values are muliplied by 10

b), values range from 1 to 6 kg/m^2, which represents about 40 to 50 % of the total content, but above 500 hPa, values are extremely low (less than 0.5 kg/m^2).

In relatively moist areas, both the lower and the intermediate layers contain 40 to 50 % of the water vapor, whereas a smaller percentage (30 %) is found in the lowest layer in the very dry areas.

If we consider now the evolution from the 1st orbit to the 3rd one, layer by layer, it appears that the temporal evolution in the 1000-850 hPa layer is very weak for almost the whole pass, except over the Atlantic Ocean north of Spain, where the values increase from 3.6 to 5.4 kg/m^2. The same tendencies appear for the 850-500 hPa layer.

5. Analysis of SSM/I parameters

For this period, there were several SSM/I passes covering about the same area as the TOVS observations (Table 2). Poleward of 57 °N, successive SSM/I swaths overlap, so that there is complete geographic coverage twice daily. Five SSM/I composites, each consisting of 3 or 4 overlapping swaths (28 February evening, 29 February, early morning and evening, 1 March, early morning and evening) are considered for presenting the SSM/I results.

5.1. Water vapor.

Selected composite SSM/I water retrievals are plotted in Fig. 12, using the same contour intervals and map projections as for the TOVS derived products in Fig. 9. In contrast to the TOVS, the SSM/I is limited to retrieving integrated water vapor over ice free water ; a dashed line is used to indicate the edge of the pack ice beyond which no SSM/I data can be used.

The SSM/I integrated water vapor image on the 28th (not shown) exhibits a characteristic water vapor maximum ahead of the polar front, accompanied by a sharp decrease across it. Quickly, the dry air advances southward, eastward and westward during the early morning of 29 February. The British Isles are at that time entirely in the cold air which has even

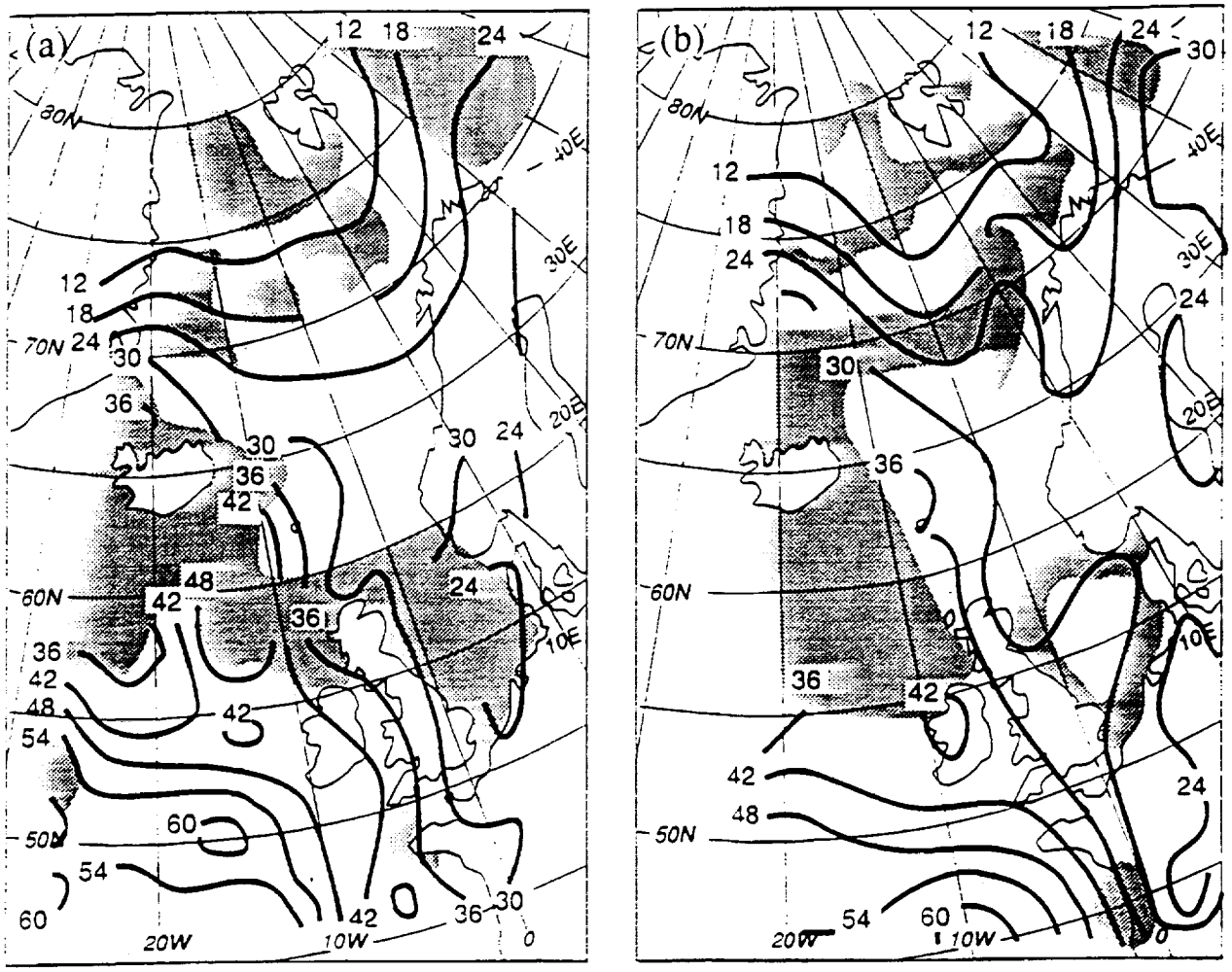

Fig. 11 : same as 10 but for the layer 850-500 hPa

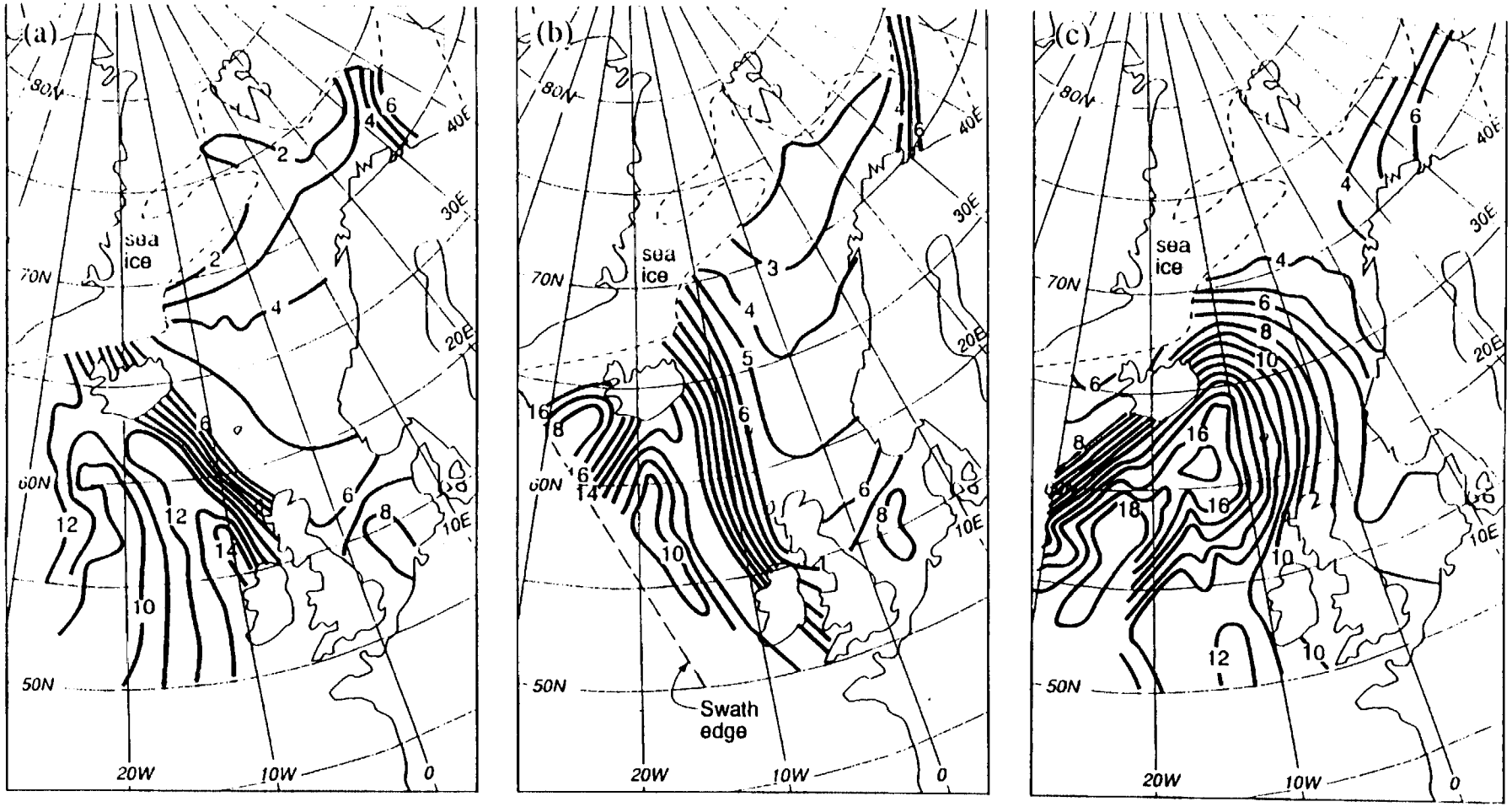

Fig. 12 : Composite SSM/I imagery of the cold air outbreak. Integrated water vapor derived from Eqn. 1. Values range from 1 to 15 kg/m^2. The dashed line represents approximately the sea ice edge.

a. 29 February 1988, easternmost swath is from 1624 UTC, westernmost is from 2124 UTC.

b. 1 March 1988, easternmost swath is from 0041 UTC, westernmost is from 0542 UTC.

c. 1 March 1988, easternmost swath is from 1608 UTC, westernmost is from 2111 UTC.

reached France. Southeast of Iceland, the water vapor content has increased dramatically in the warm sector of the incipient wave on the polar front (63 °N, 13 °W).

The SSM/I retrievals for the evening of 29 February (Fig. 12a) and the early morning of 1 March (Fig. 12b) clearly confirm the presence of a strong dry air incursion over the Norwegian Sea, with extremely low water vapor values covering most of the open ocean north of 60 °N. Throughout the region covered by the cold air mass, SSM/I retrieved water vapor values show a week north-south gradient in water vapor amount, ranging from 1-2 kg/m^2 over the open water just south of Spitzbergen up to about 6-7 kg/m^2 near the advancing edge of the front extending from Greenland to the British Isles.

The SSM/I retrievals also clearly reveal the sharp boundary between the arctic air and the somewhat moister air mass to the south and west of Iceland and the British Isles, respectively. Based on the work of Katsaros et al. (1989) and McMurdie and Katsaros (1985), who found that a surface cold front is typically located on the moist edge of the strongest gradient in the integrated water vapor field, these maps suggest a surface frontal position extending from southern Iceland to northern Ireland at around 2000 UTC 29 February (Fig.12a) and then from the northeastern tip of Iceland to central Ireland near 0530 UTC 1 March (Fig. 12b). These positions are in fact found to be generally consistent with the operational synoptic analyses presented for 1200 UTC on 29 February and 1 March (Fig. 3 b and 3 c).

On the warm side of the front, the SSM/I data also show a relatively narrow water vapor maximum of 12-14 kg/m^2 ; such a maximum is commonly observed in this position near a surface front and is believed to result from a combination of enhanced convergence and potential advection of moist air along the frontal zone.

Throughout this period, the Barents Sea (characterized by a low surface pressure), remains relatively moist (4 to 6 kg/m^2), compared to the region of the cold air outbreak.

5.2. Winds.

On the 28th of February, SSM/I surface winds (not shown) are strong in the cold air region (greater than 16 m/s), but in a large area over the North and Norwegian Seas, they could not be determined because of precipitation. There is a sharp gradient in the winds across the two frontal zones, one extending from southeast of Iceland to the British Isles, the other from northern Norway to Novaya Zemlya. These strong winds correspond to strong pressure gradients appearing in the EMB map at 1200 UTC, where wind speeds of 30 m/s are reported in the southern part of the Norwegian Sea. However, some SSM/I winds in the Greenland Sea are higher than suggested by the EMB pressure fields. A similar feature has been observed with a different algorithm in mid-latitude and can be explained by the fact that SSM/I wind speeds would be sensitive to surface roughness variations due for example to atmospheric stratification or sea state not directly related to the wind (swell, current effects).

Values in the range 4-12 m/s occur in the westernmost moist areas and seem in fair agreement with EMB wind reports at 1200 UTC.

The situation during the early morning of 29 February (not shown) does not show much evolution since the previous day, with still strong gradients across the frontal zones. However, less precipitation is found in the Norwegian Sea, but more in the North Sea. An area near 65 °N, 10 °W is found to have lower wind speeds (4-8 m/s) than some hours earlier, when they were larger than 14 m/s. These values are difficult to validate, since there are no surface reports in this area at that time (0555 UTC). However, at 1200 UTC, EMB analysis reports low wind speeds and slack pressure gradients.

On the 29th of February, evening overpasses (Fig. 13a), precipitation occurs only in the frontal area between Iceland and the British Isles, so the winds can be determined for almost the whole swaths. The contrast between wind speeds in the cold air and in the warm air tend to be weaker. Largest SSM/I wind speed values (in the range 10-14 m/s) are still found in the area of cold air (Norwegian and North Seas), but also west of the front

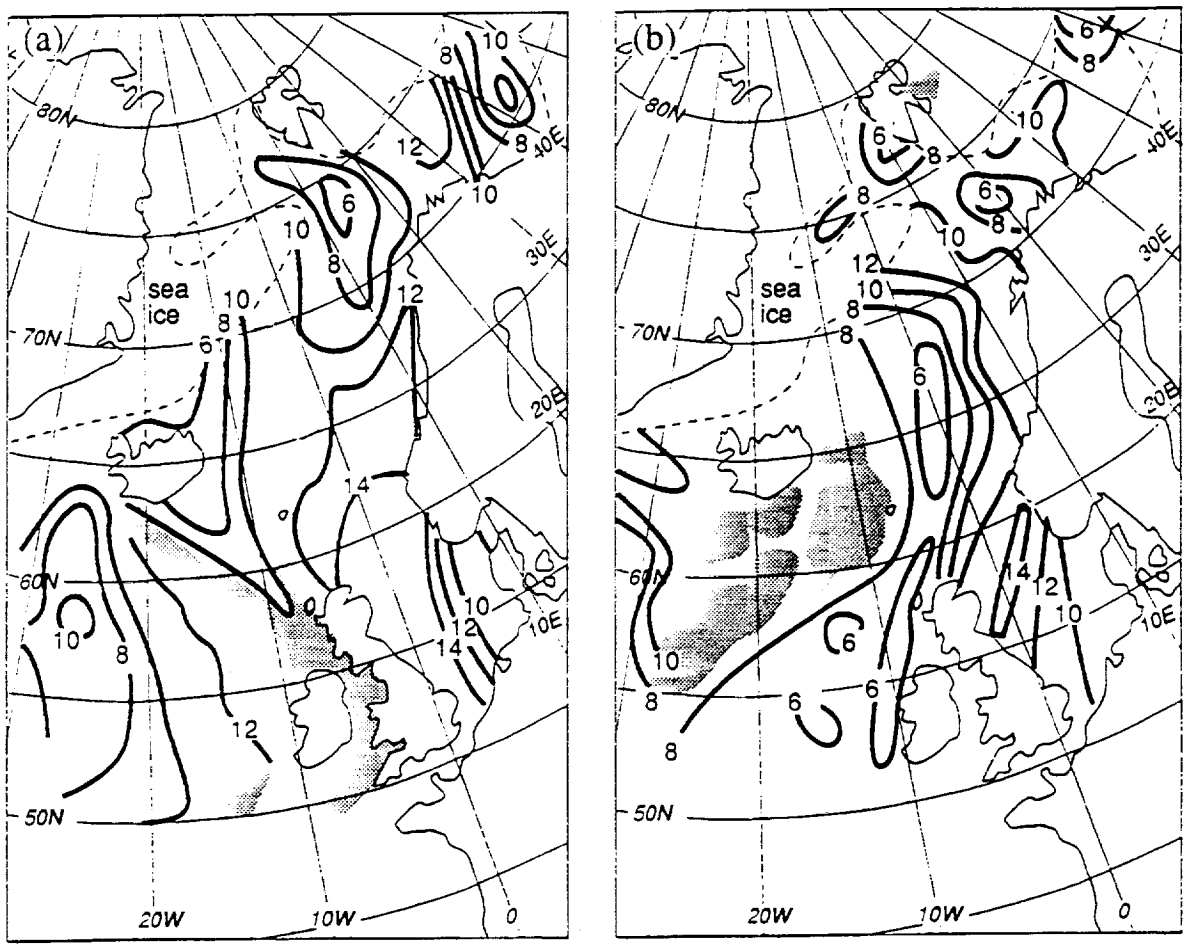

Fig. 13 : same as Fig. 12, but for surface wind speeds, derived from Eq..2 and only for evening overpasses of 29 February (a) and 1 March (b). Values range from 0 to 20 m/s. The absence of determination (grey areas over sea) indicates the presence of precipitation. The dashed line represents the approximate sea ice edge.

extending from Iceland to the British Isles. SSM/I wind speed values in the Barents Sea (8 to 12 m/s) are greater than what one might infer from the pressure patterns appearing in the EMB maps (Fig. 3b, 29 February, 1200 UTC). Reasonable agreement is, however, found west of the Barents Sea between SSM/I wind speeds and wind reports (e.g. 8 m/s at 75 °N, 20 °E, and 10 m/s at 76 °N and 25 °E). These differences in agreement may be due to differences in stratification (in the Barents Sea, the southerly winds bring warm air over the ocean, while west of this area, cold air streams off the arctic sea ice over warmer water), which results in different efficiency of momentum transfer through the atmospheric boundary layer.

On the 1st of March early morning, SSM/I wind speeds (not shown) in the Barents Sea are in better agreement with the EMB analysis.The area with lower wind speeds southeast of Iceland has extended eastward whereas the area of high wind speeds over the Norwegian Sea is smaller. This wind distribution agrees well with the EMB analysis at 0000 UTC (not shown).

In the evening of the 1st of March (Fig. 13b), rather large values (greater than 12m/s) are only found in small zones between Norway and the British Isles (EMB reports at 1200 UTC a wind speed of 10 m/s at 59 °N, 25 °W).

5.3. Signature of a polar low.

We have also looked at two other parameters derived from SSM/I, the cloud liquid water content and an index of scattering by large ice particles at 85 GHz. The valuable complementary information provided by these two parameters will be illustrated with the detection of a polar low on March 1, 0401 UTC. In Fig. 14 a which displays cloud liquid water at that time, a large region of liquid water coincides with the region of cumulus advection already seen in the AVHRR image on 29 February at about 0900 UTC (Fig. 4) and a linear feature is identifiable between 72 and 75 °N and at about 17 °E. In Fig. 14 b, the scattering index delineates this feature more clearly along with the more intense convective clouds close to the Norwegian coast. The detection of this polar low is

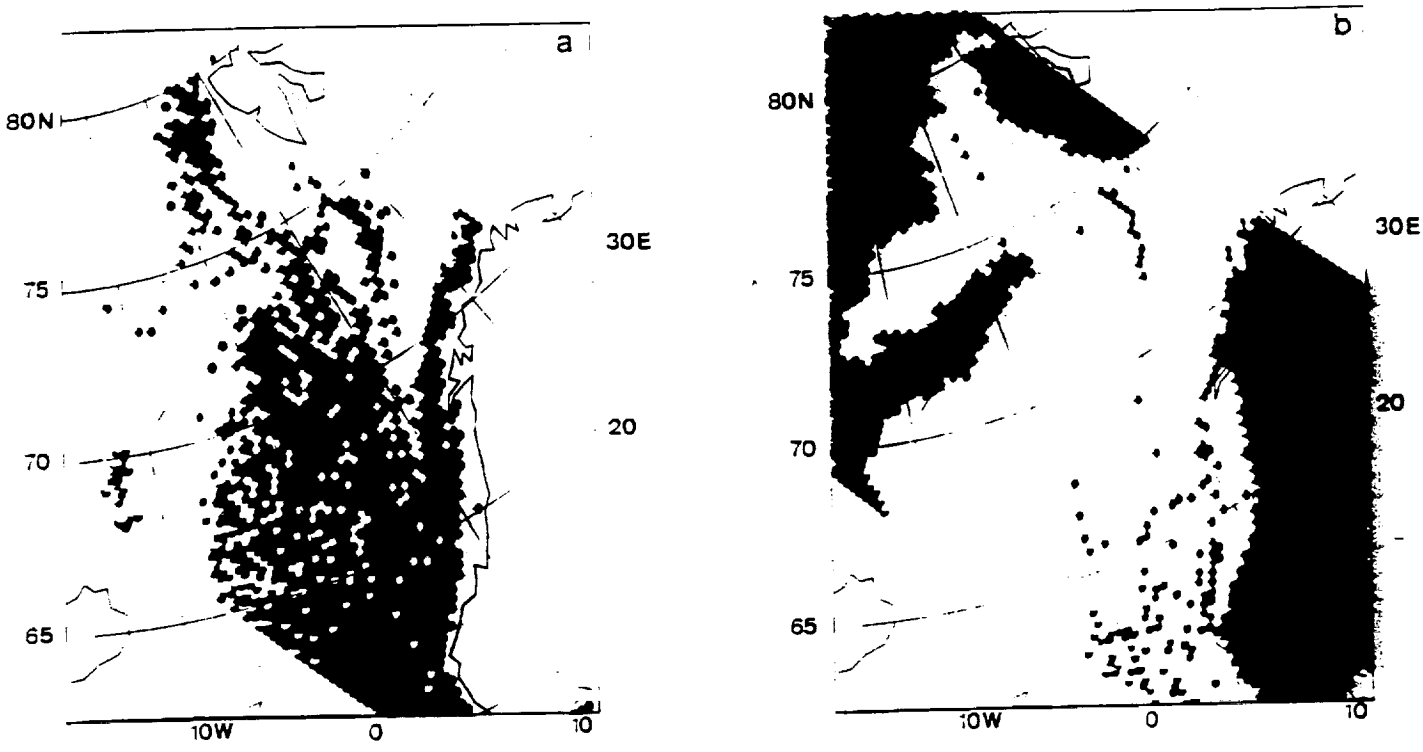

Fig.14 : Cloud liquid water (a) and scattering index by large ice particles (b) for SSM/I pass 3602, 1 March 1988, 0401 UTC. A polar low is identifiable between 72 and 75 N at about 17 E. Note that the intense convective clouds close to the Norwegian Sea are well delineated by the scattering index.

corroborated by the AVHRR image on the same day at 0845 UTC (not shown) and by the DNMI analysis, which identified this low at 1200 UTC at a position of 74 °N, 18 °E. In the SSM/I evening passes of March 1, there is no longer a signature (nor does DNMI list it any longer at 1800 UTC), one can surmise that it has either disappeared or is very weak.

6. Discussion

We have used both TOVS and SSM/I observations to study a cold air outbreak over the Norwegian Sea. Each instrument gives a special view of the weather system: the TOVS instrument provides a vertical description of the atmosphere in terms of temperature, moisture and cloud cover at a coarse spatial resolution (100 km), whereas the SSM/I instrument yields the integrated water vapor content and the surface wind speed at a higher spatial resolution (50 km). Moreover, the sensitivity of SSM/I to cloud liquid water and scattering by large ice particles makes it a powerful instrument for detecting embedded convection.

Comparing water vapor fields obtained from SSM/I and TOVS, one sees reasonable qualitative agreement for large-scale structures, in spite of time difference and of a significant number of rejections for TOVS derived water vapor. In regions where the paucity of conventional observations makes validation difficult, it is reassuring to have two independent instruments produce similar large-scale features. However, SSM/I shows much sharper gradients and generally more detailed subsynoptic structure, due largely to its better spatial resolution and its more complete coverage (SSM/I determines integrated water vapor content through clouds and rain). Throughout the region covered by the cold air mass, both SSM/I and TOVS show a weak north-south gradient in water vapor amount, but unlike the TOVS retrievals, the SSM/I ones clearly reveal the sharp gradient between the arctic air and the moister air south and west of the polar front.The TOVS retrievals yield only marginal evidence for the front related features in the water vapor fields, because of its

less favorable spatial resolution and the problem of cloud contamination throughout most of the vicinity of the front.

The 3I water vapor fields are found to be qualitatively very similar to the geopotential thickness fields of the same layer (including even the two tongues described in section 4.2). This observation is consistent with the expectation that cold air will generally be drier than warm air. On the other hand, the possibility exists that some of the similarities between the TOVS thickness and water vapor fields are an artifact of the retrieval. The fact that SSM/I water vapor retrievals show significantly less structural similarity to the TOVS thickness field would indicate that the second explanation is valid. However, the large number of rejections in the TOVS water vapor field may also have contributed to these similarities.

Quantitative comparisons between TOVS and SSM/I integrated water vapor content give on average a root mean square difference of 20 to 30 % of the mean TOVS values. Given that only a few conventional measurements are obtained over the area of interest, and that these measurements may not be representative for large areas, SSM/I and TOVS humidity estimates which are of comparable quality to radiosonde measurements could be important for meteorological purposes as underlined by several authors for TOVS (Illari 1989, Zhang 1989). These authors mention that the impact of satellite derived humidity parameters on humidity analysis are particularly important for data-sparse areas over the ocean.

SSM/I has the advantage of providing integrated water vapor content over open ocean in spite of cloudiness and rain (if not too intense). From TOVS data, no water vapor determination is performed in presence of rain or if the cloud cover is substantial, but 3I provides water vapor content over sea ice and land, where SSM/I can not discriminate the water vapor signal from the background. There is currently little validation of this parameter over sea ice, but the very low amounts found look reasonable. Over land, comparisons between TOVS dérived integrated water content and radiosonde or microwave

ground-based radiometers inferred content show that the difference in the estimation is about 20 % rms (Tahani, 1991). The coupling of both TOVS and SSM/I allows one to obtain "quasi-continuous" fields of water vapor in space, which are required for numerous meteorological applications.

Moreover, some information about the vertical distribution (3 separate layers : 1000-850, 850-500, and 500-300 hPa) can be obtained with TOVS. Even coarse vertical resolution gives insight into the physical processes involved.

Surface wind speeds derived from SSM/I, although sometimes stronger than what would be expected from conventional reports, appear to be realistic when compared to weather maps. It is nevertheless true that regions of a swath contaminated by rain (i.e. most of the time, the interesting parts of weather systems) are eliminated, which represents a shortcoming. However, regions of high wind speeds far enough from fronts are well delineated as shown in this study.

A polar low has been identified by two different parameters deduced from SSM/I (cloud liquid water and scattering by large ice particles). This polar low was undetected by TOVS observations and there is no signature of it on the surface analyses because of its small spatial scale and its very short lifetime. Further work dedicated to polar lows detection confirms this potential of SSM/I observations (to be published). An earlier study mentioned the utility of multispectral microwave radiances for analyzing these disturbances (Gloersen et al., 1989), and more particularly the 18 and 37 GHZ frequencies (two frequencies avalaible on the Scanning Multichannel Microwave Radiometer onboard the Seasat and Nimbus-7 satellites). There is no doubt that the high spatial resolution as well as the unique properties of the SSM/I 85 GHz channels added to the 19 and 37 GHz channels makes SSM/I a remarkable instrument for further studying polar lows. Coupled with the TOVS instrument, the SSM/I increases our capabilities for monitoring polar low developments in data-sparse regions.

7. Acknowledgements

Part of the SSM/I processing was performed while C. Claud was a visiting scientist at the Department of Atmospheric Sciences of the University of Washington (UW). We thank especially D. Miller of UW for assistance, K. Dewar of UW for producing most of the figures, and M. Homleid at DNMI for providing TOVS data. At LMD, C. Claud is grateful to Dr Y. Tahani for fruitful discussions and to Dr N. Husson for providing codes for the plotting of geopotential thicknesses and water vapor contents derived from the TOVS. The processing of TOVS data has been done on the computers of CIRCE (Centre Inter Regional de Calcul Electronique, CNRS, France). The work at UW was soupported by National Aeronautical and Space Administration (NASA) grant NAGW 1688.

REFERENCES

Alishouse, J.C., Snyder S.A., Vongsathorn, J., and Ferraro, R.R. 1990. Determination of oceanic total precipitable water from the SSM/I, *IEEE Trans. Geosci Remote Sensing, 28*, 811-816.

Chedin, A. and Scott, N.A. 1985. Initialization of the radiative transfer equation inversion problem from a pattern recognition type approach. Applications to the satellites of the TIROS-N series, *Advances in remote sensing retrievals*, Academic press, A. Deepak Ed., 495-515.

Chedin, A., Scott, N.A., Wahiche, C. and Moulinier, P. 1985. The Improved Initialization Inversion method : a high resolution physical method for temperature retrievals from satellites of the TIROS-N series. *J. Clim. Appl. Meteorol., 24*, 124-143.

Chedin, A. 1988. The 3I retrieval method : recent local and global applications, *Proceedings of the ECMWF seminar on data assimilation and the use of satellite data*, Reading, UK, Sept. 5-9, 1988, vol II, 181-213. Available from ECMWF, Shinfield Park, Reading, UK.

Chedin, A., Scott, N.A., Andersson, E. and Flobert, J.F. 1989. Recent developments and results of the 3I algorithm, *Proceedings of the ECMWF/EUMETSAT workshop on the use of satellite data in operational numerical weather prediction : 1989-1993*, Reading, UK, May 9-12,1989, Vol II, 105-126. Available from ECMWF, Shinfield Park, Reading, UK.

Claud, C., Scott, N.A., Chedin, A. and Gascard, J.C. 1991. Assessment of the accuracy of atmospheric temperature profiles retrieved from TOVS observations by the 3I method in the European Arctic ; application for mesoscale weather analysis. *J. Geophys. Res., 96*, (D2), 2875-2887.

European Meteorological Bulletin (1988). Available from Deutscher Wetterdienst, Zentralamt, Frankfurter Straße 135, Postfach 10 04 65, 6050 Offenbach a.M., Germany.

Gloersen, P., Mollo-Christensen, E. and Hubanks, P. 1989. Observation of Arctic polar lows with the NIMBUS-7 Scanning Multichannel Microwave Radiometer, in *Polar and Arctic Lows*, (ed. P.F. Twitchell, E.A. Rasmussen, and K.L. Davidson). Hampton/Virginia : Deepak Publishing, 359-371.

Goodberlet, M.A., Swift, C.T. and Wilkerson, J.C. 1989. Remote sensing of ocean surface winds with the Special Sensor Microwave/ Imager, *J. Geophys. Res., 94* (C10), 14547-14555.

Hollinger, J., Lo, R., Poe, G., Savage, R. and Pierce, J. 1987. Special Sensor Microwave/ Imager User's Guide. Naval Research Laboratory, Washington, D.C., 177p.

Illari, L. 1989. The quality of satellite precipitable water content data and their impact on analyzed moisture fields, *Tellus, 41A*, 319-337.

Katsaros, K.B., Bhatti, I.A., McMurdie, L.A and Petty, G.W. 1989. Identification of atmospheric fronts over the ocean with microwave measurements of water vapor and rain. *Weather and Forecasting, 4* , 449-460.

Le Marshall, J.F. 1988. An intercomparison of temperature and moisture fields derived from the TIROS Operational Vertical Sounder data by different retrieval techniques. Part I : Basic statistics, *J. Appl. Met., 27*. 1282-1293.

McMurdie, L.A. and Katsaros, K.B. 1985. Atmospheric distribution in a midlatitude cyclone observed by the Seasat Multichannel Microwave Radiometer, *Mon. Wea. Rev.*, 113, 584-598.

Petty, G.W. 1990. On the response of the Special Sensor Microwave/Imager to the marine environment. Implications for atmospheric parameters retrievals. Ph D dissertation, University of Washington, 291 pp. Available from University Microfilms, 300 North Zeeb Road, Ann Arbor, Michigan 48106.

Smith, W.L., Woolf, H.M., Hayden, C.M., Wark, D.Q. and McMillin, L.M., 1979. The TIROS-N Vertical Sounder, *Bull. Am. Meteorol. Soc., 60* , 1177-1187.

Tahani, Y., Chedin, A. and Scott, N.A. 1989. Water vapor retrieval from NOAA satellites: application to tropospheric wet correction on tropical areas. *Proceedings of the 4th Conference on Satellite Meteorology and Oceanography*, May 16-19, 1989, San Diego, 147-150. American Meteorological Society, 45 Beacon Street, Boston, Ma., USA.

Tahani, Y. 1991. Restitution de la vapeur d'eau atmosphérique à partir des observations de satellites météorologiques. Interêt pour l'altimétrie spatiale. Ph D dissertation (in french), Université Pierre et Marie Curie, 132 pp. Available from Laboratoire de Météorologie Dynamique, Ecole Polytechnique, 91128 Palaiseau Cedex, France.

Waters, J.W. 1976. Absorption and emission of microwave radiation by atmospheric gases, in *Methods of Experimental Physics*, M.L. Meeks Ed., 12, Part B, Radio Astronomy, Academic Press, Section 2.3.

Zhang, Z., Pailleux, J. and Kelly, G. 1989. Evaluation of developments of the ECMWF humidity analysis. ECMWF Tecnical Memorandum, 160, 31 pp. Available from ECMWF, Shinfield Park. Reading, UK.

Figure captions

Table 1 : Characteristics of TOVS sounding channels.

Table 2 : Characteristics of SSM/I swaths (date, orbit number and time UTC) and corresponding significant meteorological features.

Fig. 1 : Weighting functions of the 6.3 μm ("water vapor") and 11 μm ("windows") HIRS-2 channels (from Smith et al., 1979).

Fig. 2 : Illustration of the positions of SSM/I channels relative to oxygen and water vapor lines in the microwave spectrum (0 - 240 GHz), after Waters, 1976. The zenith opacity refers to the integrated column of the 1962 US Standard Atmosphere.

Fig. 3 : Surface chart (redrawn from the European Meteorological Bulletin) at 1200 UTC

a. 28 February 1988

b. 29 February 1988

c. 1 March 1988

Fig. 4 : AVHRR image, channel 4, 29 February 1988, 0856 UTC (Courtesy of the Royal Dutch Meteorological Institute , [KNMI]).

Fig. 5 : 3I cloud detection results, 29 February 1988, 0856 UTC. Clear areas are displayed by dark dots, cloudy ones are shaded grey. Blank zones correspond to calibration zones.

Fig. 6 : 1000-500 hPa 3I geopotential thicknesses (in decameter) :

a. 29 February 1988, 0856 UTC

b. 29 February 1988, 1707 UTC

c. 1 March 1988, 0833 UTC

Areas of rejections (section 4.2) are shaded grey. The dashed line represents the swath edge.

Fig. 7 : 1000-850 hPa 3I geopotential thicknesses (in decameter), 29 February 1988, 0856 UTC. Areas of rejections are shaded grey.

Fig. 8 : Same as Fig. 7, but 500-300 hPa.

Fig. 9 : 3I total precipitable water (in kg/m^2)

a. 29 February 1988, 0856 UTC

b. 1 March 1988, 0833 UTC

Areas of rejections are shaded grey.

Fig. 10 : same as 9 but for the layer 1000-850 hPa ; values are muliplied by 10

Fig. 11 : same as 10 but for the layer 850-500 hPa

Fig. 12 : Composite SSM/I imagery of the cold air outbreak. Integrated water vapor derived from Eqn. 1. Values range from 1 to 15 kg/m^2. The dashed line represents approximately the sea ice edge.

a. 29 February 1988, easternmost swath is from 1624 UTC, westernmost is from 2124 UTC.

b. 1 March 1988, easternmost swath is from 0041 UTC, westernmost is from 0542 UTC.

c. 1 March 1988, easternmost swath is from 1608 UTC, westernmost is from 2111 UTC.

Fig. 13 : same as Fig. 12, but for surface wind speeds, derived from Eq..2 and only for evening overpasses of 29 February (a) and 1 March (b). Values range from 0 to 20 m/s. The absence of determination (grey areas over sea) indicates the presence of precipitation. The dashed line represents the approximate sea ice edge.

Fig.14 : Cloud liquid water (a) and scattering index by large ice particles (b) for SSM/I pass 3602, 1 March 1988, 0401 UTC. A polar low is identifiable between 72 and 75 N at about 17 E. Note that the intense convective clouds close to the Norwegian Sea are well delineated by the scattering index.

Table 1 : Characteristics of TOVS sounding channels.

HIRS channel number	Central wavelength μm	Principal absorbing constituents	Level of peak energy contribution (hPa)
1	15.00	CO_2	30
2	14.70	CO_2	60
3	14.50	CO_2	100
4	14.20	CO_2	400
5	14.00	CO_2	600
6	13.70	CO_2/H_2O	800
7	13.40	CO_2/H_2O	900
8	11.10	Window	Surface
9	9.70	Oz	25
10	8.30	H_2O	900
11	7.30	H_2O	700
12	6.70	H_2O	500
13	4.57	N_2O	1000
14	4.52	N_2O	950
15	4.46	CO_2/N_2O	700
16	4.40	CO_2/N_2O	400
17	4.24	CO_2	5
18	4.00	Window	Surface
19	3.70	Window	Surface
20	0.70	Window	Cloud

MSU	Frequency (GHz)	Principal absorbing constituents	Level of peak energy contribution
1	50.31	Window	Surface
2	53.73	O_2	700
3	54.96	O_2	300
4	57.95	O_2	90

Table 2 : List of SSM/I swaths (date, orbit number and time UTC) and corresponding significant meteorological features

date	orbit	time	characteristics
28 February	3581	1633	
(evening)	3582	1815	early stage of the cold air outbreak
	3583	1955	
	3584	2135	
29 February	3587	0233	
(early	3588	0413	cold air outbreak well established
morning)	3589	0555	
29 February	3595	1624	
(evening)	3596	1805	strongest temperature and moisture gradients
	3597	1947	
	3598	2124	
1 March	3600	0041	
(early	3601	0221	weakening phase of the outbreak
morning)	3602	0401	polar low detection by SSM/I scattering index
	3603	0542	
1 March	3609	1608	
(evening)	3610	1750	polar low signature gone
	3611	1931	end of the cold air outbreak
	3612	2111	

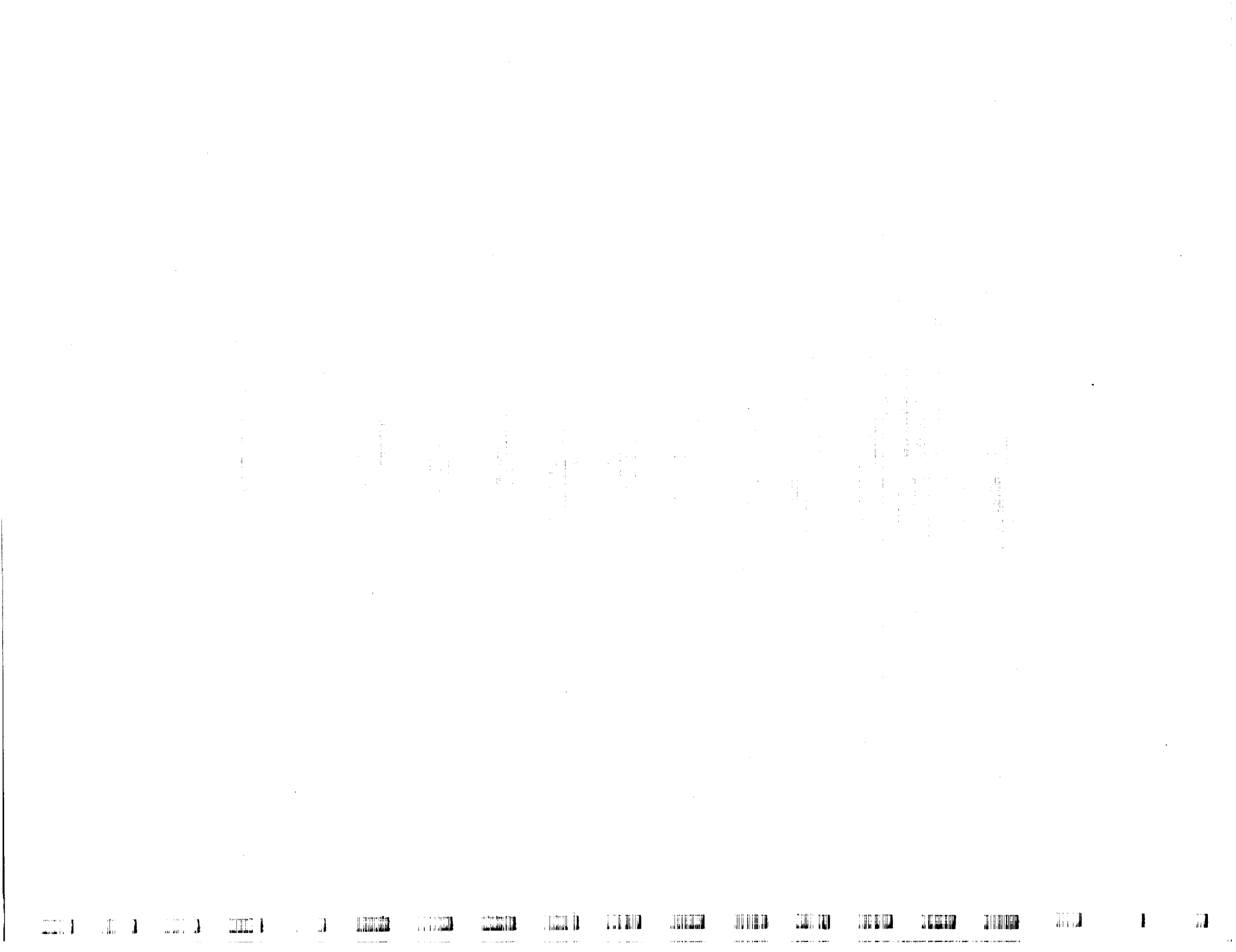

Reprinted from MONTHLY WEATHER REVIEW, Vol. 119, No. 3, March 1991
American Meteorological Society

Satellite-Derived Integrated Water-Vapor Distribution in Oceanic Midlatitude Storms: Variation with Region and Season

LYNN A. MCMURDIE AND KRISTINA B. KATSAROS

Department of Atmospheric Sciences, University of Washington, Seattle, Washington

(Manuscript received 12 March 1990, in final form 15 August 1990)

ABSTRACT

With the atmospheric water-vapor content information available from the SEASAT and Nimbus-7 Scanning Multichannel Microwave Radiometers (SMMR), differences in water-vapor distribution between cyclonic storms in different regions of the global ocean can be examined in more detail than previously possible from radiosondes. SMMR-derived integrated water vapor is a robust and dependable variable of the same accuracy as integrated radiosonde soundings. In this study, maximum and minimum water-vapor content in the vicinity of cold fronts of 80 storms that occurred in the North Atlantic, North Pacific and Southern oceans are compared. North Atlantic storms were found to have significantly higher maximum and minimum water-vapor content near cold fronts on average than North Pacific or Southern ocean storms for both the warm and cold seasons. These differences are attributed to warmer sea surface temperatures and air temperatures in the North Atlantic, and higher baroclinity and consequently stronger upward motion in North Atlantic storms. Additionally, some of the differences may be attributed to the fact that the North Atlantic storms generally occur at lower latitudes than the storms in the other regions. Furthermore, the North Pacific storms were found to have significantly higher maximum and minimum water-vapor content near cold fronts on average than the Southern Ocean storms for both the warm and cold seasons. These differences are attributable to warmer sea surface temperatures in the North Pacific during the warm season, and to less moisture transport by Southern Ocean storms and the poleward location of the Southern Ocean storms compared to North Pacific storms during the cold season. Two examples of water-vapor content in a South Atlantic storm are given to contrast with the Southern Ocean cases. The South Atlantic storm had much higher maximum water-vapor content near the cold front than most Southern Ocean storms.

1. Introduction

The initiation and development of midlatitude cyclones often occur over oceanic regions. Unfortunately, the available in situ information regarding the state of the atmosphere in vicinity of these storms is sparse, and in large regions in the Southern Hemisphere it is almost nonexistent. Since the advent of satellite remote sensing, this concern has been alleviated. Satellite-derived fields, such as temperature soundings, have been used as input to global numerical weather prediction models and have been found to improve forecasts significantly over data sparse regions, especially in the Southern Hemisphere (Bourke et al. 1982; Kalnay et al. 1985). Visible and infrared satellite pictures are routinely used by forecasters and scientists to track storm movement and to observe their development and decay (Anderson et al. 1969; Weldon 1977; Smigielsky and Elrod 1985), especially over ocean regions. Recently, instruments sensitive to the microwave portion of the electromagnetic spectrum have been placed on polar orbiting satellites. Microwave remote sensing techniques offer improvements over previous visible and infrared techniques by allowing quantitative measurements of surface and atmospheric variables even in the presence of clouds. Atmospheric variables, such as boundary layer winds and integrated water vapor, have been successfully obtained from satellite-borne microwave instruments and proven useful in the research of midlatitude cyclones (McMurdie and Katsaros 1985; Katsaros and Lewis 1986; and McMurdie et al. 1987; Levy and Brown 1986; Brown and Levy 1986; Levy 1989).

Atmospheric water vapor plays an important role in midlatitude cyclones. The formation of precipitation depends on the supply of water vapor; it is an important consideration in determining the structure of atmospheric boundary layers around frontal zones (Fleagle et al. 1988), and it can influence the development of midlatitude cyclones through the release of latent heat (Danard 1964; Reed et al. 1988). Detailed structure

Corresponding author address: Dr. L. McMurdie, Dept. of Atmospheric Sciences AK-40, University of Washington, Seattle, WA 98195.

and magnitude of the atmospheric water-vapor distribution in midlatitude cyclones were unavailable before microwave remote sensing techniques were developed. In this paper, the water-vapor information derived from the SEASAT and Nimbus-7 Scanning Multichannel Microwave Radiometers (SMMR) is examined to study the nature of the atmospheric water-vapor availability in midlatitude cyclones. The goal of this paper is to document typical water-vapor distributions in midlatitude cyclones in specific oceanic regions around the globe. Differences in water-vapor distribution in storms occurring in various regions are highlighted.

In the following sections, background concerning the satellites and the instruments used and the methods of the analysis are discussed. The results are highlighted with examples of atmospheric water-vapor distribution in midlatitude cyclones occurring in the North Atlantic, North Pacific, Southern Ocean, and South Atlantic. A summary of all the cases examined in these regions is discussed in the last section.

2. Background

The SEASAT satellite, launched in June 1978, was a unique research satellite devoted entirely to the remote sensing of the world's oceans. It carried several microwave instruments, and demonstrated that the state of the ocean environment can be monitored from space (Born et al. 1979). Data collected during this mission are still being utilized today, despite the premature end of SEASAT only three months after launch. Soon after the failure of SEASAT, the Nimbus-7 satellite was launched in October 1978. The eight instruments aboard the Nimbus-7 have provided data continuously for over eight years. It has allowed an exceptional opportunity to remotely monitor the state of the earth–atmosphere system over a long time period.

Both the SEASAT and the Nimbus-7 satellites carried a SMMR instrument. It measures the thermal emission of the earth–atmosphere system at five microwave frequencies (6.6, 10.7, 18.0, 21.0, and 37.0 GHz) and in both horizontal and vertical polarization on a spatial resolution of 50 km × 50 km for the 18.0- and 21.0-GHz channels and 27 km × 27 km for the 37.0-GHz channel. From this information, quantitative measurements of sea surface temperature, surface wind speed, sea ice concentration, integrated water vapor, integrated liquid water, and rainrate can be obtained. Of these parameters, the atmospheric water-vapor measurements have proven most reliable and as accurate as radiosonde derived estimates of integrated water vapor for a wide range of atmospheric conditions (Katsaros et al. 1981; Alishouse 1983; Chang et al. 1984).

SMMR-derived integrated water-vapor information has been useful for a variety of research objectives. Chang et al. (1984) and Prabhakara et al. (1982) examined the monthly, seasonal, and interannual variability of precipitable water over the global oceans. They identified several prominent features indicative of the large-scale atmospheric circulation, including dry regions associated with subtropical anticyclones and a region of very high atmospheric water-vapor over the western Pacific associated with the Walker circulation. Prabhakara et al. (1985) compared the water-vapor distribution determined from SMMR during normal years to the anomalous El Niño year of 1982/83 and found that the water-vapor distribution gave a very clear picture of the changes in the atmospheric circulation patterns during an El Niño year. Francis (1987) also demonstrated the evolution of the monthly variation in the global distribution of water vapor for a 5-yr period using recalibrated brightness temperatures of Nimbus-7 SMMR. The integrated water-vapor distribution from SMMR has also been used to examine individual midlatitude cyclones over the oceans. The fields can be used to accurately locate the position of surface frontal zones and frontal waves (McMurdie and Katsaros 1985; Katsaros et al. 1989). When the SMMR water-vapor field is used in conjunction with scatterometer derived boundary-layer winds, qualitative inference of the relative distribution of water vapor with height can be made (McMurdie et al. 1987).

3. Data analysis

The SEASAT data were obtained from the NASA Jet Propulsion Laboratory (JPL) in the form of geophysical parameters including integrated water vapor. The water-vapor parameter was calculated by JPL from the brightness temperatures of the 18-, 21-, and 37-GHz channels using the Wilheit and Chang (1980) algorithm. Some minor corrections to the coefficients were made after the data were compared to radiosonde soundings (SEASAT, 1981). The Nimbus-7 data were obtained from Goddard Space Flight Center in the form of brightness temperatures. Corrections outlined by Kim et al. (1984) were applied to the data to account for instrument warm up time, cross-swath biases, and drift in the 21-GHz horizontal channel. The corrected brightness temperatures were then processed through the Chang et al. (1984) water-vapor algorithm.

With the SEASAT SMMR and Nimbus-7 SMMR data, over 80 individual cyclones spanning the period September 1978 (SEASAT) and 1979–1982 (Nimbus-7) are examined. Since the Nimbus-7 SMMR operated on an alternate day duty cycle, and after 1982 the data quality deteriorated (see Francis 1987), the number of cases available for this study is limited. Individual satellite passes that occurred during the same season, and in the same oceanic region are grouped together into one category. Surface and upper-level analyses from the National Meteorological Center (NMC) and the Australian Bureau of Meteorology (ABM) and any available visible or infrared satellite images are used to locate surface fronts. Since the NMC and the ABM

surface analyses are used primarily in an operational setting, the frontal locations are sometimes inaccurate. There are occasions when there are minor discrepancies between the SMMR water-vapor patterns and the NMC or ABM front locations. When there are disagreements, they will be mentioned in the subsequent analysis. Only satellite passes over cold fronts near the surface low of mature cyclones are included. Mature cyclones are defined here as storms where the surface fronts have occluded and the satellite pictures show a distinctive large-scale comma shape. Passes over decaying storms and cold fronts far away from the main low pressure center are not included. In addition, cases with severe rain interference problems were excluded. Rain interference was inferred based on the 37-GHz polarization differences and on the water-vapor patterns themselves. If there was rain interference, it would be manifested as low polarization differences in the 37-GHz channels and as sporatic anomalously low water-vapor amounts within a field of high water-vapor content. Very few passes exhibited rain interference, although rain was present in many cases. A total of seven passes were excluded from the study.

The data were grouped according to season, where "warm" season includes storms occurring in September–November in the Northern Hemisphere and January–March in the Southern Hemisphere, and the "cold" season included storms during December–March in the Northern Hemisphere and July–September in the Southern Hemisphere. During the midsummer period, June–August, the storm frequency in the North Pacific and North Atlantic is low. We attempted to include some storms in this period, but found few cases available where the SMMR sampled a storm. Because of this, the warm season is slightly different in the Southern Hemisphere and the Northern Hemisphere with respect to the solstice. However, it is likely that these results would not be altered substantially if we were able to include cases symmetric about the solstices. This issue is discussed further in section 5.

Three oceanic regions are studied in detail: the North Atlantic, the North Pacific, and the Southern Ocean. A few passes from the South Atlantic were also studied, but this region is near where the Nimbus-7 SMMR was turned on and off and the usable samples were fewer. The exact sampling regions are shown in the subsequent sections. In Table 1, the time periods used in this study and the number of passes included during each period for each area and season are given. A total of 180 satellite passes are used in the analysis, an average of more than two passes per storm. Frontal analyses shown in all the figures are taken from either NMC or ABM unless otherwise noted.

For each case, a representative maximum and minimum integrated water-vapor content is picked and cases in the same category are averaged together. The method for selecting the maximum and minimum water-vapor values is as follows. The maximum value is either the highest contour in the vicinity of a front (i.e., within 200 km of the front) or 2 kg m^{-2} higher than the highest contour if there is a substantial region with values higher than the highest contour. The latitude at which the maximum value was obtained was as near as possible, depending on the sampling by the satellite, to the surface low or the triple point, where the occluded, warm and cold fronts coincide. The minimum value is the value of the lowest contour within 500 km of the cold front, towards the cold air, or 2 kg m^{-2} lower than the lowest contour depending on which is more appropriate.

In addition, statistical tests were made to see if the average or mean of one category was significantly different than the mean of another category using the two sample *t*-test. A minimum confidence level of 95% was chosen as the requirement for a difference between two categories to be considered significant. However, in most of the subsequent analysis, the difference between two categories was often significant at the 99% confidence level.

Every effort was made to insure that the sampling was as random as possible. Every time the satellites went over any cold frontal zone and there was no severe rain interference or the storm was not decaying, the case was included in the statistics. Again, the sampling limitations of the Nimbus-7 satellite limited the number of cases available for each category. Since several years worth of data were included, the sample size was sufficient for meeting the significance criteria.

4. Results

a. North Atlantic

Storms that developed in the region east of the east coast of the United States from 25° to 55°N and 80° to 20°W were considered to be North Atlantic storms. A map of this region is given in Fig. 1. In addition, the locations of the warm and cold season storms are indicated on this map. The western Atlantic Ocean along the east coast of the United States is a preferred region for the development of rapidly deepening cyclones (i.e., storms that during their deepening stage had pressure falls greater than 1 mb h^{-1} for 24 hours; Sanders and Gyakum 1980). Since it is of interest to explore the possible differences in SMMR-derived water-vapor in these storms compared to regularly developing storms, the storms are separated into the categories "rapidly deepening" and "standard".

A typical example of the water-vapor distribution for a warm season North Atlantic mature cyclone is given in Fig. 2. The region of maximum water vapor is in the vicinity of the cold front and the amounts are quite high. There is a strong gradient behind the cold front to the northwest of the area of maximum water vapor, and the minimum water-vapor values are 15–16 kg m^{-2}. There is an increase of water vapor to 22 kg m^{-2} in the vicinity of the low center. South of the

TABLE 1. Dates and number of satellite passes over cold fronts occurring in different regions used in the study.*

North Atlantic		North Pacific		Southern Ocean	
Dates	Number	Dates	Number	Dates	Number
September 1978	6	September 1978	8	January–March 1979	27
November 1980	12	November 1980	10		
September 1981	4	September 1979	5		
November 1981	1	September 1981	3		
Totals	23		26		27
January–March 1979	20	January–March 1979	18	September 1978	9
January–March 1981	19	January 1981	6	July 1979	18
January 1982	3	January, March 1982	4	September 1979	3
Totals	42		28		30
Grand total	176				

* Passes that sampled the warm sector, cold fronts, and the cold sector are all included in this table. This differs from Figs. 1, 4, and 7 which include the locations of passes sampling cold fronts only.

cold front, the water-vapor pattern exhibits bands of dry and moist air. The band of moist air at 35°N, 40°W is associated with an old, stationary front. The explanation for the band of high moisture content between the cold front and the stationary front is not known at this time.

A typical example of the moisture distribution in a cold season mature cyclone in the North Atlantic is given in Fig. 3. There is a maximum in water-vapor content along the cold front of 32 kg m^{-2} and high values of 26 kg m^{-2} along the warm front. There is also a local maximum along the occluded front of 20 kg m^{-2}. The region of minimum water vapor in the cold sector was not sampled.

A summary of the average maximum and minimum water-vapor content of rapidly deepening and standard storms are presented in Table 2. The two-sample *t*-test was used to test for significant differences in the maximum and minimum water-vapor contents between rapid and standard storms of the same season. These tests demonstrated that there is no significant differences in maximum water-vapor content in the vicinity of mature cold fronts in rapidly deepening cyclones and standard cyclones. The difference between the average minimum water-vapor content between rapid and standard storms during the warm season is significant at the 95% confidence level, but the difference is not significant during the cold season. However, the average maximum and minimum water-vapor contents in the warm season storms (total storms category) are significantly higher than in cold season storms. This is largely a consequence of the difference in the mean air temperatures between the seasons.

Additional passes over cold fronts of developing systems and over warm and occluded fronts of developing and mature systems were examined by McMurdie (1989). In that study, the average maximum water-vapor content near cold fronts was significantly larger than the average maximum water-vapor content near warm fronts, which in turn was larger than the average maximum near occluded fronts. This result can be explained by the fact that the occluded fronts lie farther north than warm fronts and warm fronts lie farther north than cold fronts during the mature stage of a cyclone.

b. North Pacific

The North Pacific category included storms in the region from 25° to 60°N and from 120° to 180°W. A map of this region is given in Fig. 4 along with the locations of the different storms sampled. Examples of storms that developed west of 180°W are discussed by McMurdie (1989) but are not included here.

A typical example of water-vapor distribution in a warm season North Pacific mature cyclone is given in Fig. 5. In this case, on 1000 UTC 14 September 1981, the maximum water vapor lies along the cold front and is greater than 40 kg m^{-2}. Near the warm front in the warm sector, the values are also high, greater than 32 kg m^{-2}. At 50°N, there is a distinct curvature to the contours near the front that parallels a wave along the front analyzed by NMC. The driest air sampled in this pass lies well west of the cold front at 45°N, where the integrated water-vapor content is 16 kg m^{-2}. In Fig. 5, three x's indicate where there is suspected rain interference. Despite these small regions of heavy rain, the overall water-vapor pattern is retained.

In contrast, Fig. 6 is a typical example of water-vapor distribution during the cold season in the North Pacific. Here, again, the maximum water-vapor content lies along the cold front; however, the amount is only 28 kg m^{-2}. The region of minimum water vapor is in a broad region immediately behind and northwest of the cold front and the amounts are 6–8 kg m^{-2}. Both of these regions have significantly lower water-vapor content than similar localities in the warm season case, as expected. During the warm season the air temperatures

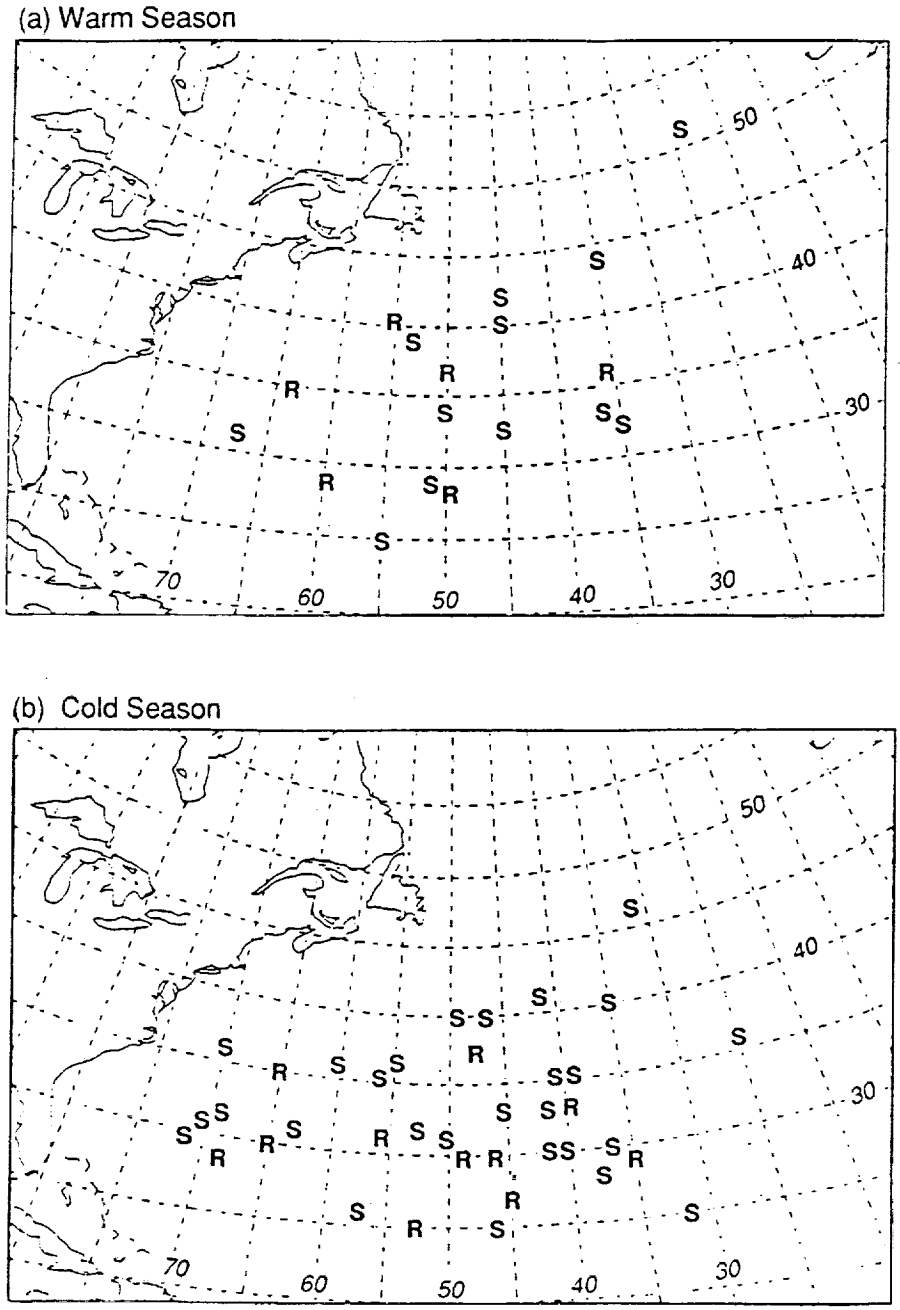

FIG. 1. Map of the North Atlantic region. Storms existing between 80° to 20°W and 25° to 60°N were included in this study. (a) Locations where the satellite sampled the cold fronts of rapidly deepening cyclones (R) and standard cyclones (S) during the warm season. (b) Locations where the satellite sampled the cold fronts of rapidly deepening cyclones (R) and standard cyclones (S) during the cold season.

are significantly warmer enabling the atmosphere to hold more water vapor, which is clear in these figures.

The average maximum integrated water-vapor content of 28 passes over mature cold fronts during the warm season in the North Pacific was 34.9 kg m^{-2} and the standard deviation was 6.0 kg m^{-2}. The average minimum was 13.0 kg m^{-2} and the standard deviation was 3.2 kg m^{-2}. The average maximum of 28 passes over cold fronts during the cold season was 25.6 kg m^{-2} and the standard deviation was 5.6 kg m^{-2}. The average minimum was 9.8 kg m^{-2} and the standard deviation was 3.5 kg m^{-2}. Using the two-sample *t*-test,

Q-2

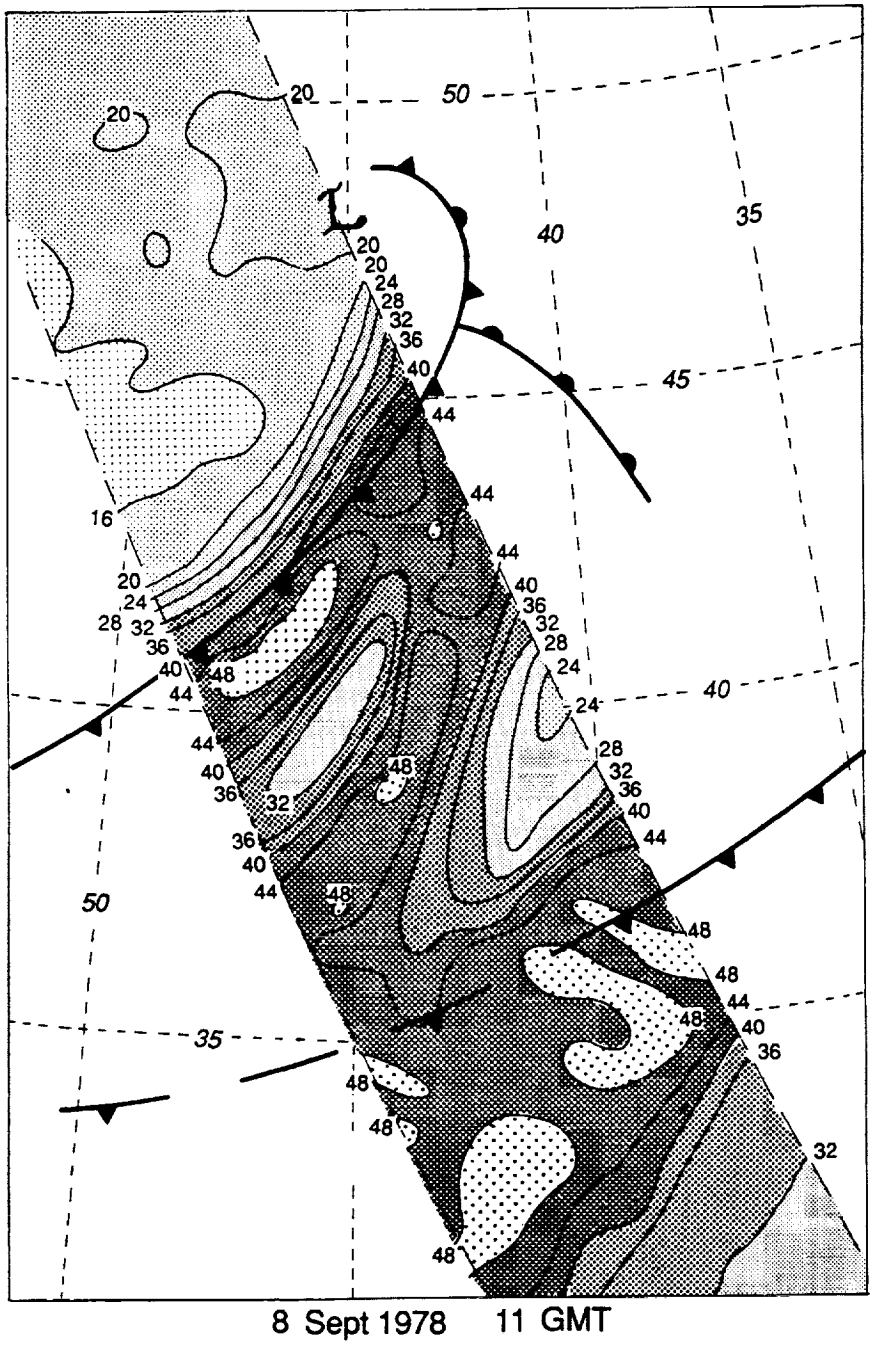

FIG. 2. An example of SMMR integrated water-vapor distribution for 1200 UTC 8 September 1978 in the warm season for the North Atlantic. Contours are every 4 kg m^{-2}. Frontal positions are obtained from NMC operational surface analysis.

the average maximum and minimum water-vapor content in the vicinity of cold fronts of mature systems is significantly higher during the warm season than during the cold season. As with the North Atlantic cases, this is largely due to the colder air and sea surface temperatures during the cold season.

Additional passes over developing systems and over warm and occluded fronts were examined by McMurdie (1989). In that study, cold fronts were found to have significantly higher maximum water-vapor content than warm fronts, and warm fronts were found to have significantly higher maximum water-vapor content than occluded fronts in both seasons. However, no significant difference was found between average

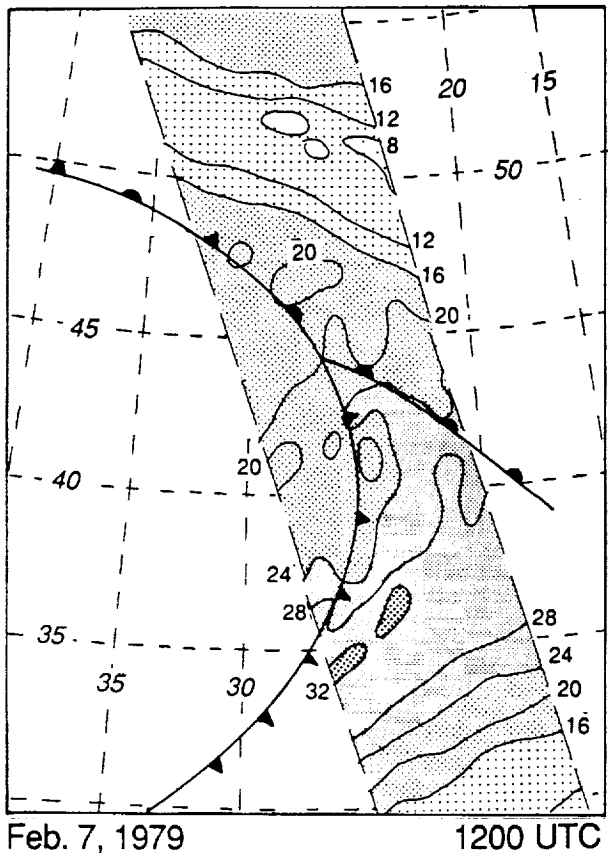

FIG. 3. An example of SMMR integrated water-vapor distribution for 1200 UTC 7 February 1979 in the cold season for the North Atlantic. Contours are every 4 kg m^{-2}. Frontal positions are obtained from NMC operational surface analysis.

maximum water-vapor content near cold fronts of developing cyclones and cold fronts of mature cyclones. Interestingly, average maximum water-vapor content near warm fronts of developing systems was significantly higher than average maximum water-vapor content in warm fronts of mature systems. In this region, it is likely that the typical warm front of mature systems lies significantly poleward of the typical warm front of developing systems, whereas the average latitude of the sampled cold fronts was similar for developing and mature systems.

c. *Southern Ocean*

Storms that occurred in the region 90°–160°E and 30°–60°S were considered to be Southern Ocean storms. This area includes the ocean west and south of Australia, as seen in the map given in Fig. 7. The locations of the sampled storms in this study are also indicated on the map. The operational analyses of the ABM were used to determine the location of the fronts.

A typical example of a warm season cyclone in the Southern Ocean is given in Fig. 8. This Nimbus-7 overpass occurred at 0521 UTC 14 January 1979 just west of the west coast of Australia. The region of maximum water vapor lies in a relatively narrow band along the cold front with values of 24 kg m^{-2}. At the cold front near 50°S the maximum water-vapor content is less at 16–20 kg m^{-2}. Immediately west of the cold front the water vapor decreases rapidly to a minimum of 11–12 kg m^{-2}. Near the low pressure center, the water-vapor content increases to 16–17 kg m^{-2}. Poleward of the system at 55°S, the water-vapor content is very low, less than 6 kg m^{-2}. The region south of 55°S is often very cold and dry in all seasons.

A typical example of a cold season Southern Ocean cyclone is given in Fig. 9. Again, the maximum water vapor lies in the vicinity of the cold front, however, the amounts are very low, 20 kg m^{-2}. There is a fairly strong decrease behind the cold front, to the south, to a region of minimum water-vapor content of 4–5 kg m^{-2}. Although the water-vapor pattern is typical of midlatitude storms in many regions, the water-vapor content is exceptionally low.

The average water-vapor content for warm and cold season storms are summarized as follows: of 27 satellite passes over warm season cyclones, the average maximum in the vicinity of cold fronts is 25.3 kg m^{-2} and

TABLE 2. Average maximum and minimum water-vapor content for warm and cold season cold fronts of North Atlantic storms. Average water-vapor content and standard deviation are given in kilograms per square meter (kg m^{-2}), and n is the number of cases.

	Maximum			Minimum		
Case	Average	Standard deviation	n	Average	Standard deviation	n
Warm season						
Standard	41.5	4.5	12	18.1	4.5	13
Rapidly deepening	43.0	4.7	6	14.8	4.4	10
Total	42.0	4.5	18	16.6	4.6	23
Cold season						
Standard	30.6	5.2	27	14.5	4.7	29
Rapidly deepening	33.5	4.7	11	14.1	5.6	10
Total	31.5	5.0	38	14.3	4.9	39

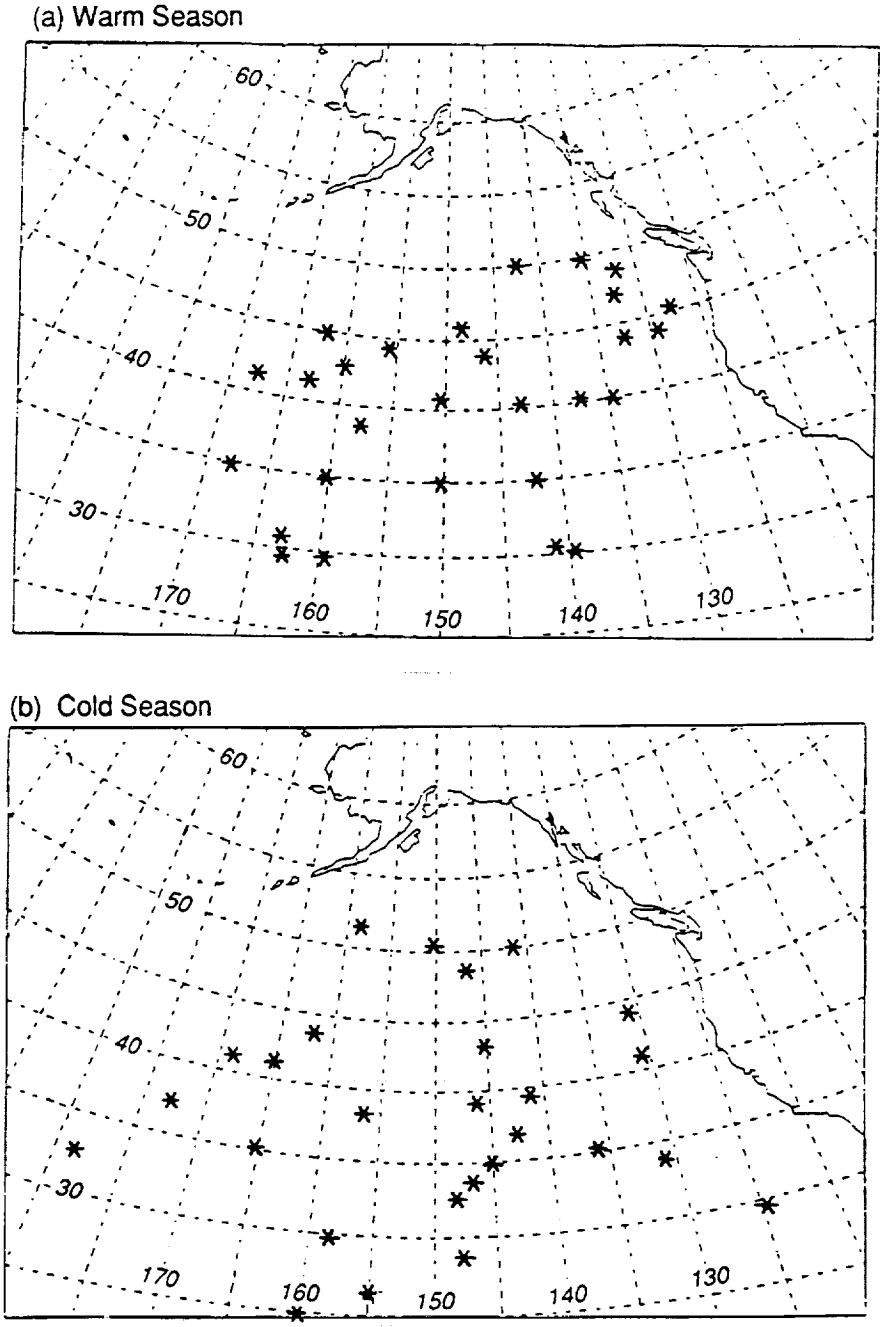

FIG. 4. Map of the North Pacific region. Storms existing between 180° to 120°W and 25° to 60°N were included in this study. Locations where the satellite sampled the cold fronts are indicated by a star (*) during (a) the warm season and (b) the cold season.

the standard deviation is 3.9 kg m^{-2}. The average minimum behind cold fronts is 9.0 kg m^{-2} and the standard deviation is 1.9 kg m^{-2}. Of 30 satellite passes over cold season cyclones, the average maximum in vicinity of cold front is 20.1 kg m^{-2}, the standard deviation is 4.5 kg m^{-2}. The average minimum behind cold fronts is 8.2 and the standard deviation is 2.7. As in the other regions, there is a significant difference in the maximum water-vapor contents between the cold season and warm season storms. However, the difference is not nearly as large as in the North Pacific or in the North Atlantic cases.

d. South Atlantic

The Southern Ocean cases presented in the previous section are not representative of the entire Southern

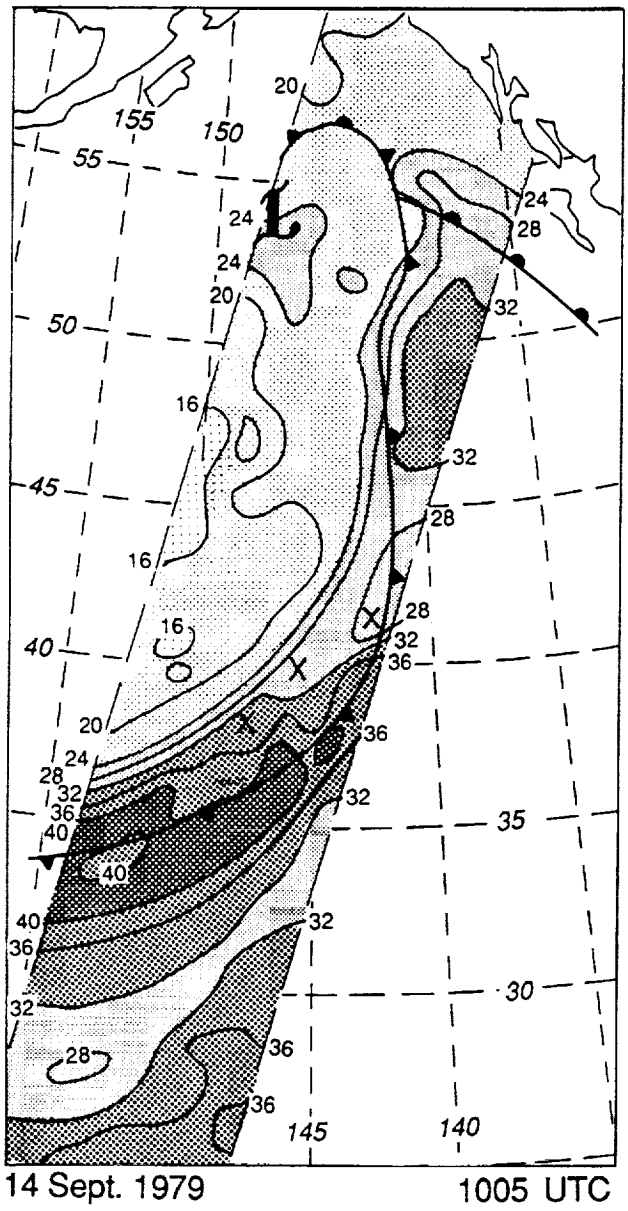

FIG. 5. An example of SMMR integrated water-vapor distribution for 1000 UTC 14 September 1981 in the warm season for the North Pacific. Contours are every 4 kg m^{-2}. Frontal position is obtained from NMC operational surface analysis. The small x's indicate regions of suspected rain interference.

Hemisphere oceanic regions. In this section two examples from a South Atlantic ocean storm are presented to contrast with the Southern Ocean cases. Rigorous tests regarding significant differences between storms in the Southern Ocean and this region have not been performed.

In Figs. 10 and 11, a storm that developed off the east coast of South America is sampled twice by Nimbus-7 SMMR, two days apart. In the earlier pass (Fig. 10), 1400 UTC 28 January 1979, there is a large amount of water vapor in the vicinity of the cold front, approximately 32 kg m^{-2} at 45°S, and the water vapor increases equatorward to greater than 40 kg m^{-2}. There is no distinct maximum along the front. The gradient behind the front, towards the south, is strong, and the minimum water-vapor content in this region is 11 kg m^{-2}. In the later pass (Fig. 11), 1300 UTC 30 January 1979, the vapor content in the vicinity of the cold front is higher, greater than 40 kg m^{-2} at 40°S, and the amount decreases slightly equatorward. There is a very strong gradient poleward to a minimum amount of 7 kg m^{-2}. The front position was taken from the 1200 UTC 30 January 1979 ABM map. It appears that the ABM frontal location is too far into the cold dry air. Our past experience would place the front closer to the region of maximum water-vapor content along the 24 or 28 kg m^{-2} contour line in this figure.

In both of these cases the maximum water-vapor content is much higher than in any of the Southern Ocean storms. On seasonal time scales, the region east

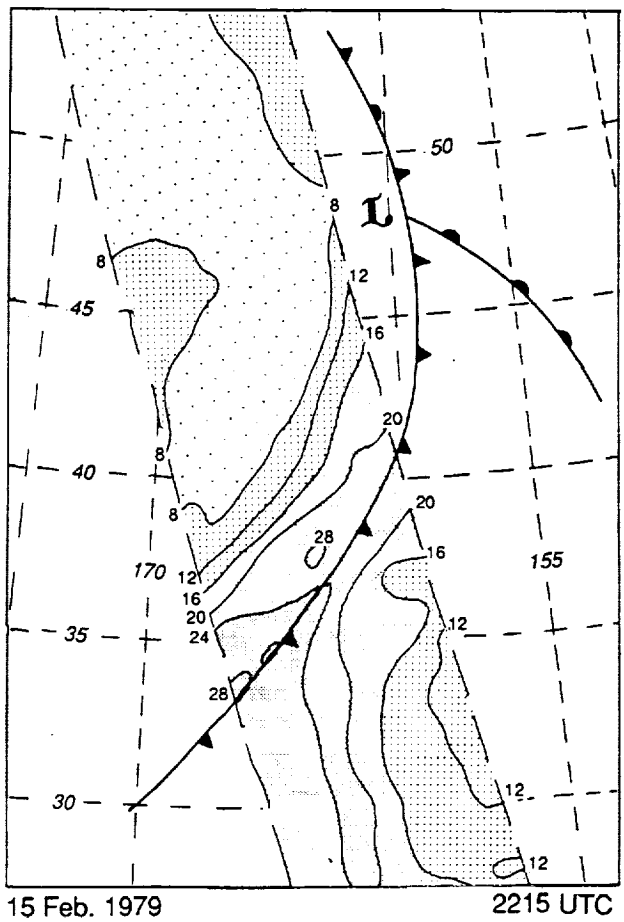

FIG. 6. An example of SMMR integrated water-vapor distribution for 2200 UTC 15 February 1979 in the cold season for the North Pacific. Contours are every 4 kg m^{-2}. Frontal positions are obtained from the NMC operational surface analysis.

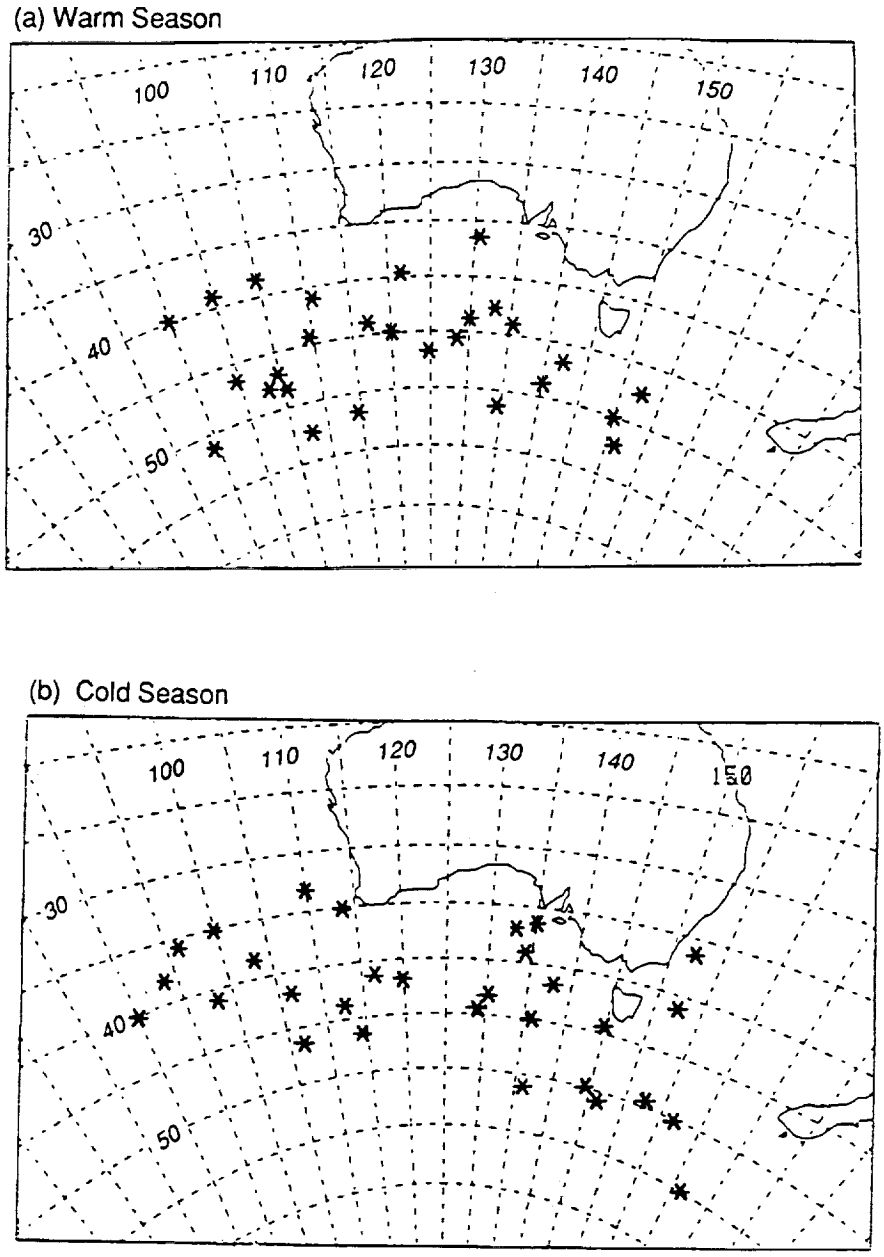

FIG. 7. Map of the Southern Ocean region. Storms existing between 90° to 160°E and 25° to 60°S were included in this study. Locations where the satellite sampled the cold fronts are indicated by a star (*) during (a) the warm season and (b) the cold season.

of South America and equatorward of 40°S has total water-vapor content greater than 30 kg m^{-2} during December–February (see Fig. 12). This is higher than the vapor content at the same latitude in the vicinity of Australia (15–20 kg m^{-2}). In addition, this particular area is a known region of cyclogenesis (Physick 1981; Carleton 1980). Using seasonal mean fields for the period July–August 1982, James and Anderson (1984) found a high incidence of transient eddy activity (baroclinic waves) over the South Atlantic, east of South America. They found that this activity could not be explained by low- and midlevel baroclinicity defined on the basis of dry, linear theory. They suggested that an increase of moisture entrainment into the westerlies in this region could account for the large transient activity there. They explored this possibility using model derived moisture, but lacked sufficient moisture observations to substantiate their results. The SMMR data

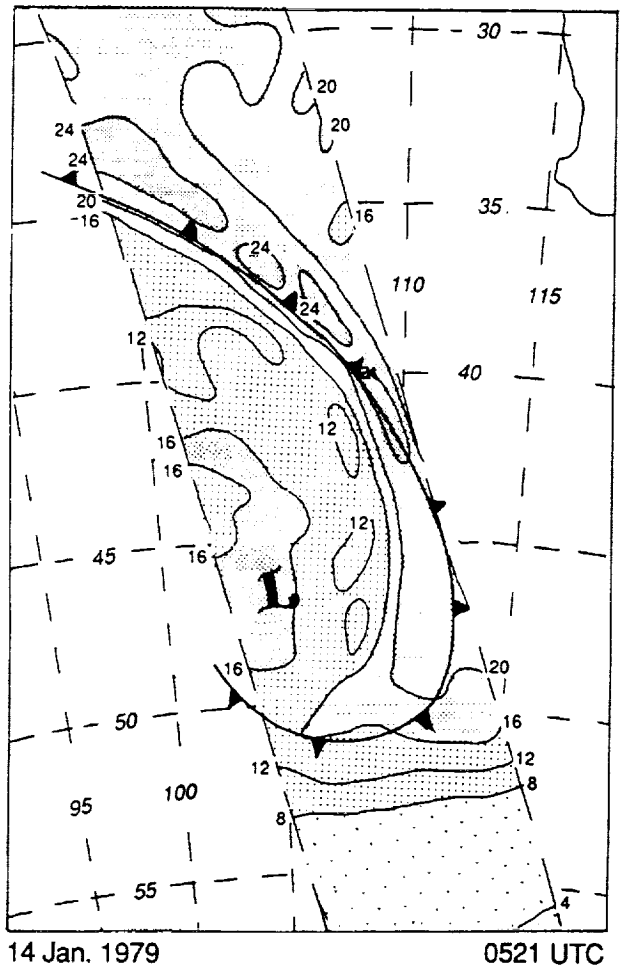

FIG. 8. An example of SMMR integrated water-vapor distribution at 0600 UTC 14 January 1979 in the warm season over the Southern Ocean. Contours are every 4 kg m^{-2}. Frontal position is estimated from the 0000 UTC and 1200 UTC 14 January 1979 ABM operational surface analyses.

support their suggestion and show there is higher amount of moisture in storms observed east of South America compared to Southern Ocean storms.

5. Discussion

In the previous sections, the typical distribution of water vapor in midlatitude cyclones in the North Pacific, North Atlantic, and Southern Ocean were presented and two passes over a storm in the South Atlantic were discussed. In Table 3, the average maximum and minimum water-vapor content in mature cold fronts for these three areas are repeated. Using the two-sample *t*-test, the North Atlantic cold fronts have significantly higher average maximum and minimum water-vapor contents than the North Pacific ones for both seasons; and the North Pacific cold fronts in turn have significantly higher average maximum and minimum water-vapor content than the Southern Ocean cold fronts for both warm and cold seasons.

It is clear from Table 3 that the North Atlantic region has very high moisture content in midlatitude storms. This can partially be explained by the relatively high sea surface temperatures in the North Atlantic and consequently higher evaporation and moisture flux into the atmosphere in this region, especially in the warm season. Consequently, the seasonal mean integrated water-vapor content in the North Atlantic is higher than in the North Pacific and the Southern Ocean for both seasons. During the warm season, it ranges from 35–20 kg m^{-2} in the latitude interval 30°–50°N in the North Atlantic. In contrast, in the North Pacific and Southern Ocean, it ranges from 30–15 kg m^{-2} and 21–15 kg m^{-2}, respectively, in the same latitude band (see Fig. 12). During the cold season, the mean water-vapor

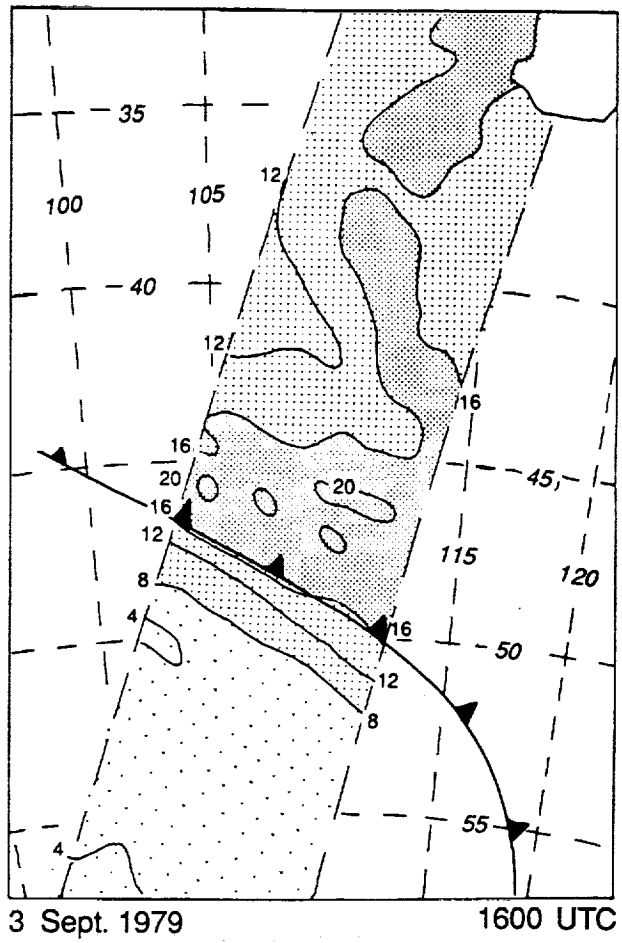

FIG. 9. An example of SMMR integrated water-vapor distribution at 1600 UTC 3 September 1979 in the cold season over the Southern Ocean. Contours are every 4 kg m^{-2}. Frontal position is estimated from the 1200 UTC 3 September 1979 and the 0000 UTC 4 September 1979 ABM operational surface analyses.

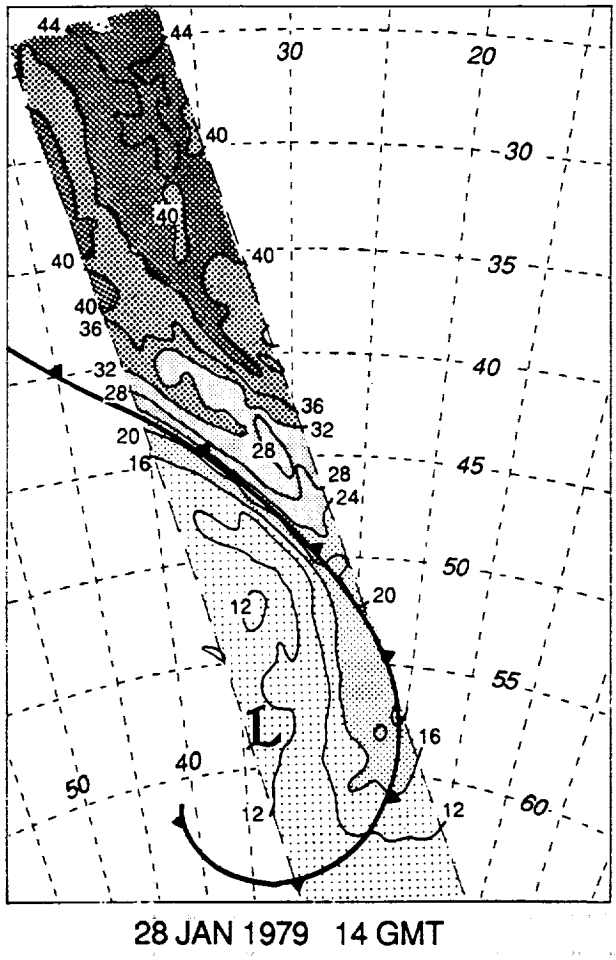

FIG. 10. Integrated water-vapor distribution for a South Atlantic storm that occurred at 1400 UTC 28 January 1979. Contours are every 4 kg m^{-2}. Frontal position is from the 1200 UTC 28 January 1979 ABM frontal analysis.

content in the 30°–50° latitude band ranges from 25–15 kg m^{-2} in the North Atlantic, 22–12 kg m^{-2} in the North Pacific, and 17–10 kg m^{-2} in the Southern Ocean (see Fig. 12). In addition, there is a western boundary current in the North Atlantic in the Gulf Stream, which is a permanent feature just off the east coast of the United States where warm ocean waters travel rapidly northward and eastward from the tropics to the mid-latitudes. The availability of atmospheric moisture from this warm ocean source must contribute to the moisture content in weather systems in the North Atlantic region. Furthermore, the North Atlantic, specifically along the East Coast, is a known region of cyclogenesis; often the storms that form there deepen rapidly. The proximity of the warm Gulf Stream to a source of cold air of continental origin enhances low-level baroclinicity and decrease the static stability in the atmosphere producing a favorable environment for cyclogenesis (Hadlock and Kreitzberg 1988). Since it is such an active region of cyclogenesis and frontogenesis, the synoptic and mesoscale convergence and upward vertical motion in the vicinity of fronts may be stronger than in most storms, thus, creating higher integrated moisture in the frontal zones of these storms. In addition, the North Atlantic storms used in this study occurred at lower latitudes than the North Pacific and Southern Ocean storms. When the latitude of the maximum water-vapor content in the vicinity of the cold front for each pass over a storm is used to indicate the location of each storm, the average latitude of the North Atlantic storms is 33°N. In contrast, the average latitude of the North Pacific and Southern Ocean storms is 38°N and 42°S, respectively. All these factors must contribute to the high moisture content in storms in the North Atlantic.

The integrated moisture content in the region of the minimum behind the cold front was also highest in the North Atlantic for both seasons. Although the air in the region where the water vapor is minimum typically originates from very cold and dry continental

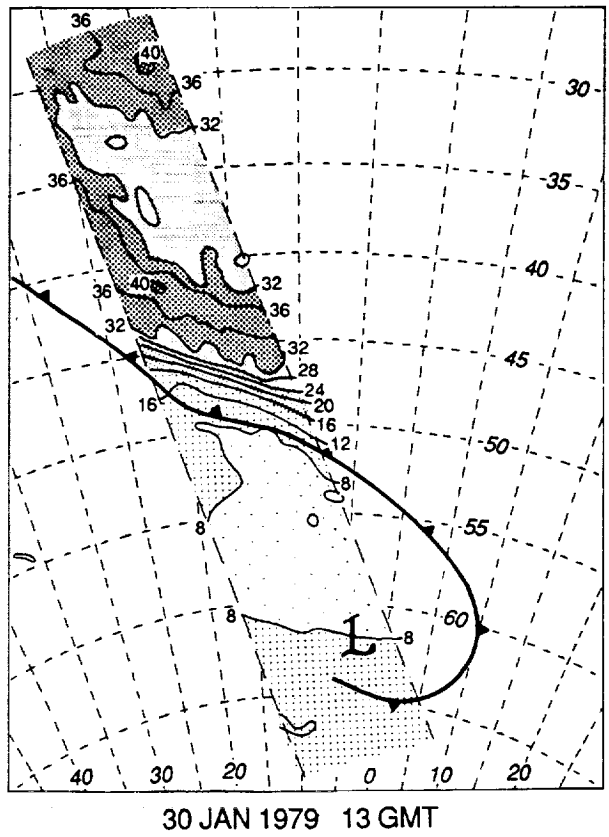

FIG. 11. Integrated water-vapor distribution for a South Atlantic storm that occurred at 1300 UTC 30 January 1979. Contours are every 4 kg m^{-2}. Frontal position is from the 1200 UTC 30 January 1979 ABM frontal analysis.

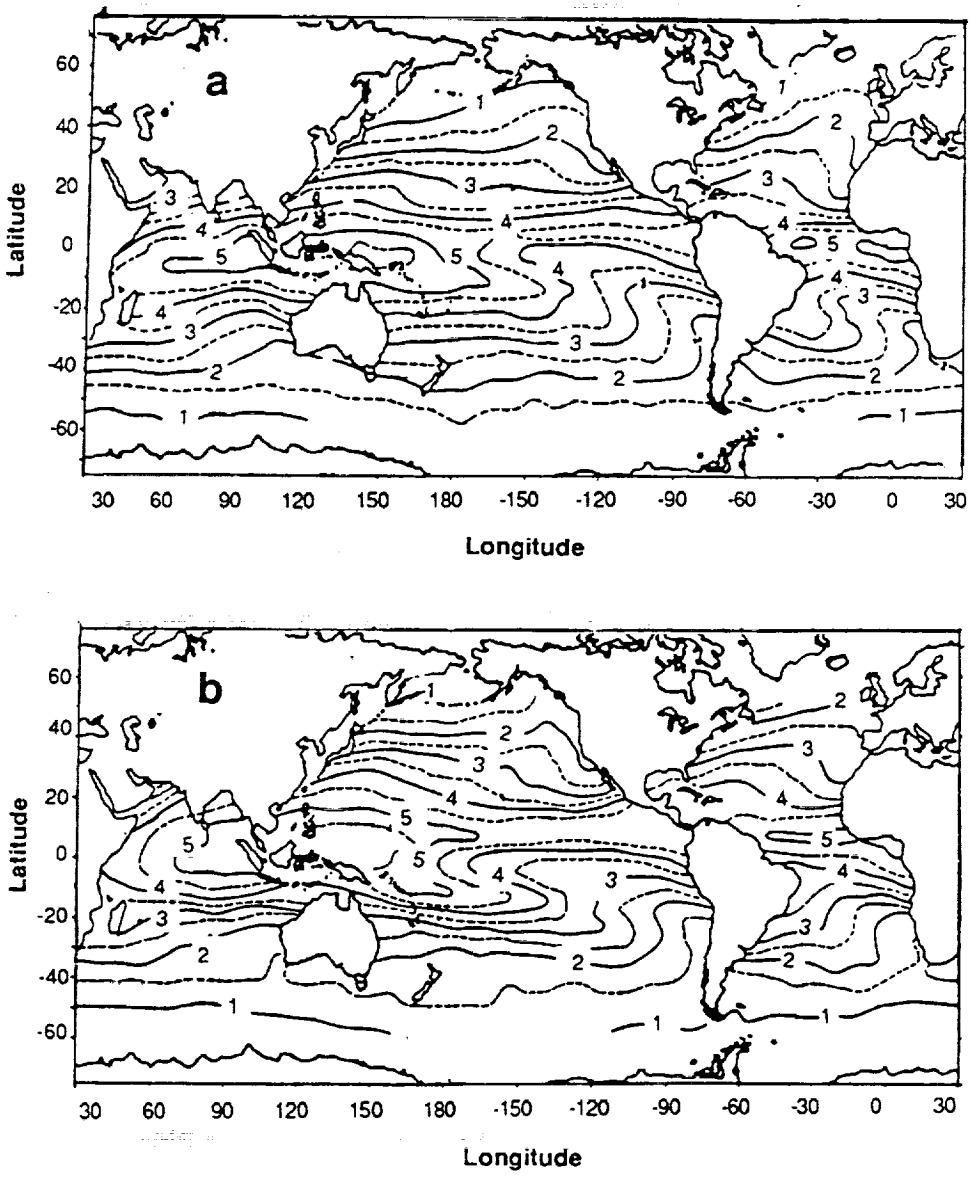

FIG. 12. Seasonal mean distribution of integrated water-vapor derived from SMMR over the global oceans for the period 1979–1981 (a) December–February, (b) September–November. The units are in grams per square centimeter (g cm^{-2}) (adapted from Prabhakara et al. 1985).

areas, when it pours over the relatively warm ocean, the surface flux of heat and moisture modifies this air strongly. Petterssen et al. (1962) calculated the sum of sensible and latent heat flux in the region west of a typical North Atlantic storm and found that it ranged from 100–400 W m^{-2}. In addition, Raman and Riordan (1988) found during the Genesis of Atlantic Lows Experiment (GALE) that a sum of sensible and latent heat flux of 800 W m^{-2} was common during cold-air outbreaks following midlatitude storm passages. This vigorous exchange of heat and moisture from the ocean to the cold air behind fronts is probably reflected in the slightly greater integrated water-vapor content in the minimum region in North Atlantic storms.

As mentioned in section 3, the sampling periods representing the Southern Hemisphere warm season and the Northern Hemisphere warm season do not have identical separation from the solstices. This was due to a lack of cases available in the Northern Hemisphere during the early warm season (July and August). However, if there were enough storms sampled during this time period, one would expect the maximum wa-

TABLE 3. Average maximum and minimum water-vapor content for cold fronts in mature cyclones. Average water-vapor content and standard deviation are given in kilograms per square meter (kg m^{-2}), and n is the number of cases.

Case	Maximum			Minimum		
	Average	Standard deviation	n	Average	Standard deviation	n
Warm season						
North Atlantic	42.0	4.5	18	16.6	4.6	23
North Pacific	34.9	6.0	28	13.0	3.2	24
Southern Ocean	25.3	3.9	27	9.0	1.9	26
Cold season						
North Atlantic	31.1	5.0	38	14.3	4.9	39
North Pacific	25.6	5.6	27	9.8	3.5	28
Southern Ocean	20.1	4.5	30	8.2	2.7	29

ter-vapor content in the vicinity of the cold fronts of early warm season storms to be the same as or greater than the water-vapor content in cold fronts of late warm season storms examined here. This is partly because the average water-vapor content in the North Pacific and North Atlantic is higher during the early warm season months (June–August) than during the late warm season months (September–November) (e.g., Fig. 2 of Prabhakara et al. 1985). On the other hand, in the Southern Ocean, the average water-vapor content does not change appreciably from early to late warm season and the storm frequency and intensity is about the same during the early and late warm season. Therefore, one would expect that the average water-vapor content in the vicinity of cold fronts in the Southern Ocean calculated in this study to be representative for the entire warm season. If the fortunate circumstances had existed so that the Southern Hemisphere and Northern Hemisphere warm seasons samples had been so chosen as to be exactly equidistant from the respective solstices, we have confidence that our general conclusions would have been similar.

In both the warm and cold seasons, the Southern Ocean average maximum and minimum water-vapor contents stand out as exceptionally low compared to the North Pacific and North Atlantic cases. In some respects, this could be due to a different large-scale circulation in the Southern Hemisphere. Several authors using a variety of data sources and analysis methods have arrived at the following characteristics of the general circulation (Trenberth 1980; Physick 1981; James and Anderson 1984): 1) the seasonal patterns of the surface pressure and 500-mb height are dominated by wavenumber 3 configuration with troughs typically at longitudes 110°E, 120°W, and 40°W; 2) the seasonal cycle is much less pronounced than in the Northern Hemisphere with a high frequency of transient cyclones throughout the year; and 3) the region of low-level baroclinicity and the high-latitude wintertime jet is further poleward than in the Northern Hemisphere. The most important feature that contributes to integrated water-vapor content of these three is the last, which implies that the jet and the storm and depression tracks tend to be at high latitudes in the Southern Ocean. This would presumably reduce the transport of warm moist air from lower latitudes by storm systems.

During the warm season, the Southern Ocean does not warm substantially. At 40°S it is roughly 15°C and at 50°S it is 10°C; whereas the North Pacific is 20°C and 14°C at these same latitude bands (van Loon 1984). In addition, the warm season integrated water-vapor content in the Southern Ocean ranges from 21 kg m^{-2} at 30°S to 15 kg m^{-2} at 50°S; whereas in the North Pacific, the range is from 30 kg m^{-2} at 30°N to 15 kg m^{-2} at 50°N (see Fig. 12). It appears that the lower sea surface temperatures and therefore lower atmospheric temperatures and mean atmospheric water-vapor contents in the Southern Ocean summer is probably the most important reason why there is such low moisture content in the Southern Ocean storms during the warm season.

It is somewhat puzzling that the Southern Ocean winter storms have significantly less total moisture than the North Pacific storms. In both regions the storms are predominately in the mature stages of development and the sea surface temperatures are climatologically the same, ranging from 17°C at 35° latitude to 7°C at 50° latitude (van Loon 1984) in both oceans during winter. There are several possibilities to account for this difference, including: 1) storms in the Southern Ocean occur significantly poleward of their North Pacific counterpart; and 2) Southern Ocean storms transport significantly less moisture poleward than the North Pacific storms.

In order to test the hypothesis that the Southern Ocean storms occurred significantly poleward of the North Pacific storms, the average latitude of the surface low pressure center for the Southern Ocean and the North Pacific storms used in this study was calculated. The average latitude of the Southern Ocean low pressure centers was 51°S and the average latitude of the

North Pacific low pressure centers was 49°N. However, the standard deviations were so large (σ = 7.0 for the Southern Ocean and σ = 6.5 for the North Pacific) that the difference between the averages was not significant. In addition, the average latitude of the cold fronts sampled in the Southern Ocean was 42°S and the average latitude of the cold fronts sampled in the North Pacific cold fronts was 38°N. Despite the large standard deviations (σ = 5.5 for the Southern Ocean and σ = 7.3 for the North Pacific), the averages are significantly different at the 97% confidence level. Therefore, there is limited evidence that the Southern Ocean cold fronts in this study were slightly poleward of the North Pacific cold fronts. However, the evidence does not appear sufficient to fully account for the differences between the water-vapor content in Southern Ocean storms and in North Pacific storms.

The second hypothesis that the Southern Ocean cold season storms transport significantly less moisture than the North Pacific storms is more difficult to test. Adequate three-dimensional wind and moisture information for all the cases examined here is lacking. However, several authors have computed the integrated water-vapor distribution and vertically integrated meridional and zonal components of moisture flux on seasonal time scales. With radiosonde and model derived information, Howarth (1983) calculated that the meridional component of moisture flux in the Southern Ocean region during winter months was 25 kg m^{-1} s^{-1}. Peixoto et al. (1981) performed a similar calculation using radiosonde derived information and computed a value of 89 kg m^{-1} s^{-1} for the North Pacific. They both attributed the poleward meridional flux of moisture to cyclone activity. In addition, the semipermanent Aleutian Low may play a role in the higher vapor content of North Pacific storms. Rasmusson (1972) showed that the zonally averaged meridional transport of moisture due to stationary eddies is significant. During the winter season in the Northern Hemisphere it accounts for approximately one-third of the total meridional transport of moisture. The Southern Ocean, on the other hand, does not have semipermanent features such as the Aleutian Low. This moisture transport may explain why the seasonal total integrated water-vapor content is slightly higher in the North Pacific basin than in the Southern Ocean (see Fig. 12), especially in the eastern North Pacific. The North Pacific storms, therefore, may occur in an environment with higher vapor content than the Southern Ocean storms on average. In any case, using the values calculated by Peixoto et al. (1981) and Rasmusson (1972), the relative contribution to the total meridional moisture flux by transient eddies in the North Pacific is approximately 60 kg m^{-1} s^{-1}, twice that calculated by Howarth for the Southern Ocean. These studies and others, support the hypothesis that Southern Ocean cold season cyclones transport less water vapor than the North Pacific cold season cyclones. Yet, without information on temporal and spatial scales of the cyclones themselves, this must remain an open question. Perhaps in the future, with high resolution wind information, much like that of the SEASAT Scatterometer, and high resolution water-vapor information, like that of the SMMR or the current Special Sensor Microwave Imager (SSM/I), the meridional flux of boundary-layer water vapor poleward in cold season midlatitude cyclones can be computed for these regions.

McMurdie (1989) found some interesting differences in maximum water-vapor content in cold fronts and warm fronts. The North Pacific and North Atlantic mature storms were found to have significantly higher maximum water-vapor content in cold fronts than in warm fronts. In addition, in the North Pacific cases, developing warm fronts have significantly more water-vapor than mature warm fronts. These observations can be partially explained by differences in the mean temperature of the air column at mature and developing warm and cold fronts. Mature warm fronts tend to lie significantly poleward of the mature cold front of the same system and of the position of the warm front during the storm's developing stage. In many cases, the air at the mature warm front has been modified and has cooled over time and mixed with the cooler air to the northeast resulting in lower water-vapor content at the mature warm front. Observations and modeling of the dynamical development of warm and cold fronts over time are consistent with the above observations (Eliassen 1962; Hoskins and Heckley 1981; Keyser and Pecnick 1987; and Levy 1989). These authors show that cold fronts continue to develop sharp temperature gradients and have strong convergence (and therefore higher moisture convergence) as the storm system develops, whereas warm fronts do not.

In this study, significant differences in average maximum and minimum water-vapor content were found between storms that occur in the North Atlantic, North Pacific, and Southern Ocean. In addition, there is limited evidence that the South Atlantic storms have much higher maximum water-vapor content than the Southern Ocean storms, lending observational evidence in support of the speculation of James and Anderson (1984) concerning the high transient activity in the South Atlantic. These differences in water-vapor content are attributed to differences in ocean temperatures and moisture advection and convergence. The relative importance of these mechanisms in explaining the differences were discussed. These observational results comprise the first documentation of typical water-vapor contents in midlatitude cyclones occurring in these regions. Full explanation of the regional and seasonal differences in water-vapor content of cyclones must await further studies probably incorporating diagnostic analysis of limited area or global numerical models.

Despite the limitations inherent in the SEASAT and Nimbus-7 SMMR, this study demonstrates what can be done with the SSM/I data on current and future DMSP satellites and eventually with data from the microwave radiometers in the Earth Observing System planned for 1995 and beyond.

Acknowledgments. This study represents a portion of one of the author's (LAM) Ph.D. dissertation. Thanks are extended to Iftekhar Bhatti and Grant Petty for help with data processing and computer programming and to Kay Dewar for assistance with the figures. This work was performed under NASA Contract NAS8-36473 with additional support from NASA Grant NAG5-943. The Nimbus-7 SMMR CELL-ALL data were processed by the SMMR information processing team of the Nimbus Project and provided to us by the National Space Science Data Center at Goddard Space Flight Center. One of the authors (LAM) acknowledges support from the Cooperative Institute for Meteorological Satellite Studies during preparation of this manuscript.

REFERENCES

Alishouse, J. C., 1983: Total precipitable water and rainfall determinations from the SEASAT Scanning Multichannel Microwave Radiometer (SMMR). *J. Geophys. Res.*, **88,** 1929–1935.

Anderson, R. K., J. P. Ashman, F. Bittner, G. R. Farr, E. W. Ferguson, V. J. Oliver and A. H. Smith, 1969: Applications of meteorological satellite data in analysis and forecasting. ESSA Tech. Rep. NESC 51 [Available from Govt. Printing Office, Washington.]

Born, G. H., J. A. Dunne and D. B. Lame, 1979: SEASAT mission overview. *Science,* **204,** 1405–1406.

Brown, R. A., and G. Levy, 1986: Ocean surface pressure fields from satellite sensed winds. *Mon. Wea. Rev.*, **114,** 2197–2206.

Bourke, W., K. Puri and R. Seaman, 1982: Numerical weather studies from the FGGE Southern Hemisphere database. *Mon. Wea. Rev.*, **110,** 1787–1800.

Carleton, A. M., 1980: Recent variations in winter extratropical cyclone activity for the Australian region. *Search,* **11,** 37–39.

Chang, H. D., P. H. Hwang, T. T. Wilheit, A. T. C. Chang, D. H. Staelin and P. W. Rosenkranz, 1984: Monthly distribution of precipitable water from the Nimbus-7 SMMR data. *J. Geophys. Res.*, **89,** 5328–5334.

Danard, M. B., 1964: On the influence of released latent heat on cyclone development. *J. Appl. Meteor.*, **3,** 27–37.

Eliassen, A., 1962: On the vertical circulation in frontal zones. *Geofys. Publ.*, **24,** 147–160.

Fleagle, R. G., N. A. Bond and W. A. Nuss, 1988: Atmosphere–ocean interaction in midlatitude storms. *Meteor. Atmos. Phys.*, **38,** 50–63.

Francis, E. A., 1987: Calibration of the Nimbus-7 Scanning Multichannel Microwave Radiometer (SMMR), 1979–1984. M. S. thesis, Dept. of Oceanography, Oregon State University, Corvalis, 248 pp.

Hadlock, R., and C. W. Kreitzberg, 1988: The Experiment on Rapidly Intensifying Cyclones over the Atlantic (ERICA) Field Study: Objectives and plans. *Bull. Amer. Met. Soc.*, **69,** 1309–1320.

Hoskins, B. J., and W. A. Heckley, 1981: Cold and warm fronts in baroclinic waves. *Quart. J. Roy. Met. Soc.*, **107,** 79–90.

Howarth, D. A. 1983: Seasonal variations in the vertically integrated water-vapor transport fields over the Southern Hemisphere. *Mon. Wea. Rev.*, **111,** 1259–1272.

James, I. N., and D. L. T. Anderson, 1984: The seasonal mean flow and distribution of large-scale weather systems in the Southern Hemisphere: The effects of moisture transports. *Quart. J. Roy. Meteor. Soc.*, **110,** 943–966.

Kalnay, E., R. Atlas, W. Baker and J. Susskind, 1985: GLAS experiments on the impact of FGGE satellite data on numerical weather prediction. *First National Workshop on the Global Weather Experiment,* 121–145.

Katsaros, K. B., and R. M. Lewis, 1986: Mesoscale and synoptic-scale features of North Pacific weather systems observed with the Scanning Multichannel Microwave Radiometer on Nimbus-7. *J. Geophys. Res.*, **91,** 2321–2330.

——, P. K. Taylor, J. C. Alishouse and R. J. Lipes, 1981: Quality of SEASAT Scanning Multichannel Microwave Radiometer (SMMR) atmospheric water determinations. *Oceanography from Space,* J. F. R. Gower, Ed., Plenum, 691–706.

——, I. A. Bhatti, L. A. McMurdie and G. W. Petty, 1989: Passive microwave measurements of water-vapor fields and rain for locating fronts in cyclonic storms. *Wea. Forecasting,* **4,** 449–460.

Keyser, D., and M. J. Pecnick, 1987: The effect of alongfront temperature variation in a two-dimensional primitive equation model of surface frontogenesis. *J. Atmos. Sci.*, **44,** 577–604.

Kim, S. T., D. Han and H. D. Chang, 1984: Analyses and correction of the brightness temperatures measured in the 21-GHz horizontal channel of the Nimbus-7 Scanning Multichannel Microwave Radiometer. SASC Tech. Rep. SASC-T-5-5100-0004-0026-84. 52 pp. [Available from the authors at Systems and Applied Sciences Corporation, 5809 Annapolis Road, Hyattsville, Maryland 20784.]

Levy, G., 1989: Surface dynamics of observed maritime fronts. *J. Atmos. Sci.*, **46,** 1219–1232.

——, and R. A. Brown, 1986: A simple, objective analysis scheme for Scatterometer data. *J. Geophys. Res.*, **91,** 5153–5158.

McMurdie, L. A., 1989: Interpretation of integrated water-vapor patterns in oceanic midlatitude cyclones derived from the Scanning Multichannel Microwave Radiometer. Ph.D. Thesis, University of Washington, Seattle, 223 pp.

——, and K. B. Katsaros, 1985: Atmospheric water distribution in a midlatitude cyclone observed by the SEASAT Scanning Multichannel Microwave Radiometer. *Mon. Wea. Rev.*, **113,** 584–598.

——, G. Levy and K. B. Katsaros, 1987: On the relationship between scatterometer-derived convergences and atmospheric moisture. *Mon. Wea. Rev.*, **115,** 1281–1294.

Peixoto, J. P., D. A. Salstein and R. D. Rosen, 1981: Intra-annual variation in large-scale moisture fields. *J. Geophys. Res.*, **86,** 1255–1264.

Petterssen, S., D. L. Bradbury and K. Pedersen, 1962: The Norwegian cyclone models in relation to heat and cold sources. *Geofys. Publ.*, **24,** 243–280.

Physick, W. L., 1981: Winter depression tracks and climatological jet streams in the Southern Hemisphere during the FGGE year. *Quart. J. Roy. Meteor. Soc.*, **107,** 883–898.

Prabhakara, C., H. D. Chang and A. T. C. Chang, 1982: Remote sensing of precipitable water over the oceans from Nimbus-7 microwave measurements. *J. Appl. Meteor.*, **21,** 59–68.

——, D. A. Short and B. E. Vollmet, 1985: El Niño and atmospheric water vapor: Observations from Nimbus-7 SMMR. *J. Clim. Appl. Meteor.*, **24,** 1311–1324.

Raman, S., and A. J. Riodan, 1988: The Genesis of Atlantic Lows Experiment: The planetary boundary-layer subprogram of GALE. *Bull. Amer. Meteor. Soc.*, **69,** 161–172.

Rasmusson, E. 1972: Seasonal variation of tropical humidity parameters. *The General Circulation of the Tropical Atmosphere and Interactions with Extratropical Latitudes,* R. E. Newell, J. W. Kidson, D. G. Vincent and G. J. Boer, Eds., The MIT Press, 203–210.

Reed, R. J., A. J. Simmons, M. D. Albright and P. Unden, 1988: The role of latent heat release in explosive cyclogenesis: Three examples based on ECMWF operational forecasts. *Wea. Forecasting*, **3**, 217–229.

Sanders, F., and J. R. Gyakum, 1980: Synoptic-dynamic climatology of the "bomb." *Mon. Wea. Rev.*, **108**, 1589–1606.

SEASAT 1981: Scanning Multichannel Microwave Radiometer IV (April 1981) report. JPL document No. 622-234 129 pp.

Smigielsky, F. J., and G. P. Elrod, 1985: Surface cyclogenesis as indicated by satellite imagery. NOAA Tech. Memo. NESDIS 9, 30 pp. [Available from the authors at the National Environmental Satellite Data Information Service of National Ocean and Atmosphere Administration, Washington, D.C. 20233.]

Trenberth, K. E., 1980: Planetary waves at 500 mb in the Southern Hemisphere. *Mon. Wea. Rev.*, **108**, 1378–1389.

van Loon, H., 1984: Climates of the Oceans. World Survey of Climatology, Vol. 15, Elsevier Science Publishers, 716 p.

Weldon, R. B., 1977: An ocean cyclogenesis—it's cloud interpretation. Satellite Application Information Note 77/7, NWS/NESS, 11 pp. [Available from the author at National Environmental Satellite Data Information Service of National Ocean and Atmosphere Administration, Washington, D.C. 20233.]

Wilheit, T. T., and A. T. C. Chang, 1980: An algorithm for retrieval of ocean surface and atmospheric parameters from the observations of the Scanning Multichannel Microwave Radiometer (SMMR). *Radio Science*, **15**, 525–544.

Tellus (1991), *43A*, 306–320

Quantitative comparison between simulated cloudiness and clouds objectively derived from satellite data*

By ELMER RAUSTEIN, *Geophysical Institute, University of Bergen Allégt. 70, N-5007 Bergen, Norway*, HILDING SUNDQVIST, *Department of Meteorology, Stockholm University S-106 91 Stockholm, Sweden* and KRISTINA B. KATSAROS, *Department of Atm Sciences, University of Washington Seattle, WA 98195, USA*

(Manuscript received 7 August 1990; in final form 8 January 1991)

ABSTRACT

The cloud cover and cloud water content obtained from integration of a limited area mesoscale prediction model are compared with the corresponding quantities derived from AVHRR and SSM/I satellite data. The model has an elaborate condensation-cloud parameterization scheme, in which cloud water is a prognostic variable. From AVHRR data, both cloud cover and liquid water content are retrieved by utilization of radiances from the visible, near infrared and infrared channels. From the 37GHz polarization difference in the microwave data obtained from SSM/I measurements, liquid water content is interpreted; this is only possible over the sea. An important feature of this comparison exercise is that the retrieved data are distributed on the same grid as the model. The difference between the simulation and the analysed cloud fields can thus easily be quantified and exhibited on the model domain. It is demonstrated that this type of retrieved meteorological parameters constitutes potentially useful data samples for quantitative verification of model simulations. There are some weaknesses in the retrieval methods that have to be removed before we can have sufficient confidence in the data to make quantitative verification meaningful. Furthermore, calibration against cloud parameters obtained through other measurements is necessary, although the three data sets show a remarkably good agreement in pattern and range of magnitude in the liquid water content. Even if improvements are needed, the present study has made it possible to make inferences about some deficiencies in the parameterization scheme of the model.

1. Introduction

During the past decade, a great number of numerical model studies have been devoted to investigation of sensitivity to cloud-radiation conditions in the atmosphere. By and large, it can be said that all those studies indicate that there is an important impact from the cloudiness on the resulting circulation in NWP models and GCM (see list of acronyms in Appendix) as well as in climate models (Manabe and Stouffer, 1980; Ramanathan et al., 1983; Röckner and Schlese, 1987; Wetherald and Manabe, 1988; Cess et al., 1989; Slingo, 1990). It can furthermore be stated that very little attention generally is paid to the model clouds themselves. With regard to the sensitivity to clouds, it is urgent that much more work be done on the problem of condensation-cloud parameterization. The more realistic the model cloudiness becomes, the more confidently we can draw conclusions from model results. In the most recent papers, a concern may be found about the realism in the model cloud fields (Wetherald and Manabe, 1988; Cess et al., 1989).

There are two aspects that must be considered in a parameterization problem. One is the derivation and development of parameterization schemes, the other is the verification that model results exhibit

* Contribution number 625.

a realistic behavior and distribution of, in this case, cloudiness.

The conventional ground-based cloud observations are incomplete and spatially too sparse to constitute a useful data set in the context discussed here. It is not until recently that relevant observational data have become available through satellite measurements. From the AVHRR data, it is now possible to make quantified interpretations of cloud cover and cloud water content (Raustein, 1989). From the microwave measurements, quantified cloud water content and precipitating water content may be deduced (Staelin et al., 1976; McMurdie and Katsaros, 1985; Takeda and Liu, 1987; Katsaros et al., 1989; Petty, 1990; Curry et al., 1990; Katsaros et al., 1990).

The satellite measurements also have their limitations. Cloud classification from AVHRR data utilizes channels both in the infrared (IR), and in the visible part of the spectrum. The interpretations are sensitive to sun elevation, and criteria for distinguishing between clouds and snow are not currently included in the method. Furthermore, microwave data can only be used over ocean areas.

The interpretation of both AVHRR data and microwave data are in an early stage of development. This means that the "observations" obtained this way have some degree of uncertainty, especially in absolute values.

There is another important aspect that is common to all of these satellite measurements. Namely, they give the vertically integrated value of the measured quantities. These do not necessarily reflect a unique vertical distribution (Slingo and Slingo, 1988).

Because of the development stage of the interpretation schemes and because of the two-dimensionality of the measurements, it is important that we utilize as many categories of measurements as possible for the model verifications. A careful comparison of corresponding measurements by different methods, as well as comparison of model results and measurements, may assist in calibrating the observations. In this way an enhanced confidence in the observations may gradually be achieved.

In order to verify simulated vertical distributions, it hence appears necessary to obtain observations also in other ways, such as from dedicated field programs such as, for example, FIRE (Cox et al., 1987). Then, as condensation-cloud parameterization schemes begin to show an acceptable performance, those schemes can be utilized to infer vertical distributions from satellite measurements.

There is a long way to go before we have reached a satisfactory state with regard to observational data of condensation-cloud quantities, as well as a realistic simulation of those quantities in various models. Considering the attention the cloud topic has gained recently, it is indeed urgent to intensify the research efforts in both modelling of condensation-cloud processes and in the verification of those simulations.

We are therefore of the opinion that, at the present state of the art, cloud parameters, derived from satellite data, are not yet quite ready to be used for direct absolute verification of model simulations. But to improve this situation, it is necessary to go through a development phase, in which we make comparisons between interpreted variables and model variables. This is the purpose of the present paper. A study along similar lines has recently been published by Saunders (1989).

The simulated cloudiness is produced in a NWP model (the AMUB model, which is a version of the operational model of the Norwegian Weather Service, modified at the University of Bergen), which has an elaborate condensation-cloud parameterization scheme.

The observed cloud parameters are obtained from two sources. One comprises cloud cover and vertically integrated liquid water content, objectively derived from satellite AVHRR data according to the approach suggested by Raustein (1989). The other data set is vertically integrated liquid water content, which is obtained by interpretation of satellite microwave measurements according to Petty (1990).

One model field which would have been desirable to compare to a corresponding satellite data field, is that of total outgoing longwave radiation. However, this field is not available from the satellite data we are using, as they are taken only from a few window bands.

Specifically, comparisons are made between clouds, predicted with the AMUB model and satellite clouds at times differing by not more than half an hour to one hour. An important feature of this study is that the cloud parameters from the

satellite data are projected on the same grid as the model.

2. Model features and the derivation of cloudiness from AVHRR and SSM/I microwave data

2.1. Model features

The AMUB model is a modified version of the operational fine mesh model at the Norwegian Weather service (DNMI). A description of the original version may be found in Grønås et al. (1987) and Nordeng (1986). The modifications introduced at AMUB are described by Sundqvist et al. (1989). Consequently, here we only present the broad features of the AMUB model. This limited area model is based on the primitive equations with sigma as vertical coordinate. In the experiments presented here, the horizontal resolution is 50 km and there are 10 levels in the vertical, with the top at 200 mb. The number of grid points at each level is 49×61; the geographical area that is covered may be seen in Fig. 4.

The time integration is explicit, but the scheme contains spatial and temporal smoothing of the tendencies in the staggered grid so that the time step is nearly four times as long as the one basically obtained from the CFL condition (Bratseth, 1983). Vertical eddy diffusion is applied through the whole depth of the model atmosphere. The exchange coefficient is a function of the Richardson number and cloud cover. The sea surface temperature is prescribed, while over land, an energy exchange equation is applied as well as a soil moisture formulation, accounting for precipitation, storage and run off. Radiative fluxes are calculated at all model levels. The fluxes are modified with regard to the current cloud cover obtained from the condensation-cloud parameterization. The emissivities are not functions of the cloud water content, but prescribed with different values for high, medium high and low clouds.

As indicated, the particular feature of the AMUB model is that an elaborate condensation-cloud parameterization scheme is employed. This scheme carries cloud water as a prognostic variable and treats release of latent heat, appearance of fractional cloud cover, cloud water content and precipitation/evaporation in a consistent way (Sundqvist, 1988; Sundqvist et al., 1989).

The parameterization of the *microphysical processes* accounts for coalescence as well as Bergeron-Findeisen effects. This scheme is *common for convective and stratiform* condensation, but the associated parameters have different values in the two stability regimes.

For the parameterization of *convective condensation*, a modified Kuo scheme is employed. The scheme includes calculation of cloud water. The partitioning of converging vapour between moistening and condensation is essentially governed by the relative humidity. The fractional cloud cover is a function of the intensity and the depth of the convection. The condition for *stratiform condensation* to appear is that the relative humidity is greater than a prescribed threshold value, which is different over sea and land. The fractional cloud cover is a linear function of the square root of the sub-saturation. The *cloud water advection*, which is only horizontal, is calculated with an upstream scheme to assure positive definite cloud water values.

2.2. Derivation of cloud parameters from AVHRR data

The method of deriving fractional cloud cover and vertically integrated liquid water content (LWC) is described by Raustein (1989). A brief description of the method is given below.

Three of the AVHRR channels are utilized, viz. *channel 1* (0.58–0.68 μm, visible), *channel 2* (0.7–1.1 μm, near infrared), and *channel 4* (10.5–11.5 μm, infrared). First a statistical method called clustering is applied to the data of channels 1 and 4 to obtain an objective cloud classification. In the two-dimensional radiance space, we find concentrations of pixels (called clusters), which we identify as certain cloud types, or as either land or sea surface. Pixels belonging to a certain cluster contain clouds of the same type, and the area covered by such a pixel is assumed to be overcast. Pixels that are scattered and thus not belonging to a cluster are overcast or partially cloudy. The cloud fraction of such a pixel is found in two steps: (a) The cloud type, to which the clouds in the pixel belong, is obtained by finding the cloud cluster, to which the pixel is closest in the 3-dimensional radiance space, where the 3 dimensions are the radiances of channels 1, 2 and 4. (b) The cloud

fraction is then found by linearly interpolating the pixel's channel 2 radiance between the surface cluster's mean, and the closest cloud cluster's.

To compute the LWC and cloud top temperature we use radiative transfer models of Coakley and Chylek (1975) and Arking and Childs (1985), together with parameterized LWC and channel 4 emissivity according to Stephens (1978).

In order to have the cloud parameters derived from the satellite data projected on the same grid as the model, a navigation method developed by Kloster at NRSC (personal communication) is used to position each pixel in the model grid. The grid box value of each cloud parameter is then taken as the average of the values of the pixels which belong to the grid box.

2.3. *Derivation of liquid water content from microwave data*

The microwave data are from the SSM/I on the F8 satellite in the US Defense Meteorological Satellite Program (DMSP), which was launched into a polar orbit in June 1987. This microwave radiometer scans a 1390 km wide swath in a conical sweep at 53° incidence angle. Operating frequencies are 19.35, 22.235, 37 and 85.5 GHz, in both horizontal and vertical polarization, except the 22.235 GHz channel, which only operates in horizontal polarization. The pixel resolution is nominally 50, 50, 25 and 15 km, respectively. Several possible algorithms for determining cloud liquid water content have been developed (e.g., Petty, 1990). For the purpose of this model-satellite data comparison, a 50-km resolution-integrated cloud liquid water algorithm based on the 37 GHz polarization was selected. For higher spatial resolution and better discrimination, an algorithm employing the 85.5 GHz channels has been developed (Petty, 1990). Unfortunately, this algorithm cannot be used for our August 1988 case, due to gain problems with the 85.5 GHz channel in vertical polarization, which had started shortly before this time.

The 37 GHz algorithm is based on the theoretical depolarization effect of the cloud droplets on the polarized emission from the sea surface. A relation between the observed polarized signal, P, and vertically integrated liquid water mass, L ($\equiv$LWC), is of the following form (Petty, 1990):

$$P = \tau_1^{\alpha} = \exp\left[-\frac{\alpha\kappa L}{\cos\theta}\right], \qquad (2.1)$$

where τ_1 is effective, microwave transmittance associated with the cloud liquid water, α has the approximate value 2, κ is effective mass extinction coefficient of the liquid water in the cloud and θ is the incidence angle (53°).

The relation for L_{37} in terms of polarization at 37 GHz ($T_{37V} - T_{37H}$) has been found from a theoretical brightness temperature model, which provides values for $\alpha \cdot \kappa$:

$$L_{37} = -1.42 \ln(P_{37}) \qquad (\text{kg m}^{-2}). \qquad (2.2)$$

P_{37} includes corrections for changes in the background, that is the wind roughening of the sea surface and water vapour in the column. Thus

$$P_{37} = (T_{37V} - T_{37H}) \times \exp(0.151U + 0.00607V - 4.40), \qquad (2.3)$$

where U is surface wind speed and V is water vapour content (SI units), also available from SSM/I brightness temperatures. Further details on the derivation of the complete and self-consistent set of algorithms developed to interpret SSM/I data are found in Petty (1990). Similar approaches to derive liquid water amount from microwave data are reported in Curry et al. (1990) and Takeda and Liu (1987).

It is pertinent to note that the liquid water content (LWC) derived from AVHRR as well as from microwave data comprise both cloud water and precipitating water. Thus there are reasons to expect that the analysed amounts should tend to be somewhat larger than the vertical integral of the simulated water content, which stems only from the clouds. We use the notation LWC both for analysed and simulated amounts, even if the latter ones strictly could be called cloud water content (CWC).

3. Comparison of model clouds and clouds derived from satellite measurements

3.1. *Choice of situation*

As mentioned above, there may be difficulties in the interpretation of AVHRR data at low sun

elevations and over snow covered surfaces. We have taken those aspects into account in our choice of situation for this first comparison. Furthermore, in order to make use of microwave data, we have looked for a cloud system that has its major parts over the sea surface during the period of comparison. This implies that there are very few conventional surface observations available for verification. We also wanted to find a situation with a pronounced non-stationary cloud system under motion during the simulation period.

Thus, we are considering a situation with initial time at 26 August 1988 12 GMT and the 30 h forecast (till 27 August 1988 18 GMT). The synoptic surface map is shown in Fig. 1. During this period, we have AVHRR data centred around 27 August 1988 8.45 GMT (Fig. 2), which we call Sav1 in the sequel, corresponding to +21 h simulation time, and 27 August 1988, 14.30 GMT (Fig. 3), Sav2, corresponding to +27 h. We have microwave data centred around three different points in time, one at 26 August 1988, 19.00 GMT, (around +6 h), another at 27 August 1988, 4.30 GMT, (around +16 h) and a third one from 18.30 GMT, (around +30 h); the last mentioned we call Smi3. It may be pointed out that in all those cases, the extracted satellite data cover only part of the computational area.

3.2. *Cloud cover from model and AVHRR measurements*

The cloud cover in the forecast model is defined at each level, so we have to calculate a 2-dimensional field of the cover, corresponding to what a satellite sees. There are three basic alternatives for such a calculation, namely, assumptions that clouds at different levels have either minimum, maximum or random overlap. There is of course some arbitrariness in each of the options. According to a recent study by Tian and Curry (1989), the two last mentioned alternatives are more realistic than the first one. We have adopted a maximum/random overlap assumption, imply-

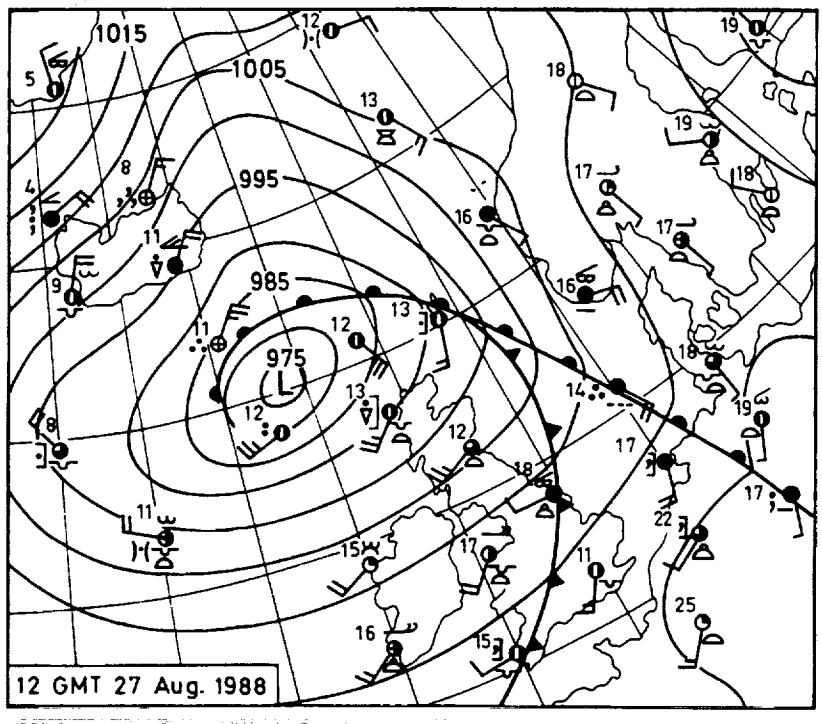

Fig. 1. Surface analysis at 12 GMT 27 August 1988.

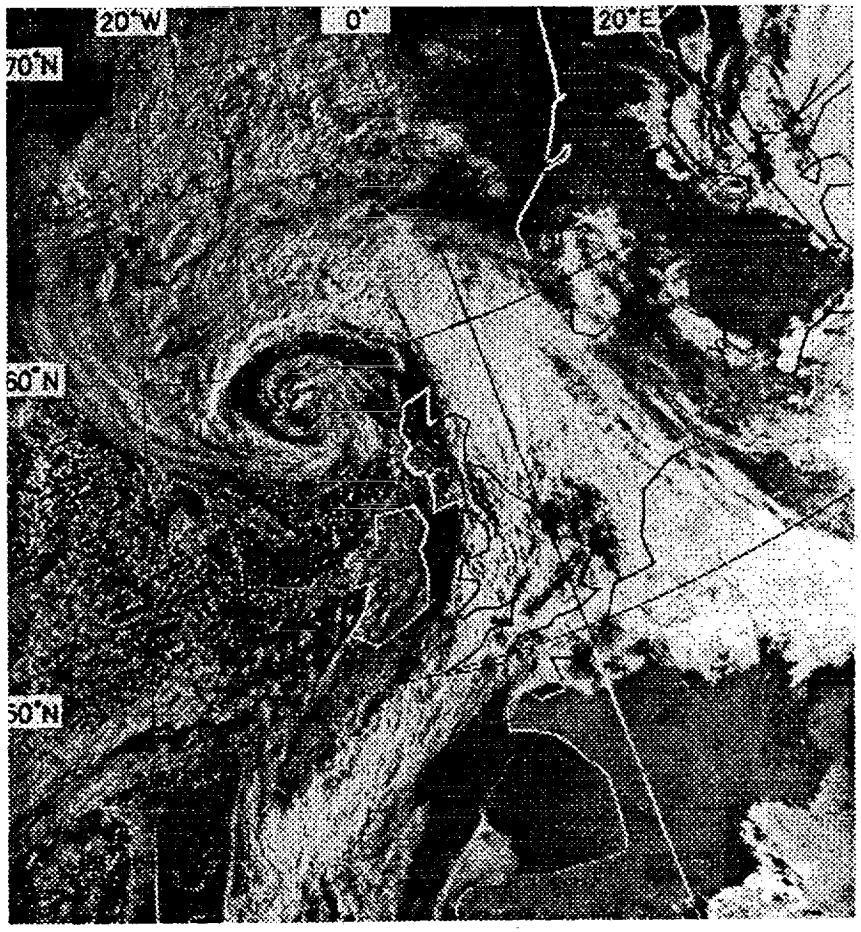

Fig. 2. Satellite (NOAA 10) picture in near infrared (channel 2) from passage 27 August 1988 around 8.45 GMT. (Satellite Receiving Station, Dundee University, UK.)

ing that maximum overlap is used as long as the cover varies monotonically from level to level in a column and that random overlap is taken when non-monotonic variation occurs in the same column (Sundqvist et al., 1989).

Figures 4a–b show that there is good overall agreement between Savl and the simulated cover at the corresponding time. One of the first things that we notice is that the satellite analysis has a somewhat larger overcast area than the model field. This disagreement is seen over the Gulf of Bothnia and over the area behind the cold front east of Scotland-England where the clear area is more extended in the model field than in the analysis. A corresponding deviation is also found south-west of Ireland. The synoptic map shows that a frontal wave is under development in this area. To see those differences quantitatively, we have subtracted the model cloud cover from the observed one in Fig. 4c. The differences mentioned above are clearly seen in this figure. These deviations, where the analysis shows practically overcast while the model field is cloud-free, could possibly be due to an uncertainty in the condensation scheme as to what the (threshold) conditions should be for condensation to appear. But it seems more likely that those deviations are due to the model dynamics, which may fail in simulating

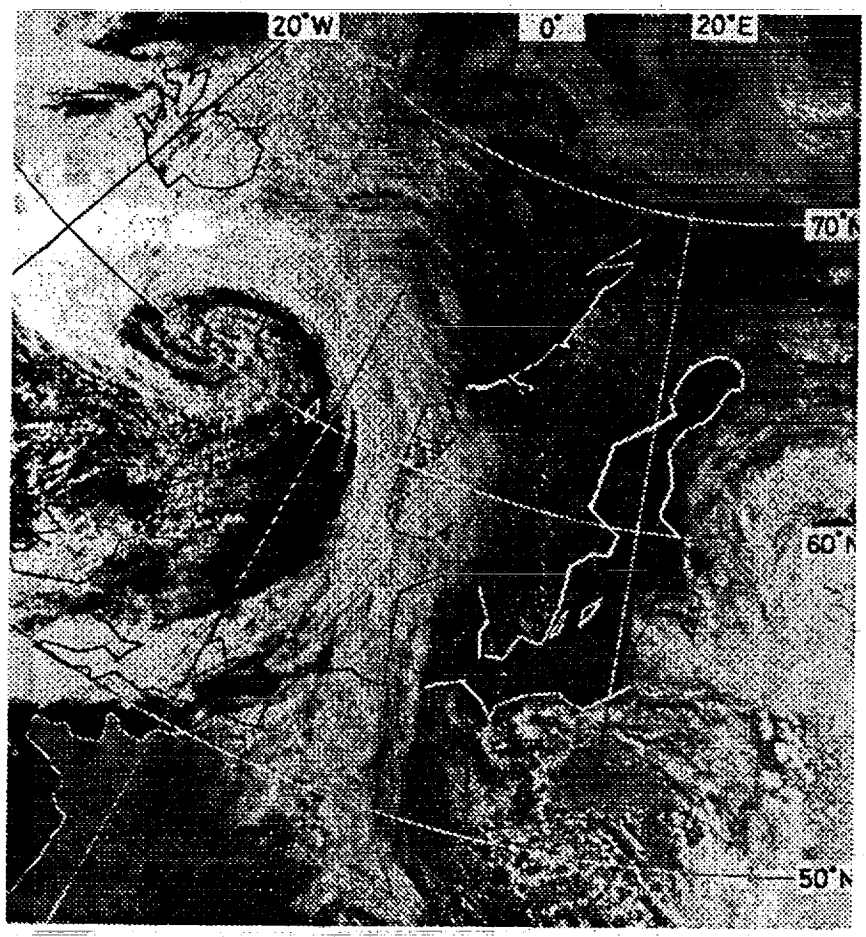

Fig. 3. Satellite (NOAA 9) picture in near infrared (channel 2) from passage 27 August 1988 around 14.30 GMT. (Satellite Receiving Station, Dundee University, UK.)

realistically the motions connected with (a) the fairly weak pressure gradients through a great depth over central Sweden and the Gulf of Bothnia, (b) the relatively small scale features behind the cold front, and (c) the developing wave entering through the southern boundary of the model area.

In the south-west sector of the low, where convection is taking place (Fig. 2), there are somewhat more negative than positive differences (Fig. 4c). This is even more evident in the water amount difference as we will see below. The synoptic observations in Scotland and Ireland report shower activity with cloud cover between three and seven octas. These features indicate that the interpretation of the AVHRR data has more uncertainty over areas with scattered convection.

Near the northern boundary of the analysis region, the difference pattern, with its positive values to the north and negative values to the south, indicates that the model may have a phase error in this condensation system.

The narrow band of negative values, implying more clouds in the model than in the analysis, just north and west of the low pressure centre is also worth noting in Fig. 4c. Fig. 2 exhibits a narrow cloud-free band, which evidently cannot be resolved by the model. From Fig. 4b it is seen that

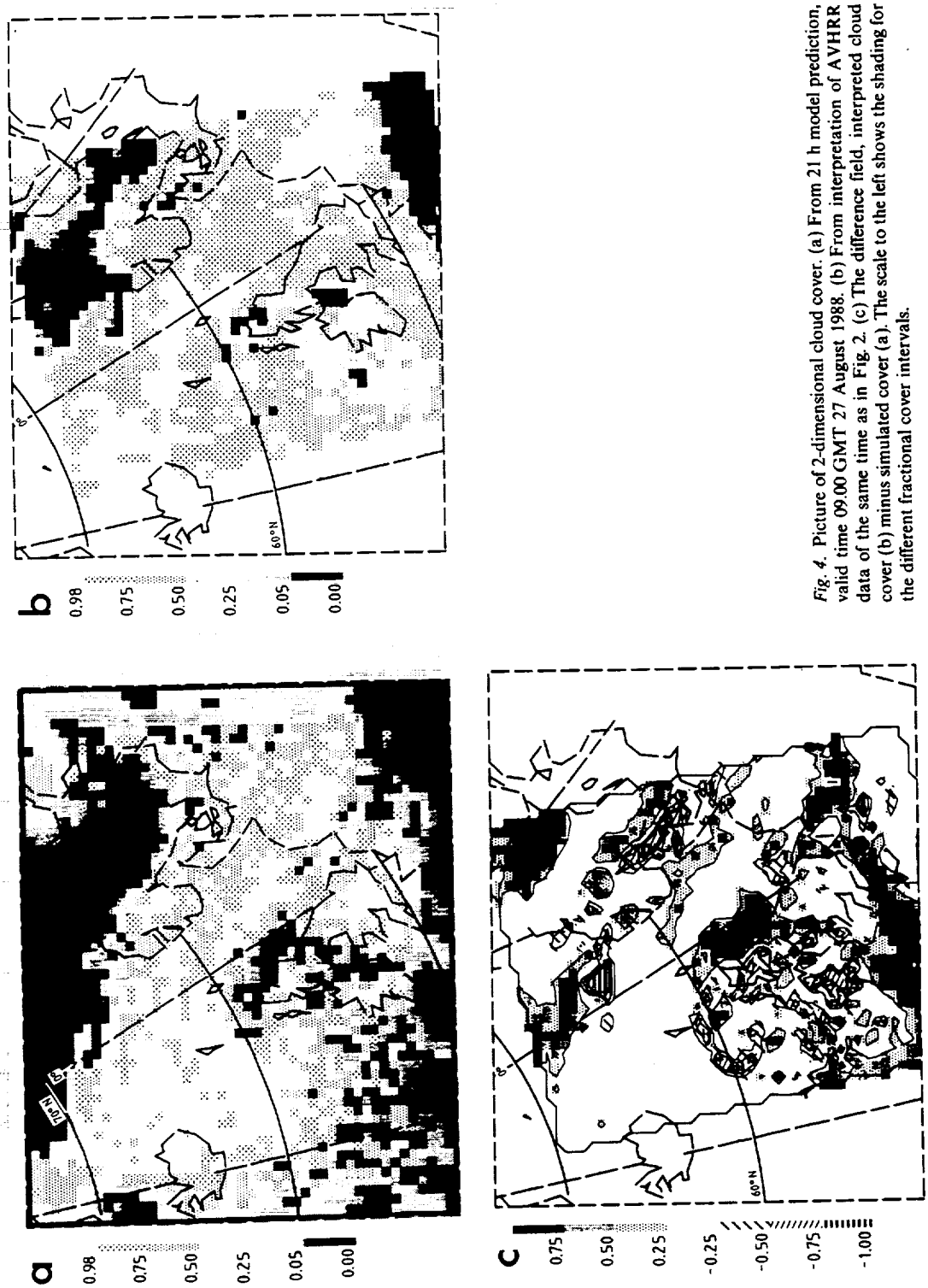

Fig. 4. Picture of 2-dimensional cloud cover. (a) From 21 h model prediction, valid time 09.00 GMT 27 August 1988. (b) From interpretation of AVHRR data of the same time as in Fig. 2. (c) The difference field, interpreted cloud cover (b) minus simulated cover (a). The scale to the left shows the shading for the different fractional cover intervals.

the analysis on the model resolution also loses the cloud-free feature and shows a partly cloudy band.

There are several areas with positive values in Fig. 4c that are interesting. As examples we may particularly regard the area along England's east coast, and the band beginning at 60°N and west of Norway and running toward SSE just west of Jutland into Western Germany. In these cases, the model simulates fractional cloudiness ranging between 25 and 75%, while the analysis shows a cover that systematically is 15–50 units larger. These discrepancies are probably due to the model's parameterization scheme for condensation. Thus, it is likely that the scheme tends to underestimate the *fractional stratiform* cloud cover.

We may also make a more statistical comparison by considering the following numbers: in the analysis area, the analysed clouds are present at 1560 gridpoints with an average cover of 66%, while the model clouds are present at 1310 gridpoints yielding a mean cover of 53%. Fig. 5 shows a frequency distribution of cloud cover categories for both the analysed clouds and the model clouds.

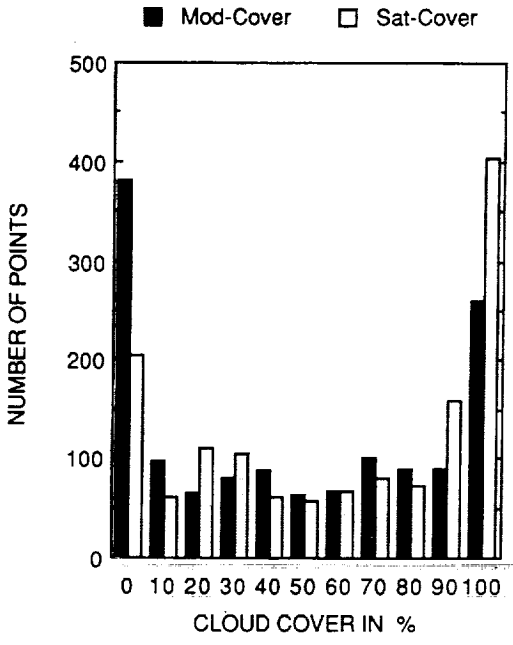

Fig. 5. Frequency distribution of cloud cover categories for the analysed clouds and the model clouds. The case is that of Sav2 and the forecast is for +27 h.

We have here chosen the time of Sav2, at which the comparison exhibits essentially the same results as those shown in Figs. 4a–c. From Fig. 5 we see that the analysed and the simulated cloud covers have an over all similarity in their bimodal distributions. But there are discrepancies, which are most pronounced in the extreme categories, that is, for zero and for 100%. There are markedly more cloudfree points and fewer overcast points in the simulated case than in the satellite analysis. This circumstance again shows the model's tendency to underestimate the cloud cover.

3.3. *Cloud water content from model and AVHRR measurements*

The satellite derived liquid water content is compared with the vertical integral of the predicted cloud water content. We noted earlier that the 2-dimensional cloud cover suffers from some arbitrariness due to the necessary assumption about overlapping; this is not the case with the vertically integrated water content, which is a well defined quantity.

As in the case of cloud cover, there is good qualitative agreement between the simulated cloud water field and the one obtained from the satellite measurements. Figs. 6a–b show that the simulated water content has a somewhat wider spread than found in Sav1, where the higher values appear in narrower bands. The maximum values are much the same, although there seems to be a few more points with the high values (more than 1.5 kg m^{-2}) in the Sav1 field (over Western Germany).

Fig. 6c shows the difference between the satellite derived water content and the model's vertically integrated cloud water amount. We may first observe the difference in the convection mentioned above in connection with convective cloud cover. In Fig. 6c, the simulated water amount is higher than the analysed amount over Scotland and western Ireland, and over the sea west of there. Regarding this discrepancy together with the synoptic reports and cloud cover differences shown above, it appears likely that the interpretation of the AVHRR data underestimates the convective cloud cover and water amount. There is also a band along the front from Cornwall toward ENE through England where the simulated water amount is higher than the analysed one, but in this

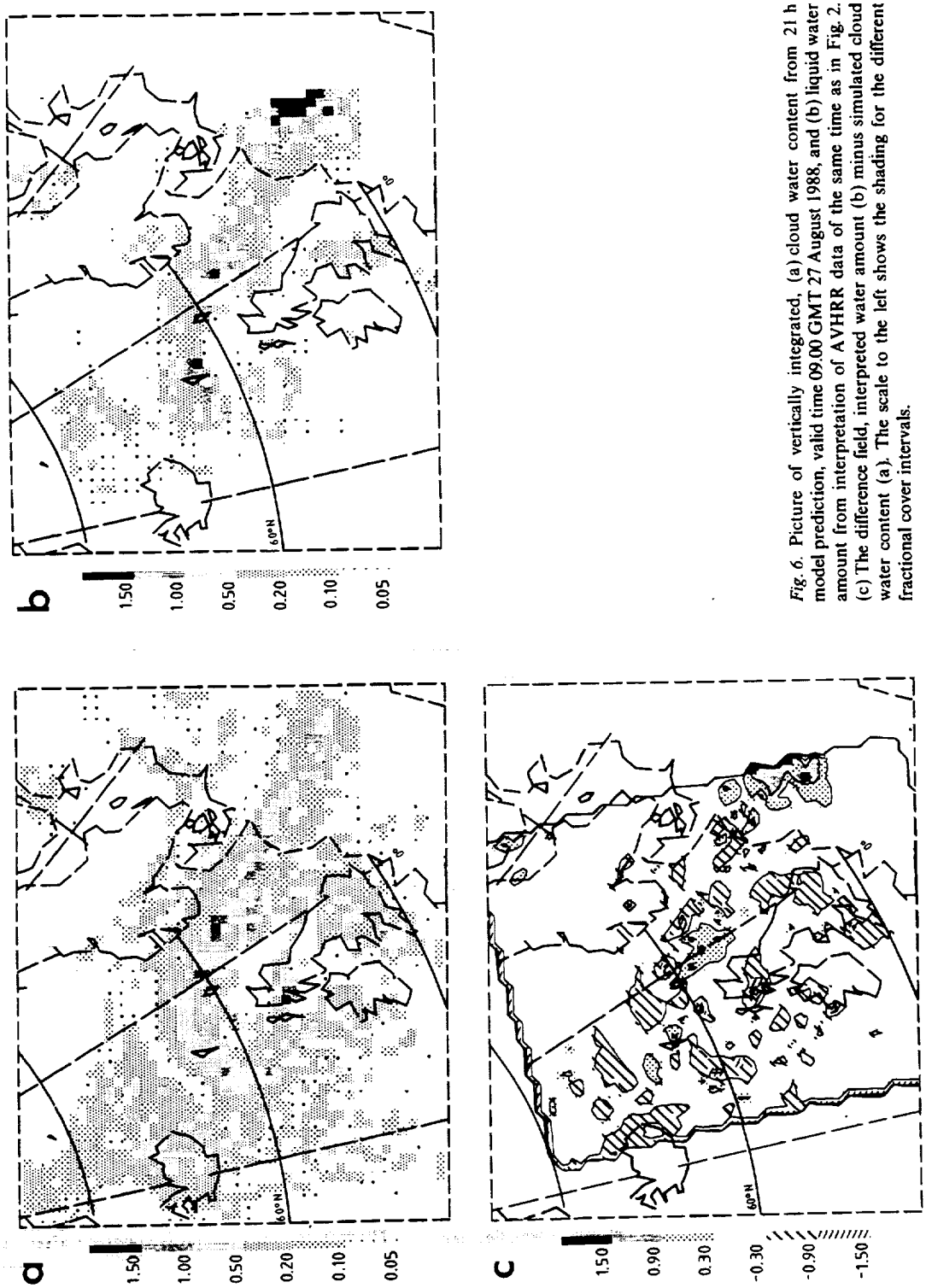

Fig. 6. Picture of vertically integrated, (a) cloud water content from 21 h model prediction, valid time 09.00 GMT 27 August 1988, and (b) liquid water amount from interpretation of AVHRR data of the same time as in Fig. 2. (c) The difference field, interpreted water amount (b) minus simulated cloud water content (a). The scale to the left shows the shading for the different fractional cover intervals.

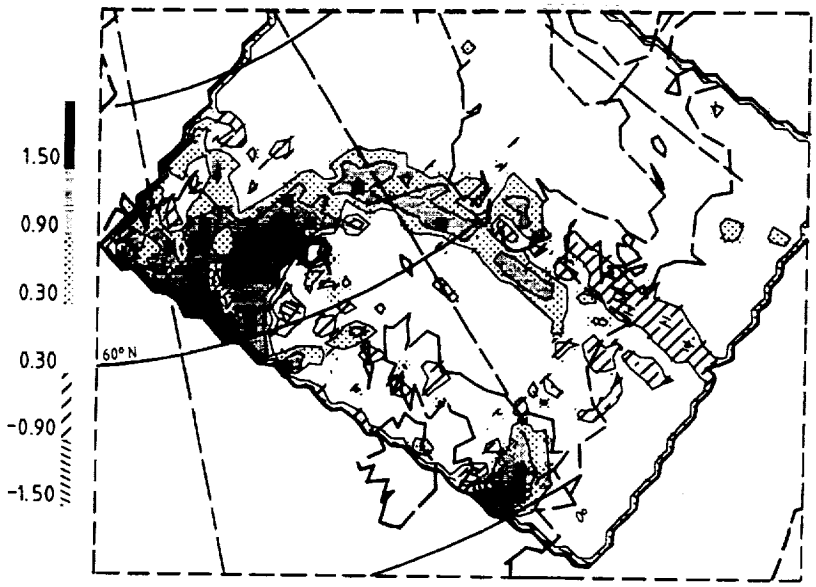

Fig. 7. The difference field, interpreted water amount at the time of Fig. 3, minus simulated cloud water content from +27 h of the model prediction. The scale to the left shows the shading for the different amount intervals; unit, $kg \cdot m^{-2}$, (or mm water column).

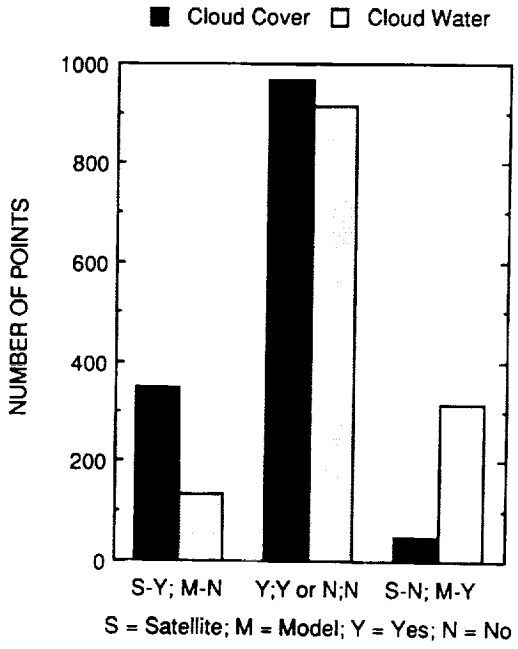

Fig. 8. The figure exhibits the number of grid points of agreement and of disagreement between observation and simulation for cloud cover and for cloud water content.

case it is more difficult to judge which of the two fields is the more realistic one.

At the time of Sav2, Fig. 7, there is a more distinct difference in the cloud water content, with the higher values in the measured field. However, there is better agreement in the spatial distribution than at the time of Sav1. The degree of spatial agreement at the time of Sav2 is indicated in another way in Fig. 8, which depicts the number of grid points of agreement and of disagreement between observation and simulation for cloud cover as well as for cloud water content. The figure also shows that the model underestimates cloud cover. Furthermore, the figure indicates that there is a discrepancy between the number of points with cloud cover and the number of points with cloud water. A slight contribution to this discrepancy may come from the model output, because the fields of cover and water differ by one time step. But the major contribution appears to come from the analyses, in which we found a distinct difference between Sav1 and Sav2 in spatial spread of cloud water. This question is directly connected to the matter discussed in the next paragraph.

There is one feature that is apparent when looking at Figs. 2 and 3, namely that the clouds appear

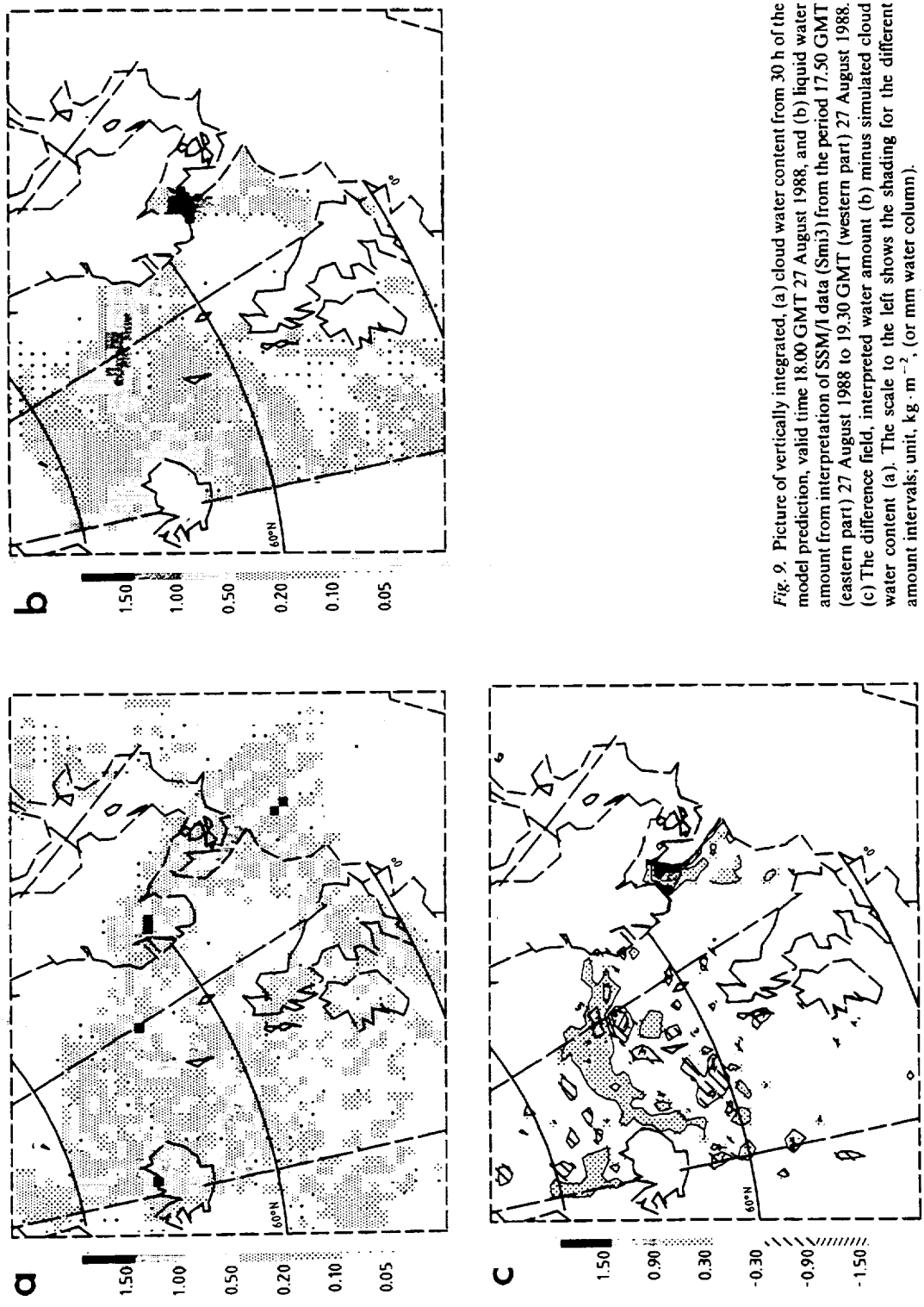

Fig. 9. Picture of vertically integrated, (a) cloud water content from 30 h of the model prediction, valid time 18.00 GMT 27 August 1988, and (b) liquid water amount from interpretation of SSM/I data (Smi3) from the period 17.50 GMT (eastern part) 27 August 1988 to 19.30 GMT (western part) 27 August 1988. (c) The difference field, interpreted water amount (b) minus simulated cloud water content (a). The scale to the left shows the shading for the different amount intervals; unit, $kg \cdot m^{-2}$, (or mm water column).

considerably brighter on the same side of the picture as where the sun is, as seen from the satellite. This has to do with the anisotropy in the bidirectional reflectivity, as reported by Taylor and Stowe (1984). When calculating the LWC from the satellite data, we have regarded the clouds as isotropic reflectors, so the anisotropy may explain some features that seem somewhat unrealistic. For example, from Fig. 6c we see that, in the eastern part, the satellite derived LWC at 8.45 GMT is higher than the simulated one at +21 h. Correspondingly we see from Fig. 7 that the analysed LWC at 14.30 GMT is considerably higher than the simulated one at +27 h in the western part. Those substantial positive deviations may in part be explained by the anisotropy, but it is apparent that some of them are due to underestimates in the model. For instance, the synoptic map at 09.00 GMT shows a rainband over West Germany and the synoptic map at 15.00 GMT shows a rain area over southern England and to the south of Iceland. The relatively high values of LWC from the satellite analysis are thus indirectly corroborated by other observations, while the simulated precipitation is nearly negligible in the same areas. The area of positive difference in Fig. 7, extending from about 0E, 62N southward along the west coast of Norway, may be explained by the fact that the precipitating water is not included in the model LWC. The simulated 3 h precipitation at +27 h is significant in this area. Most of the alternating positive and negative differences in the North Sea in Fig. 6c are due to the later time of the analysed frontal cloud band compared to the simulated cloud band in this area.

3.4. Cloud water content from model and SSM/I measurements

The LWC derived from the microwave data is compared with the vertical integral of predicted cloud water content. As indicated in Subsection 3.1, we have performed comparisons at three different points in time. As the results of those comparisons are essentially the same, we have chosen to show the results from the +30 h simulation (Fig. 9a) and Smi3 (Fig. 9b). The difference, Smi3 minus the simulation, is exhibited in Fig. 9c. The comparison is relevant only over the sea, since the microwave interpretation only exists there. It is seen that even in the +30 h forecast, there is remarkably good agreement between the positions of the frontal bands in Figs. 9a and 9b. An area of positive differences over Skagerack west of Sweden is seen in Fig. 9c. According to the synoptic map of 18.00 GMT, it is raining over that area, thus indicating that the numerical forecast underestimates the LWC. East of Iceland there is a band of positive differences, and a somewhat less coherent negative one south of that band. This situation indicates that the simulated system has a phase lag. However, this may, to some extent, be fictitious since the western part of the satellite analysis is from the satellite pass at about 19.30 GMT.

4. Summary

In the present study, cloud cover and cloud water content from a NWP model have been compared to the corresponding quantities derived from radiances measured by AVHRR and SSM/I on satellites. It is demonstrated that this type of retrieved meteorological parameters constitute potentially useful data samples for quantitative verification of model simulations. The results obtained in this pilot exercise are indeed encouraging. But there are some weaknesses in the retrieval methods that have to be removed before we can have sufficient confidence in the data to make quantitative verification meaningful. For instance in the retrieval methods applied to AVHRR data, it is necessary to treat the anisotropic reflectance more accurately. The constraint that the sun elevation is above a certain limit should be eliminated. The results of the present study indicate that the interpreted cloud cover in convective areas may have an unsatisfactory uncertainty. Furthermore, the inability to distinguish between snow cover and clouds is a very important difficulty that has to be removed so that the method can be applied with confidence at all times of the year.

As for the liquid water content, there is no straightforward answer to what is the best estimate, the simulation or the analysis. However, by utilizing precipitation reports on synoptic maps, we have some possibility to make a judgement over areas where the simulation and analysis have clear differences.

It is necessary that data from direct measurements (e.g., from FIRE and alike) are

utilized for calibration of the retrieved cloud parameters. To allow calibration of interpretations of microwave data, it is desirable that some dedicated field experiment is undertaken over ocean areas. Cloudiness produced in model simulations may also be compared with data from in situ measurements; an estimate of the simulated water content in the cloud proper is obtained by dividing the integrated water amount of a grid column with the associated cloud cover.

Despite uncertainties in the observational data considered here, it has yet been possible to infer some weaknesses in the model's parameterization scheme, by regarding the quantitative differences between analysis and simulation. Hence, it is found that the scheme has difficulties in handling the extremes of cloud cover in stratiform situations; there appears to be an underestimate of the cases with 100% cover and an overestimate of cloud-free areas.

Extensive utilization of the potential that retrieved cloudiness from satellite measurements represent will lead to improvements and refinements in the interpretation methods. So the sooner we begin to make use of those data, the sooner we will acquire a satisfactory level of accuracy and confidence in the retrieved data. In turn, this will facilitate improvements and refinements in the condensation-cloud parameterization schemes. As our parameterization schemes improve, we can utilize them to derive the vertical distribution of condensation and cloud processes. It will then be possible to improve the humidity analysis as well as to establish initial states of release of latent heat and of cloud water content. A confident description of the latent heating is of great value in the initialization process. As more advanced condensation-cloud schemes become adopted in prediction models, it will be of great importance (e.g., for minimizing spin-up) that a realistic initial state of cloud water content is given.

5. Acknowledgments

We thank Nils Gunnar Kvamstø for programming assistance and for performing the model simulations. We appreciate the assistance of G. W. Petty and D. K. Miller in producing the microwave integrated liquid water data. We also wish to thank Mr. Øyvind Thomassen for programming assistance and Mr. Frank Cleveland for preparing the figures. The SSM/I brightness temperatures were kindly provided by F. Wentz and E. Francis of Remote Sensing Systems, Inc. We gratefully acknowledge the computer resources that were provided free of charge by Bergen Scientific Centre (BSC/IBM). The work by E. R. and H. S. has been supported by The Norwegian Research Council for Science and Humanities under Contract ABC/SDU 447.89/008. The work at University of Washington was supported by NASA Grants NAGW-1688 and NAG5-943.

6. Appendix

List of ACRONYMS

AMUB	Section of Meteorology, University of Bergen
AVHRR	Advanced Very High Resolution Radiometer
BSC	Bergen Scientific Centre (IBM)
CFL	Courant-Friedrichs-Levy (numerical stability condition)
CWC	Cloud Water Content
FIRE	First ISCCP Regional Experiment
GCM	General Circulation Model
ISCCP	International Satellite Cloud Climatology Project
LWC	Liquid Water Content
NRSC	Nansen Remote Sensing Center
NWP	Numerical Weather Prediction
SMMR	Scanning Multichannel Microwave Radiometer
SSM/I	Special Sensor Microwave Imager

REFERENCES

Arking, A. and Childs, J. D. 1985. Retrieval of Cloud Cover Parameters from Multispectral Satellite Images. *J. Clim. and Appl. Meteor. 24*, 322–333.

Bratseth, A. M. 1983. Some economical, explicit finite-difference schemes for the primitive equations. *Mon. Wea. Rev. 111*, 663–668.

Cess, R. D., Potter, G. L., Blanchet, J. P., Boer, G. J., Gahn, S. J., Kiehl, J. T., Le Treut, H., Liang, Z.-X.,

Mitchell, J. F. B., Morcrette, J.-J., Randall, D. A., Riches, M. R., Röckner, E., Schlese, U., Slingo, A., Taylor, K. E., Washington, W. M., Weatherald, R. T. and Yagai, I. 1989. Interpretation of cloud-climate feedback as produced by 14 atmospheric general circulation models. *Science 245*, 513–516.

Coakley, J. A. and Chylek, P. 1975. The two-stream approximation in radiative transfer: including the angle of the incident radiation. *J. Atmos. Sci. 32*, 409–418.

Cox, S. K., McDougal, D., Randall, D. A. and Schiffer, R. A. 1987. FIRE-The First ISCCP regional experiment. *Atmosphere, Ocean 67*, 114–118.

Curry, J. A., Ardeel, C. D. and Tian, L. 1990. Liquid Water Content and Precipitation Characteristics of Stratiform Clouds as Inferred from Satellite Microwave Measurements. *J. Geophys. Res. 95*, 16659–16671.

Grønås, S., Foss, A. and Lystad, M. 1987. Numerical simulations of polar lows in the Norwegian Sea. *Tellus 39A*, 334–353.

Katsaros, K. B., Bhatti, I., McMurdie, L. A. and Petty, G. W. 1989. Identification of atmospheric fronts over the ocean with microwave measurements of water vapor and rain. *Weather and Forecasting 4*, 449–460.

Katsaros, K. B., Hammarstrand, U. and Petty, G. W. 1990. Atmospheric water in mid-latitude cyclones observed by microwave radiometry and compared to model calculations. *Report DM-52*. Department of Meteorology, Stockholm University, S-106 91 Stockholm, Sweden.

Manabe, S. and Stouffer, R. J. 1980. Sensitivity of a global climate model to an increase of CO_2-concentration in the atmosphere. *J. Geophys. Res. 85*, 5529–5554.

McMurdie, L. A. and Katsaros, K. B. 1985. Atmospheric water distribution in a mid-latitude cyclone observed by the Seasat Scanning Multichannel Microwave Radiometer. *Mon. Wea. Rev. 113*, 584–598.

Nordeng, T. E. 1986. Parameterization of physical processes in a three-dimensional numerical weather prediction model. *Tech. Rep. no. 65*. The Norwegian Meteorological Institute, Oslo, Norway.

Petty, G. W. 1990. *On the response of the Special Sensor Microwave/Imager to the marine environment—Implications for atmospheric parameter retrievals.* Ph.D. Thesis. Dept. of Atmospheric Sci., University of Washington. (Available from University Microfilms, 300 North Zeeb Road, Ann Arbor, Michigan 48106, USA, pp. 291.)

Ramanathan, V. E., Pitcher, E. J., Malone, R. C. and Blackmon, M. L. 1983. The response of a spectral general circulation model to refinements in radiative processes. *J. Atmos. Sci. 40*, 605–630.

Raustein, E. 1989. Use of a clustering method for objective cloud classification and determination of cloud parameters from satellite data. *Report NR: 2, 1989*. Meteorological Report Series, University of Bergen. (Available from Geophysical Institute, University of Bergen, Allégt. 70, N-5007 Bergen, Norway.)

Röckner, E. and Schlese, U. 1987. Cloud optical depth feedbacks and climate modelling. *Nature 329*, 10 September, 138–140.

Saunders, R. W. 1989. A comparison of Satellite-retrieved Parameters with Mesoscale Model Analyses. *Quart. J. Roy. Meteor. Soc. 115*, 651–672.

Slingo, A. and Slingo, J. M. 1988. The response of a general circulation model to cloud longwave radiation forcing. I: Introduction and initial experiments. *Quart. J. Roy. Meteor. Soc. 114*, 1027–1062.

Slingo, A. 1990. Sensitivity in the earth's radiation budget to changes in low clouds. *Nature 343*, 4 January 1990, 49–51.

Staelin, D. H., Kunzi, K. F., Pettyjohn, R. L., Poon, R. K. L. and Wilcox, R. W. 1976. Remote sensing of atmospheric water vapor and liquid water with the Nimbus 5 microwave spectrometer. *J. Appl. Meteor. 15*, 1204–1214.

Stephens, G. L. 1978. Radiation Profiles in extended Water Clouds. II: Parameterization Schemes. *J. Atmos. Sci. 35*, 2123–2132.

Sundqvist, H. 1988. Parameterization of condensation and associated clouds in models for weather prediction and general circulation simulation. In: *Physically-based modelling and simulation of climate and climatic change*, (ed. M. E. Schlesinger), Reidel, Dordrecht. Part I, 433–461.

Sundqvist, H., Berge, E. and Kristjánssón, J. E. 1989. Condensation and cloud parameterization studies with a mesoscale numerical weather prediction model. *Mon. Wea. Rev. 117*, 1641–1657.

Takeda, T. and Liu, G. 1987. Estimation of atmospheric liquid-water amount by NIMBUS 7 SMMR data: A new method and its application to the western North-Pacific region. *J. Meteor. Soc. Japan 65*, 931–947.

Taylor, V. R. and Stowe, L. L. 1984. Atlas of reflectance patterns for uniform earth and cloud surfaces. *NOAA Technical Reports, NESDIS 10*.

Tian, L. and Curry, J. A. 1989. Cloud overlap statistics. *J. Geophys. Res. 94*, D7, 9925–9935.

Wetherald, R. J. and Manabe, S. 1988. Cloud feedback processes in a general circulation model. *J. Atmos. Sci. 45*, 1397–1415.